(4)

AD-A225 859

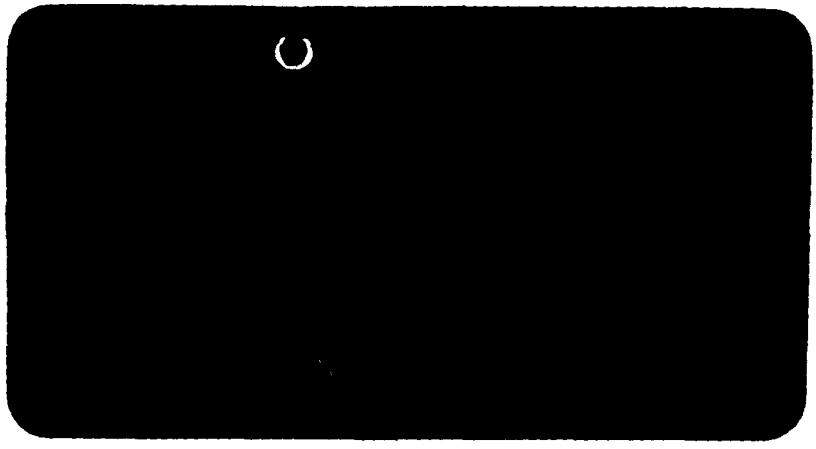





CERAMICS
PROCESS SYSTEMS

(4)

SECOND ANNUAL REPORT

FOR THE PROJECT

"COMPOSITE CERAMIC SUPERCONDUCTING
WIRES FOR ELECTRIC MOTOR APPLICATIONS"

PRIME CONTRACTOR

CERAMICS PROCESS SYSTEMS CORPORATION
155 FORTUNE BOULEVARD
MILFORD, MASSACHUSETTS 01757

30 JULY 1990

CPS 90-020

DARPA ORDER NO: 9525
CONTRACT NO: N00014-88-C-0512
CONTRACT EFFECTIVE DATE: 30 JUNE 1988
CONTRACT EXPIRATION DATE: 31 MARCH 1991
PRINCIPAL INVESTIGATOR: JOHN W. HALLORAN
(508) 634-3422

Prepared for
DEFENSE ADVANCED RESEARCH PROJECTS AGENCY
1400 Wilson Boulevard
Arlington, VA 22209

OFFICE OF NAVAL RESEARCH
800 North Quincy Street
Arlington, VA 22217-5000

# REPORT DOCUMENTATION PAGE

Form Approved
OMB No. 0704-0188



| 1. AGENCY USE ONLY (Leave blank) | 2. REPORT DATE | 3. REPORT TYPE AND DATES COVERED |
|---|---|---|
| | 30 July 1990 | Technical Report 1 July 89- 30 June 90 |

**4. TITLE AND SUBTITLE**
Composite Ceramic Superconducting Wires for Electric Motor Applications

**5. FUNDING NUMBERS**
N00014-88-C-0512

**6. AUTHOR(S)**
J. W. Halloran

**7. PERFORMING ORGANIZATION NAME(S) AND ADDRESS(ES)**
Ceramics Process Systems Corporation
155 Fortune Boulevard
Milford, MA 01757

**8. PERFORMING ORGANIZATION REPORT NUMBER**
CPS 90- 020

**9. SPONSORING/MONITORING AGENCY NAME(S) AND ADDRESS(ES)**
Defense Advanced Research Projects Agency
1400 Wilson Boulevard, Arlington, VA 22209

Office of Naval Research
800 North Quincy Street, Arlington, VA 22217-500

**10. SPONSORING/MONITORING AGENCY REPORT NUMBER**

**11. SUPPLEMENTARY NOTES**
N/A

**12a. DISTRIBUTION/AVAILABILITY STATEMENT**
Unlimited

**12b. DISTRIBUTION CODE**

**13. ABSTRACT** (Maximum 200 words)

Several types of HTSC wire have been produced and two types of HTSC motors are being built. Hundreds of meters of Ag- clad wire were fabricated from $YBa_2Cu_3O_{7-x}$ (Y-123) and $Bi_2Ca_2Sr_2Cu_3O_{10}$ (BiSCCO). The DC homopolar motor coils are not yet completed, but multiple turns of wire have been wound on the coil bobbins to characterize the superconducting properties of coiled wire. Multifilamentary conductors were fabricated as cables and coils. The sintered polycrystalline wire has self-field critical current densities ($J_c$) as high as 2800 A/cm$^2$, but the $J_c$ falls rapidly with magnetic field. To improve $J_c$, sintered YBCO wire is melt textured with a continuous process which has produced textured wire up to 0.5 meters long with 77K transport $J_c$ above 11,770 A/cm$^2$ in self field and 2100 A/cm$^2$ at 1 telsa.

The Emerson Electric DC homopolar HTSC motor has been fabricated and run with conventional copper coils. A novel class of potentially very powerful superconducting motors have been designed to use trapped flux in melt textured Y-123 as "magnet replicas" in an new type of permanent magnet motor. The stator element and part of the rotor of the first prototype machine exist, and the HTSC magnet replica segments are being fabricated.

| 14. SUBJECT TERMS | 15. NUMBER OF PAGES |
|---|---|
| Superconductor, ceramic, motor | 129 |
| | 16. PRICE CODE |

| 17. SECURITY CLASSIFICATION OF REPORT | 18. SECURITY CLASSIFICATION OF THIS PAGE | 19. SECURITY CLASSIFICATION OF ABSTRACT | 20. LIMITATION OF ABSTRACT |
|---|---|---|---|
| Unclassified | Unclassified | Unclassified | |

# COMPOSITE CERAMIC SUPERCONDUCTING WIRES FOR ELECTRIC MOTOR APPLICATIONS

## EXECUTIVE SUMMARY

This is a progress report for July 1989-June 1990, on a program to develop high temperature superconducting (HTSC) wire by cladding HTSC ceramic fibers with metal, and to build an high temperature superconducting motor.

We demonstrated our fiber process for wire by fabricating hundreds of meters of silver clad wire from both $YBa_2Cu_3O_{7-x}$ (Y-123) and $Bi_2Ca_2Sr_2Cu_3O_{10}$ (BiSCCO). The fiber spinning and green cladding operations produce kilometer-long continuous material. Much effort was devoted to scaling up the wire process to fabricate HTSC coils for a DC homopolar motor. The coils are not yet completed, but we have wound multiple turns of wire on the coil bobbins, and characterized the superconducting properties of the coiled wire. We have demonstrated multifilamentary conductors as cables and coils of sintered silver clad braided wire. The sintered polycrystalline wire has self-field critical current densities ($J_c$) as high as 2800 A/cm$^2$, but are weak-linked, so the $J_c$ falls rapidly with magnetic field.

To overcome the weak-link problem we "melt texture" the sintered wire by directional solidification. We have a continuous melt texturing process for Y-123 wires which, while slow, can produce textured wire up to 0.5 meters long. The melt textured wire has 77K transport $J_c$ above 11,770 A/cm$^2$ in self field and 2100 A/cm$^2$ at 1 telsa.

The Emerson Electric DC homopolar HTSC motor was designed to operate with low $J_c$ wire to be a test bed for wire. The machine has been fabricated and operated conventional copper coils. A novel class of superconducting motors have been designed at Emerson Electric subcontract, using trapped flux in melt textured Y-123 as "magnet replicas" in an new type of permanent magnet motor. These have the promise for very high output motors, and can be built in the very near term. The stator element and part of the rotor of the first prototype machine presently exist, and the HTSC magnet replica segments are now being fabricated.

TABLE OF CONTENTS

page

SECTION 1 GENERAL INTRODUCTION....1

SECTION 2 WIRE FABRICATION....12

2.1 Introduction and General Comments....12

2.2 Fiber Preparation....13
2.2.1 Introduction....13
2.2.2 Powder production....13
2.2.3 Green fiber spinning....19
2.2.3.1 Experimental fibers....19
2.2.3.2 Alternate polymer systems....21
2.2.3.3 Multifilament Fiber Development....22
2.2.4 Braiding of Y-123 green fibers....23

2.3 Cladding and Sintering....26
2.3.1 Cladding and co-firing....26
2.3.2 Continuous sintering....32
2.3.3 Oxygen Annealing....34
2.3.4 Fabrication of Homopolar Motor Field Coil Segments....36
2.3.5 Properties of SP Wire....40
2.3.5 1 Mechanical Behavior....40
2.3.6 Processing of BiSCCO Fiber and Wire....43
2.3.6 Braided Sintered Wire....45

2.4 Electrical Characterization....50
2.4.1 Measurement Technique....51
2.4.2 Critical Current Density in Applied Magnetic Field....51
2.4.2 Magnetic Susceptibility....52
2.4.2 Statistical and Spacial Variations in Critical Current Density....52

2.5 Melt Processing of HTSC Wires....65
2.5.1 Melt Processing Activities at CPSS....65
2.5.1.1 Continuously melt textured wire....66
2.5.1.2 Melt Textured Pellets....68
2.5.2 A. D. Little Laser Float Zone Program....69
2.5.3 Oak Ridge National Laboratory Pilot Center Program....70
2.5.4 Rapid Thermal Processing....79

SECTION 3 HIGH TEMPERATURE SUPERCONDUCTOR MOTOR DESIGN AND FABRICATION....81

3.1 Introduction....81

3.2 Iron Core Homopolar Motor....82
3.2.1 Brush Testing....85
3.2.1.1 Brush Friction....85

TABLE OF CONTENTS -- continued

3.2.1.2 Voltage Drop Tests....86
3.2.2 Homopolar Motor Performance Calculations....96
3.2.2.1 Original Designed Performance....96
3.2.2.2 Effects of $J_c$ Reduced by Magnetic Field....100
3.2.3 Testing of Homopolar DC Motor with Copper Field Windings..110

3.3 Brushless DC Motor Using Trapped Flux HTSC Magnets....112

3.4 Other Advanced HTSC Motor Designs....120
3.4.1 High Performance Homopolar DC Motor....120
3.4.2 Heteropolar DC Motor....120

3.5 Summary....121

SECTION 4 GENERAL DISCUSSION AND SUMMARY....122

4.1 General Discussion....122

4.2 Prospects for Practical Applications for YBCO Wire at 77K....123

4.3 Prospects for Practical Applications for BiSCCO Wire at 77K and Lower Temperatures....125

4.4 Summary....128

# LIST OF FIGURES

page

Figure 1.1.1 Spools of Y-123 Wire and Its Precursor Fibers. From Left: Bare Green Y-123 Fiber; Green Silver Clad Fiber; and Sintered Silver Clad Y-123 Wire.....4

Figure 1.1.2 Prototype Bobbin For the Emerson Homopolar Motor with Eleven Turns of Annealed Superconducting Sintered Ag-Clad Y-123 Wire.....4

Figure 1.1.3 Continuously Melt Textured YBCO Wires of 100 Micron and 200 Micron Nominal Diameter. Above: Wire Mounted for Electrical Test, With Shorter Segments Below: Several Longer Wires.....5

Figure 1.1.4 Emerson Electric HTSC Homopolar Machine in Test Mount.....6

Figure 1.1.5 Components of the Hybrid Trapped Flux "Permanent Magnet Motor" Below: Stator with Resistive Coils Above: Rotor (without HTSC segments).....6

Figure 1.1.6 Revised Project Schedule for Fiber.....9

Figure 1.1.7 Revised Project Schedule for Wire Tasks. Note that Ribbon Wire had been postponed in favor of monofil wire and new tasks in melt textured wire and BiSCCO wire have been added.....10

Figure 1.1.8 Project Schedule for HTSC Motor Task.....11

Figure 2.2.1 Resistive Transition for Bi(Pb)SCCO Tape Calcined at 775°C and Sintered at 865°C.....16

Figure 2.2.2 Peak Height Ratios for (002) Diffraction Lines for the "High Temperature" Bi-2223 Phase And the "Low Temperature) Bi-2122 Phase Versus Calcination Time and Temperature for Compositions BPH2 and BP5.....16

LIST OF FIGURES- continued


| | | Page |
|---|---|---|
| Figure 2.2.3 | AC Susceptibility of $Bi_{1.7}Pb_{0.3}Ca_2Sr_2Cu_3O_\delta$ Pellet After Calcining 6 Hours at 775°C and sintering 30 Hours at 845°C | 17 |
| Figure 2.2.4 | AC Susceptibility of $Bi_{1.7}Pb_{0.3}Ca_2Sr_2Cu_3O_\delta$ Pellet After Calcining 6 Hours at 775°C and sintering 132 Hours at 845°C | 17 |
| Figure 2.2.5 | AC Susceptibility of $Bi_{1.2}Pb_{0.8}Ca_2Sr_2Cu_3O_\delta$ Pellet After Calcining 380 Hours at 845°C and sintering 30 Hours at 845°C | 18 |
| Figure 2.2.6A | Photograph of 1.5 Kilometer Spool of Y-123 Green Fiber | 24 |
| Figure 2.2.6B | Two Recent Spools of Y-123 Green Fiber Left: Bare Fiber Right: Green Clad Fiber | 24 |
| Figure 2.2.7A | Sixteen Filament Flat Braid of 125-Micron Y-123 Green Fiber | 25 |
| Figure 2.2.7B | Sixty Eight Filament Flat Braid of 125-Micron Y-123 Green Fiber | 25 |
| Figure 2.3.1 | Green Fiber Before and After Coating With PM Silver Green Cladding | 30 |
| Figure 2.3.2 | Comparison of the Porous Silver Coatings form Spherical Powders with Dense Silver Coatings from Flakey Silver Powders | 31 |
| Figure 2.3.3 | Cross Section of Recent Ag-Clad Sintered Polycrystalline Y-123 Wire | 31 |
| Figure 2.3.4 | Electric Field vs. Current Density for a 1.3-Turn, 0.86 Meter Long Segment in the Center of Coil 1, Showing a $J_c$ of 500 A/cm$^2$ | 39 |
| Figure 2.3.5 | Electric Field vs. Current Density for the Entire 11 Turns,7.14 Meters of Coil 2 and Five Partial Segments | 39 |

LIST OF FIGURES- continued

page

Figure 2.3.6A Tensile Properties of Sintered Y-123 Wire, Comparing Load at Fracture Distributions for Bare Fiber, Wire with 23-Micron Thick Cladding of Dense Silver, and a Wire with 48-Micron Thick Cladding of Porous Silver.....42

Figure 2.3.6B Tensile Properties of Sintered Y-123 Wire, Comparing Stress at Fracture Distributions for Bare Fiber, Wire with 23-Micron Thick Cladding of Dense Silver, and a Wire with 48-Micron Thick Cladding of Porous Silver.....42

Figure 2.3.7 Stages in the Production of Prototype BiSCCO Wire. From Left: Green fiber, Green Clad Fiber, Sintered Wire after Rolling.....44

Figure 2.3.8 Seventeen Filament Braid of Silver Clad Polycrystalline Y-123 Wire Continuously Sintered using Braided Green Clad Fiber.....48

Figure 2.3.9 Electric Field vs. Current Density at 77K for Seventeen Filament Braid Silver Clad Polycrystalline Y-123 Wire, Comparing the Middle 50-cm Section with the Entire 106-cm Gage Length.....48

Figure 2.3.10 Critical Current Density vs. Magnetic Field at 77K for Seventeen Filament Braided Silver Clad Polycrystalline Y-123 Wire.....49

Figure 2.3.11 Electric Field vs. Current Density at 77K for 8-Turn Coil Made With Braided Silver Clad Polycrystalline Y-123 Wire, Comparing the Central Two Turns with Complete Coil.....49

Figure 2.4.1 Electric Field vs. Current Density at 77K in Self Field for Bare Filament and Clad Wire.....56

Figure 2.4.2 Critical Current Density vs. Magnetic Field for Clad Wire at 77K.....57

LIST OF FIGURES- continued

page

Figure 2.4.3 Critical Current Density vs. Magnetic Field at 77K for Bare Y-123 Filament....58

Figure 2.4.4 Distribution of $J_c$ Data for Short Wire Samples....59

Figure 2.4.5 Distribution of $J_c$ Data for 2-cm Segments of Long Wires Compared with Short Wire Samples at 2-cm Gage Length....60

Figure 2.4.6 Distribution of $J_c$ Data for 2-cm Segments, 4- cm Segments, and 8-cm Segments of Long Wires....61

Figure 2.4.7 Spacial Variations of $J_c$ Within Three Long Wires....62

Figure 2.4.8 Voltage Measured at Each of the Four Taps in a Multiple Contact Long Wire at Current Densities of 305-,407-, 509-and 1005 A/cm$^2$....63

Figure 2.4.9 Transport Critical Current Density vs. Volume Susceptibility at 77K....64

Figure 2.5.1 Continuously Melt Textured 250-Micron YBCO Wire Mounted for Electrical Testing....71

Figure 2.5.2 Critical Current Density at 77K vs. Magnetic Field for the 250-micron Diameter Melt Textured Wire....72

Figure 2.5.3 Electric Field vs. Current Density at 77K in Self Field for Four Adjacent Regions of a 10-cm Long Melt Textured YBCO Wire....73

Figure 2.5.4A Microstructure of a "Good" Region of a Melt Textured YBCO Wire, Showing Several Well Oriented Grains Crossed Polars 200X....74

Figure 2.5.4B Microstructure of a "Poor" Region of a Melt Textured YBCO Wire, Showing Poor Orientation of Grains Crossed Polars 200X....74

Figure 2.5.4C Microstructure of a "Poor" Region of a Melt Textured YBCO Wire, Showing Abrupt Termination of Oriented Grains....75

LIST OF FIGURES- continued

page

Figure 2.5.5 AC Susceptibility vs. Temperature for 250 -Micron Melt Textured YBCO Wire....76

Figure 2.5.6 AC Susceptibility vs. Temperature for Melt Textured YBCO Pellet....76

Figure 2.5.8 Laser Float Zone Processed Y-123+Y-211 Rods....77

Figure 2.5.9 Polished Section of Laser Float Zone Processed Y-123 Rod CPS-1, after Post-Anneal at 850°C
Above:Ordinary Light Below:Crossed Polars 200X....78

Figure 3.2.1 Superconducting Homopolar Motor Design....83

Figure 3.2.2 Motor Cross-Section Through Brush Assembly....84

Figure 3.2.3 Voltage Drop vs. Current for 65% Copper Brush on Copper Slip Ring....88

Figure 3.2.4 Voltage Drop vs. Current for 65% Copper Brush on Brass Slip Ring....89

Figure 3.2.5 Voltage Drop vs. Current for 65% Copper Brush on Smooth Steel Slip Ring....90

Figure 3.2.6 Voltage Drop vs. Current for 65% Copper Brush on Steel Slip Ring (16 threads per inch)....91

Figure 3.2.7 Voltage Drop vs. Current for 85% Copper Brush on Copper Slip Ring....92

Figure 3.2.8 Voltage Drop vs. Current for 85% Copper Brush on Brass Slip Ring....93

Figure 3.2.9 Voltage Drop vs. Current for 85% Copper Brush on Smooth Steel Slip Ring....94

Figure 3.2.10 Voltage Drop vs. Current for 85% Copper Brush on Steel Slip Ring (16 threads per inch)....95

Figure 3.2.11 Steel Core Homopolar Motor Flux Plot....97

Figure 3.2.12 Current Contour....99

LIST OF FIGURES- continued

page


Figure 3.2.13 Motor Power and Losses vs. Brush Pressure for 100% Field Coil Ampere Turns. Speed is 3000 RPM. Current is 1000 Amperes.....101

Figure 3.2.14 Current Density vs. Magnetic Field for HTSC Wire and for Motor Coils.....102

Figure 3.2.15 Motor Power and Losses vs. Brush Pressure for 50% Field Coil Ampere Turns. Speed is 3000 RPM. Current is 1000 Amperes.....104

Figure 3.2.16 Motor Power and Losses vs. Brush Pressure for 35% Field Coil Ampere Turns. Speed is 3000 RPM. Current is 1000 Amperes.....105

Figure 3.2.17 Motor Power and Losses vs. Brush Pressure for 25% Field Coil Ampere Turns. Speed is 3000 RPM. Current is 1000 Amperes.....106

Figure 3.2.18 Current Density vs. Magnetic Field for HTSC Wire with Coil Operating Points.....107

Figure 3.2.19 Flux Densities and Current Densities in Six Small HTSC Coils with Optimized Current Distribution.....108

Figure 3.2.20 Motor Power and Losses vs. Brush Pressure for 30% Field Coil Ampere Turns. Speed is 3000 RPM. Current is 1000 Amperes.....109

Figure 3.2.21 Flux Through Field Coil vs Field Coil Ampere-Turns..110

Figure 3.3.1 Brushless DC Motor with HTSC Stator Windings and Bulk HTSC Rotor.....113

Figure 3.3.2 HTSC Stator Supplies Magnetic Field to Charge the Rotor of a Superconducting Brushless DC Motor...115

Figure 3.3.3 Flux is Trapped in the HTSC Material After Rotor is Cooled in a Magnetic Field.....116

Figure 3.3.4 HTSC Brushless DC Rotor and Stator Flux Combine in the Peak Torque Position.....117

LIST OF FIGURES- continued

page

Figure 3.3.5 Horsepower versus Current Density in HTSC Stator Windings.....119

Figure 4.1 Critical Currents in Bulk YBCO at 77K, State of the Art, July 1990.....127

# COMPOSITE CERAMIC SUPERCONDUCTING WIRES FOR ELECTRIC MOTOR APPLICATIONS

JOHN W. HALLORAN
PRINCIPAL INVESTIGATOR
CERAMICS PROCESS SYSTEMS CORPORATION
MILFORD, MASSACHUSETTS 01757

## SECTION 1

## GENERAL INTRODUCTION

This Second Annual Report covers activities during July 1989 through June 1990, on a program to develop high temperature superconducting wire by cladding $YBa_2Cu_3O_{7-x}$ (Y-123) ceramic fibers with metal, and to use this wire to build a superconducting motor.

Progress has been very good. We have successfully demonstrated our fiber process for wire by fabricating continuous silver clad YBCO wire from both $YBa_2Cu_3O_{7-x}$ (Y-123) and $Bi_{1.7}Pb_{0.3}Ca_2Sr_{2.0}Cu_3O_{10-\delta}$ (lead doped BiSCCO) systems. We have made hundreds of meters of sintered Y-123 wire, and our fiber spinning and green cladding operations produce kilometer-long continuous material. Some of the products of our research are illustrated in Figure 1.1.1, a photograph showing spools of our green Y-123 fiber, green silver clad fiber, and sintered Y-123 wire.

Much of our effort this year was devoted to scaling up the wire process to produce enough to wind HTSC coils for the Emerson DC homopolar motor. While we have not completed the homopolar motor coils, we have wound up to eleven turns of wire on the coil bobbins, and characterized the superconducting properties of the coiled wire. One of these coil bobbins appears in Figure 1.1.2.

We have demonstrated multifilamentary braided conductors as cables and coils of sintered silver clad multifilament braided wire. The multifilamentary wire has the same critical current in meter-long gage lengths as it has in

centimeter-long samples.

The sintered polycrystalline (SP) wire has been extensively characterized, showing self-field critical current densities ($J_c$) as high as 3500 A/cm$^2$. They are, of course, weak-linked, so the $J_c$ falls rapidly with applied magnetic field. To overcome the weak-link problem we developed post-processing methods for the Y-123 sintered wire to melt texture the material by directional solidification. Early results are very encouraging. We have a continuous melt texturing process for Y-123 wires which, while slow, is capable of producing quite long textured wire. A collection of 100- and 200-micron diameter melt textured wires are shown in Figure 1.1.3. A recent melt textured wire exhibited a 77K transport $J_c$ above[3] 11,770 A/cm$^2$ in self field. The $J_c$ in a 1 Tesla magnetic field is 2100 A/cm$^2$.

The Emerson Electric DC homopolar HTSC motor has been fabricated and is undergoing tests with conventional copper coils. Figure 1.1.4 is a photograph of the homopolar motor mounted in a test stand (without the liquid nitrogen vessel). This machine has been designed to operate with the weak flux density available from low $J_c$ wire, providing a test bed for wire.

Recently there has been an exciting development in the Emerson Electric subcontract. Crapo and Lloyd at Emerson have designed an new type of "permanent magnet" motor which exploits trapped flux in melt textured Y-123 materials to create "magnet replicas". These have the promise for very high output motors, and can be built in the very near term. In fact, the stator element and part of the rotor of the first prototype machine is shown in Figure 1.1.5. This prototype is a hybrid machine, using bulk melt textured Y-123 pieces as magnet replica segments for the rotor, with resistive copper coils in the stator. These

---

[3]. The apparent critical current was limited by Joule heating of the silver paint contacts, so the actual 77 K is higher by an unknown amount.

segments are now being fabricated. We anticipate that this machine will produce at least 0.37 kilowatts (0.5 hp), operating in liquid nitrogen.

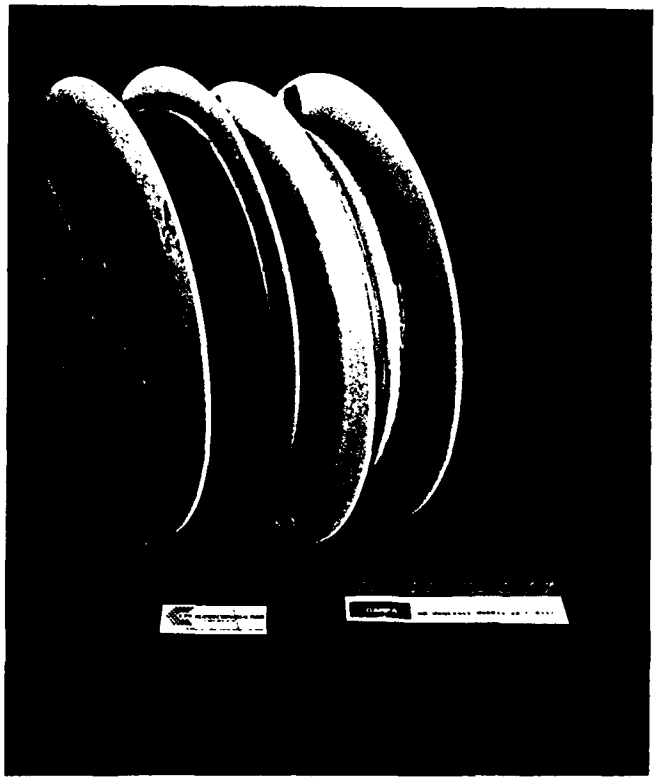

Figure 1.1.1 Spools of Y-123 Wire and Its Precursor Fibers. From Left: Bare Green Y-123 Fiber; Green Silver Clad Fiber; and Sintered Silver Clad Y-123 Wire

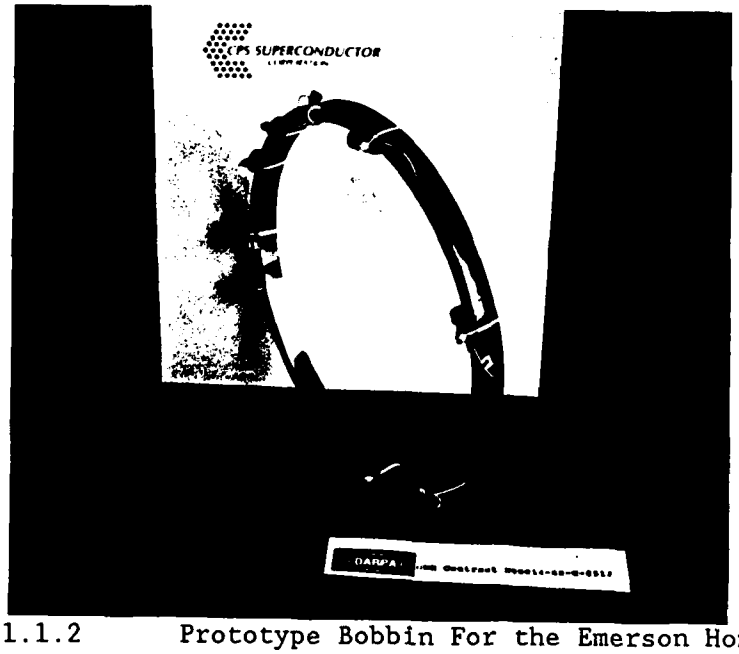


Figure 1.1.2 Prototype Bobbin For the Emerson Homopolar Motor with Eleven Turns of Annealed Superconducting Sintered Ag-Clad Y-123 Wire

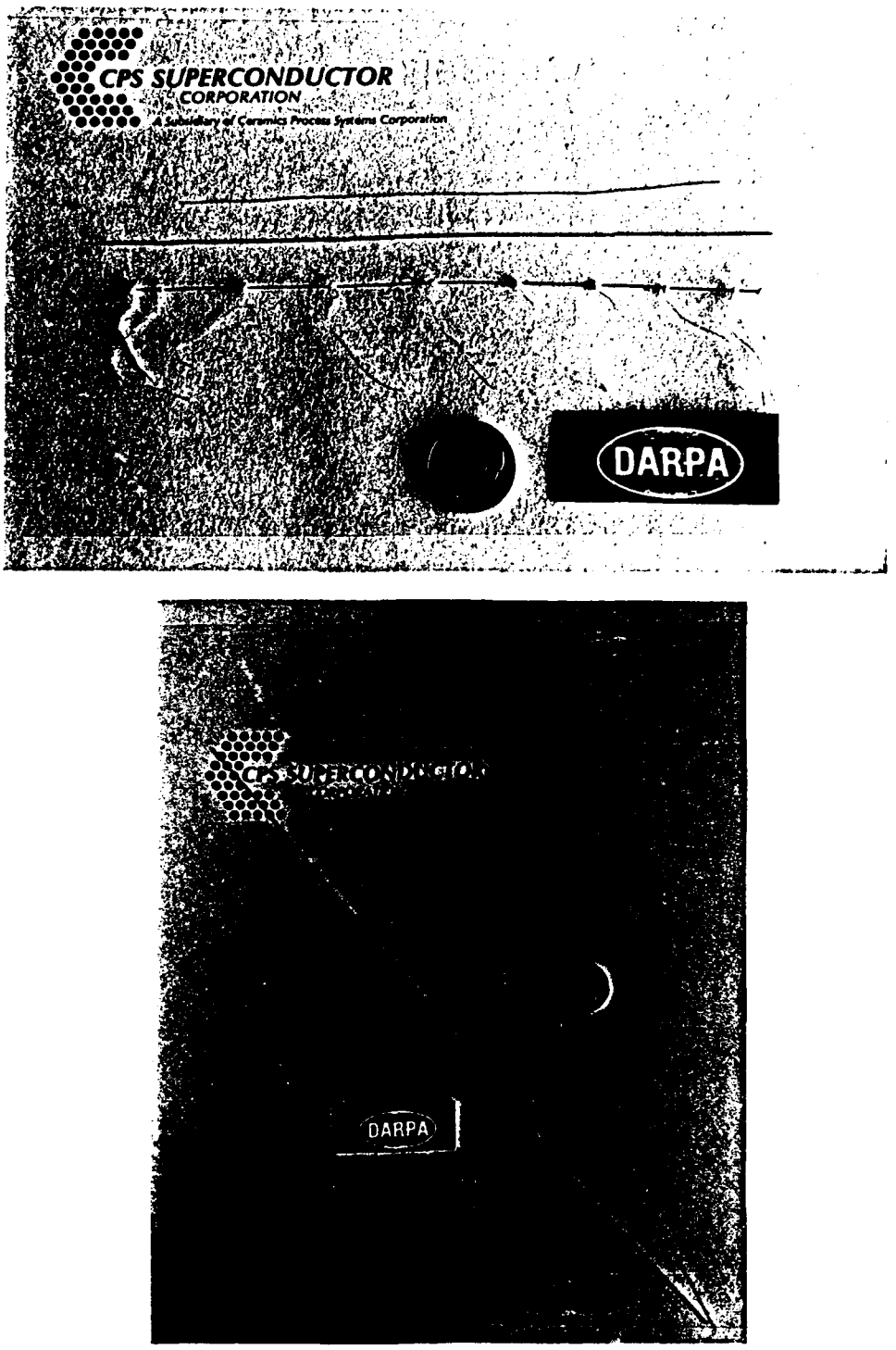


Figure 1.1.3 Continuously Melt Textured YBCO Wires of 100 Micron and 200 Micron Nominal Diameter.
Above: Wire Mounted for Electrical Test, With Shorter Segments
Below: Several Longer Wires

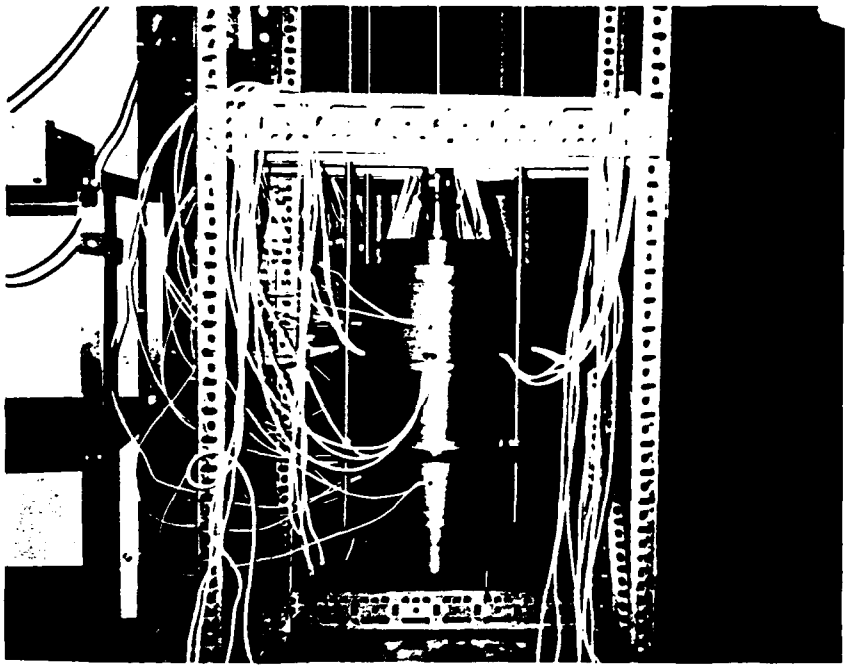

Figure 1.1.4 Emerson Electric HTSC Homopolar Machine in Test Mount (Without Liquid Nitrogen Vessel). At Left is the 3000 Amp DC Power Supply for the Rotor. Not Shown is the Power Supply For the Field Coils. ( Above the homopolar motor is a small DC motor used to spin the rotor to wear in the brushes)

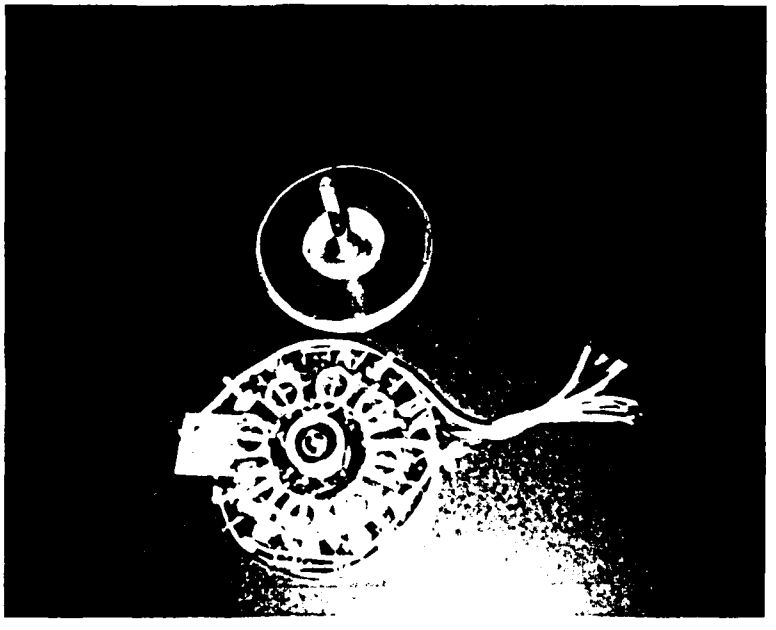

Figure 1.1.5 Components of the Hybrid Trapped Flux "Permanent Magnet Motor"
Below: Stator with Resistive Coils
Above: Rotor (without HTSC segments)

During the first three quarters of this year the program was carried out by three subcontractors: CPS Superconductor Corporation (CPSS), a subsidiary of Ceramics Process Systems, is responsible for the development of the wire; Albany International Research Corporation (AIResCo) develops the green fiber spinning and braiding methods, and provides all of the green fibers; and the Emerson Motor Division (EMD) of Emerson Electric, which is building the superconducting motor. A new subcontract dealing with improving melt texturing of Y-123 wire started last quarter at Arthur D. Little, Inc. and another subcontract is being negotiated with the HTSC Pilot Center at Oak Ridge National Laboratory. Unfunded collaborative research supporting the DARPA program included transmission electron microscopy of Y-123 wires done at Los Alamos National Laboratory as an HTSC Pilot Center contract, and informal collaborative research was done at Sandia National Laboratory to explore rapid thermal processing of HTSC wire.

We have made major changes in the development program as we pursued some promising opportunities and abandoned others. We have de-emphasized the design and building of (wire-wound) HTSC motors, reflecting the fact the multi-tesla HTSC coils (requiring many kiloamp-turns of wire) could not be produced in the current year. The funding made available by scaling down the motor effort has been used increase activities aimed at developing high $J_c$ wire. This includes increased efforts at CPSS and new subcontracts aimed at melt texturing at A. D. Little and Oak Ridge National Lab HTSC Pilot Center.

The status of the program is compared with individual tasks of the revised Statement of Work in Figures 1.1.6, 1.1.7, and 1.1.8, which show timelines for the major fiber and wire development tasks. The fiber spinning tasks, as shown, involves Y-123 melt spinning and braiding. These tasks will be extended through

1990. The wire tasks show several of the changes as the program has evolved. The main effort now involves silver coated and co-fired monofil wire, with braided multifilamentary wire as a secondary effort. The newer activities involving melt texturing, including in-house CPSS work and two planned subcontracts, now appear in the list of tasks. We are no longer working on multifilament ribbon wire, as it was originally envisioned, as this has been supplanted by work on braids. The HTSC motor tasks are on schedule, but do not involve testing with HTSC coils, since we have not yet produced complete coils.

The following sections describe in detail the progress on the wire manufacturing task and the motor design task. Section 2 covers all aspects of the wire manufacturing development, including the fiber spinning work conducted at Albany International Research Corporation in Mansfield, Massachusetts, and the Y-123 powder production, sintering, cladding, and characterization work conducted at CPS Superconductor in Milford, Massachusetts. Section 3 outlines the HTSC motor design activities at Emerson Motor Division in St. Louis, Missouri.

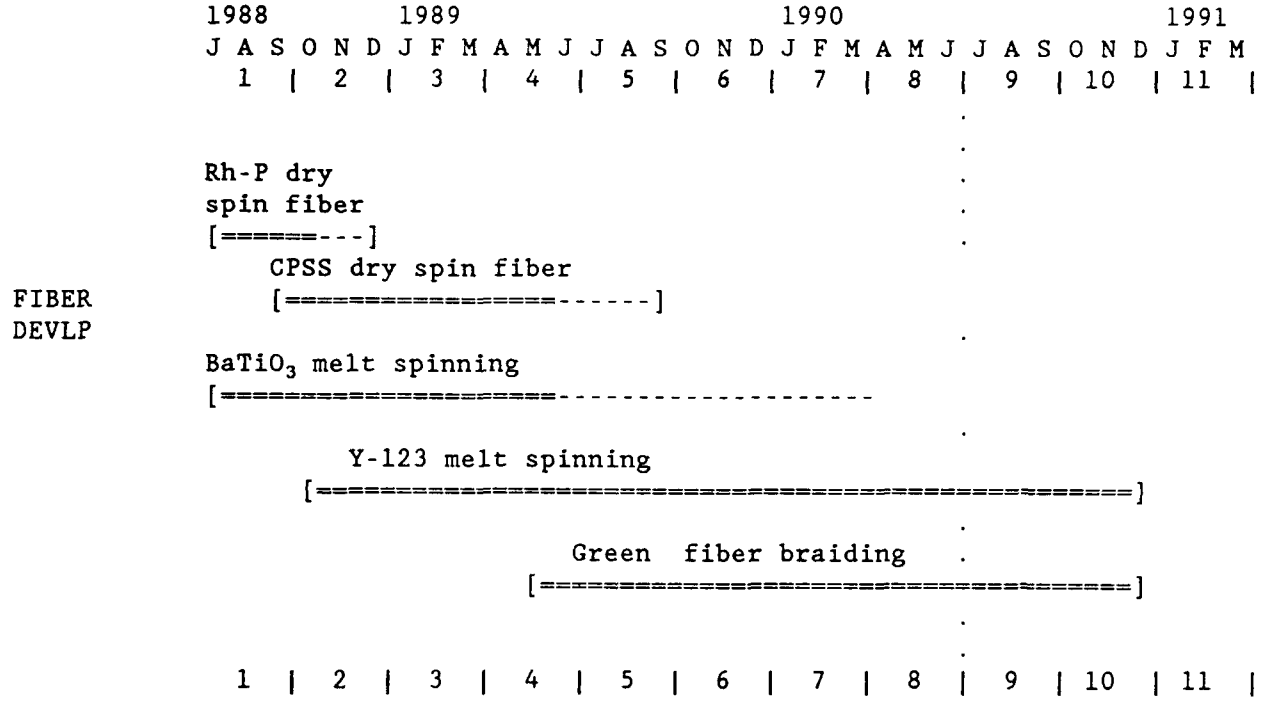


Figure 1.1.6 Revised Project Schedule for Fiber

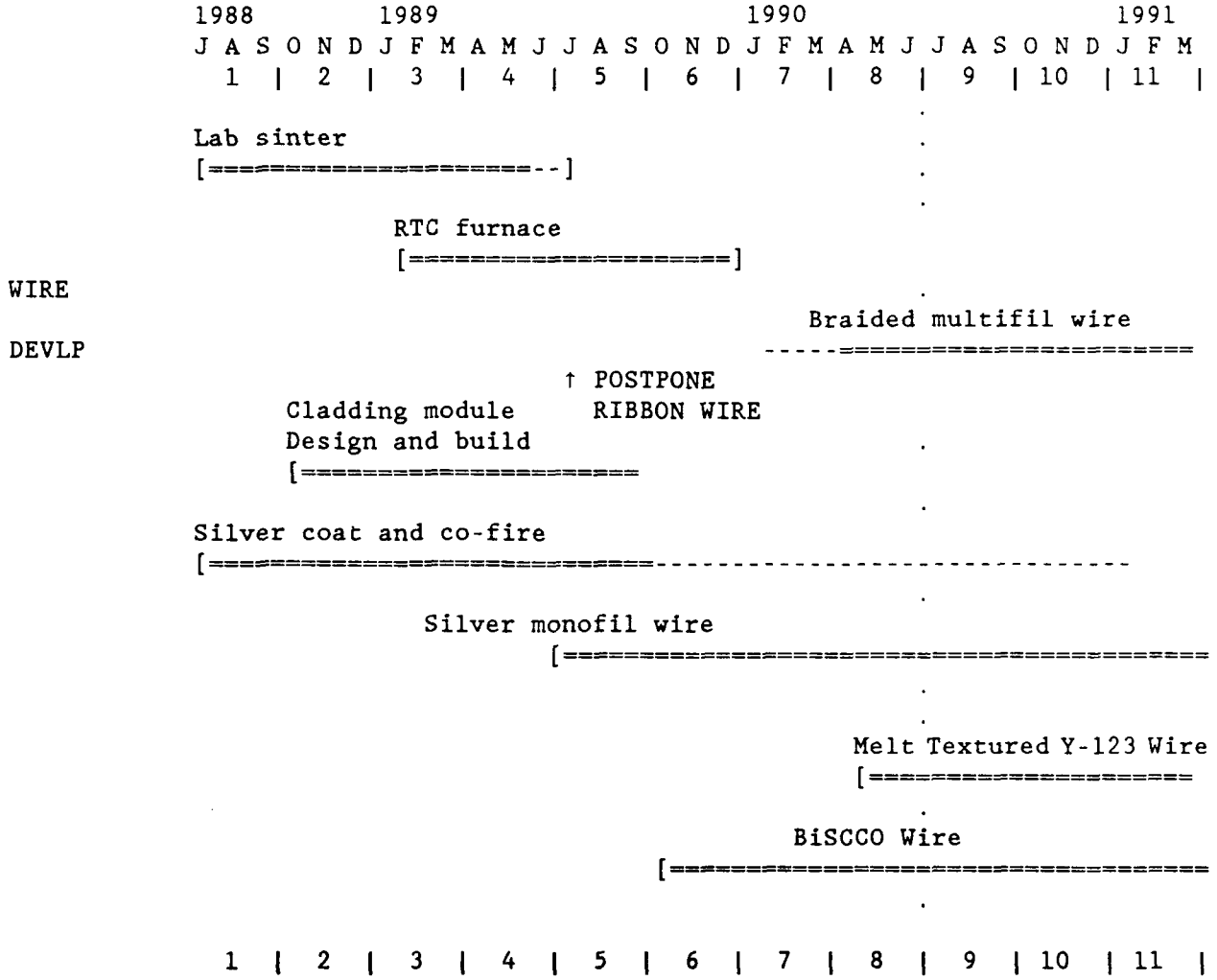


Figure 1.1.7 Revised Project Schedule for Wire Tasks. Note that Ribbon Wire had been postponed in favor of monofil wire and new tasks in melt textured wire and BiSCCO wire have been added

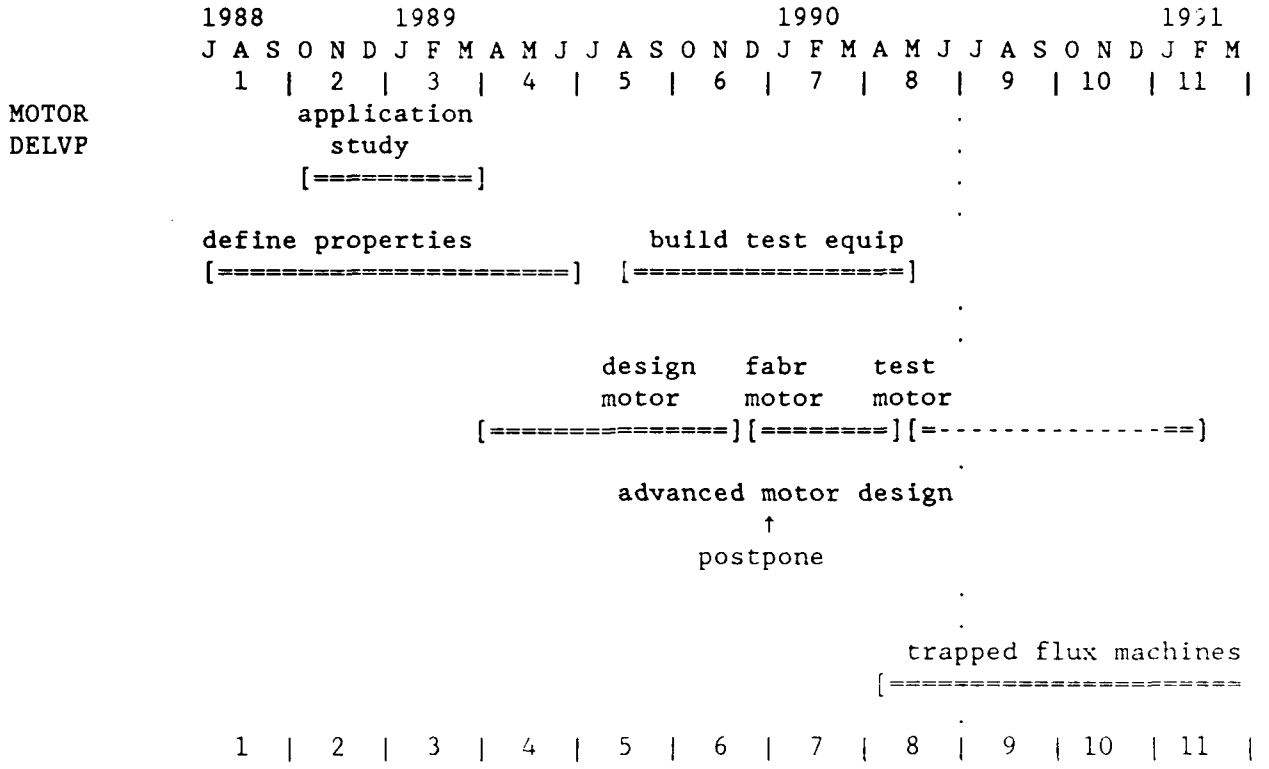


Figure 1.1.8 Project Schedule for HTSC Motor Task

# SECTION 2

# WIRE FABRICATION

DAVID CHANDLER, JOHN HALLORAN, JAMES HODGE, LORI JO KLEMPTNER, MATTHEW NEAL, MARK PARISH, HYUN PARK, MICHAEL PARKER, AND VIREN PATHARE
CPS SUPERCONDUCTOR CORPORATION

GEORGE BAKIS, DANA EAGLES, WESLEY ISHIDA, AND STEPHEN TIERNAN
ALBANY INTERNATIONAL RESEARCH CORPORATION

## 2.1 Introduction and General Comments

We have developed a three-step HTSC wire process which involves: (1) preparing textile-quality "green clad" fiber consisting of melt-spun HTSC green fiber with a particulate silver coating; (2) continuously sintering the fiber to produce silver-clad sintered polycrystalline wire (SP wire); and (3) post-processing the polycrystalline wire to make a high critical current density wire. We have demonstrated the practicality of each individual step, and proven the feasibility of the three steps in sequence.

We have made hundreds of meters of SP wire, mostly from $YBa_2Cu_3O_{7-x}$ (Y-123) in the form of flexible wire collected on a spool. We have fabricated fiber and Ag-clad wire from $Bi_{1.7}Pb_{0.3}Ca_2Sr_{2.0}Cu_3O_{10-\delta}$ (lead doped BiSCCO), and demonstrated that sintered BiSCCO wire can be rolled into ribbon. During this year we progressed from making 50-cm wire samples -- characterized as 3-cm short specimens-- to the point where we now fabricated 50-meter continuous lengths, which are wound onto bobbins and characterized in lengths up to 7-meters. We have made multifilamentary braided wire characterized in segments up to one meter long.

Most importantly, we have begun to overcome the weak-link problem and

produce wire with significantly higher critical current density. We are post processing our Y-123 wire by directional solidification of fibers, to make continuously melt textured wire carrying 11,770 A/cm$^2$ at self field and 1500 A/cm$^2$ at 1 Tesla.

This section documents activities for each major process steps, in chronological order for the process flow

## 2.2 Fiber Preparation

### 2.2.1 Introduction

Activities related to powder preparation and fiber processing are reported in this section. Production of materials in the Y-123 system included standard 1.6 micron stoichiometric powder and a variety of experimental off-stoichiometric compositions, largely for melt texturing work. Development of processes for BiSCCO materials received more attention in the second half of the year, leading to the ability to produce kilogram lots of powder containing up to 80 wt% of the 110K Bi-2223 phase. The fiber spinning process was further developed, with emphasis on green fibers with 60 volume percent Y-123 loadings, exploration of alternative polymers, and the first efforts at multifilamentary spinning. Braiding capability was greatly improved.

### 2.2.2 Powder production

Throughout this year we routinely produced our standard 1.6-micron Y-123 powder to supply project needs. The process was scaled up to the level of 10-kilogram batch size and standardized. This production level is sufficient for present powder requirements. Many lots of the standard powder were made. The total production of standard Y-123 for the project was about 53 kilograms.

Three quarters of this powder was used to make fiber, with the balance in current inventory. Consistency and uniformity was emphasized to assure constant raw material for the project. We continually examined process variables and techniques to improve the manufacturing process and powder quality, as well as examine environmental effects.

In addition to process development, we conducted research to characterize the gas-solid and solid-solid reactions during calcination of Y-123. This has included collaborative research with high temperature X-ray diffraction with Cam Hubbard at the High Temperature Materials Laboratory at Oak Ridge National Laboratory. This work will be reported in separate publications.

Several processes were examined for producing Y-124. We also prepared approximately quantities of Y-211 and barium cuprate to supply off-stoichiometric materials for melt processing.

We significantly increased effort directed at bismuth cuprate systems, with emphasis on the lead doped Bi(Pb)SCCO-2223 system, producing a number of compositions around $Bi_{2-x}Pb_xCa_{2+y}Sr_{2.0}Cu_{3+z}O_\delta$. This involved initial work with melt spun BiSCCO green fiber, which we used to produce silver clad sintered wire, and more detailed work to develop compositions and heat treatments. An 0.8 kg lot of powder was used to spin several large spools of 125-micron fiber and smaller quantity of 1375-micron fiber. This early powder was a two phase mixture of Bi-2122 and a calcium strontium plumbate. Later work involving composition development was conducted with tape cast sheets, instead of fibers. Compositions were formulated varying the lead substitution and copper content, calcination, and sintering. Tape samples were supported on silver foil during sintering. Figure 2.2.1 illustrates the resistive transition of one of the early sintered tapes. This work identified two promising compositions, which we coded

as BP5 ($Bi_{1.2}Pb_{0.8}Ca_2Sr_2Cu_3O_\delta$) and BPH2 ($Bi_{1.7}Pb_{0.3}Ca_2Sr_2Cu_3O_\delta$).

Recent work has concentrated on synthesis of larger quantities of the BP5 and BPH2 composition, using the scaled-up powder production facilities originally built for Y-123. Of particular interest was the development of the 2223 high temperature phase as a function of time and temperature in flowing air. Figure 2.2.2 shows the peak height ratio for the (002) peak for the high temperature 2223 phase with the (002) peak of the low temperature 2122 phase. The initial transformation rate of 2122 to 2223 is faster at 850°C and 860°C, but seems to reach a plateau around a peak height ratio of one. At 845°C the transformation rate is slower, but it reaches a greater ratio after long anneals.

We have found that large fractions of the 2223 phase can be developed either by calcining for relatively short times, followed by lengthy sintering anneals, or by calcining for a long time and sintering briefly. Optimal temperatures and times seem to be different for the BPH2 and BP5 compositions. Figure 2.2.3 shows that a BPH2 pellet calcined 6 hours at 775°C and sintered 30 hours at 845°C has a sharp drop in the real susceptibility at 105K involving 20% of the sample, with gradual increase of the superconducting fraction up to 80% at 60K. The same composition and calcining treatment has improved properties after a prolonged sintering treatment at 835°C. Figure 2.2.4 shows a 40% fraction at 105K, reaching almost 100% at 85K. The BP5 composition requires longer anneals to reach the same degree of conversion. The AC Susceptibility for a sample calcined 380 hours and sintered 30 hours at 845°C appears in Figure 2.2.5. It reaches nearly 100% superconducting fraction at 85K, but has only 20% fraction above 105K.

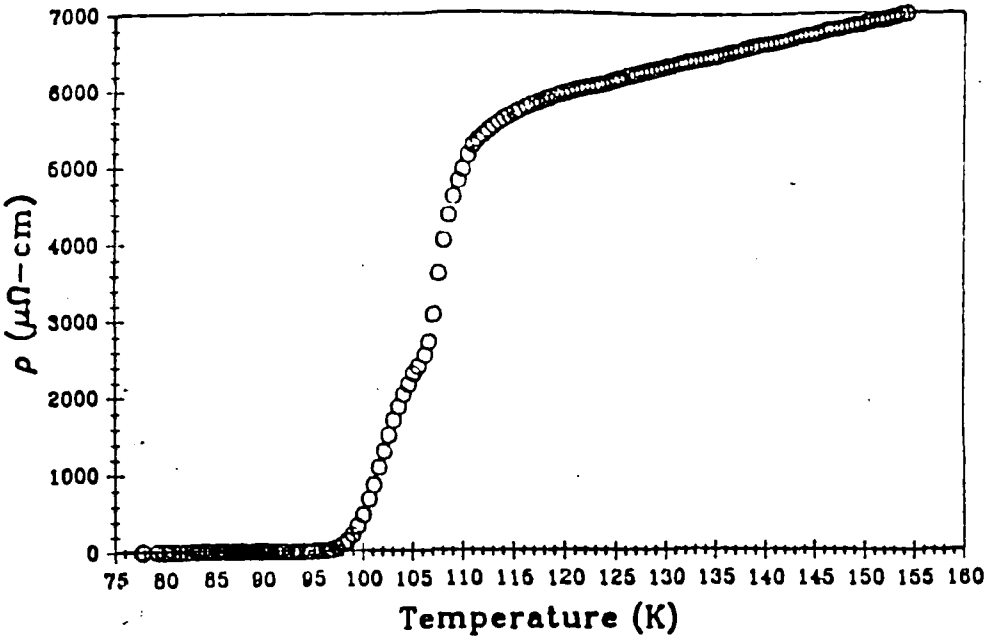


Figure 2.2.1 Resistive Transition for Bi(Pb)SCCO Tape Calcined at 775°C and Sintered at 865°C. Composition $Bi_{1.7}Pb_{0.3}Ca_2Sr_2Cu_3O_\delta$

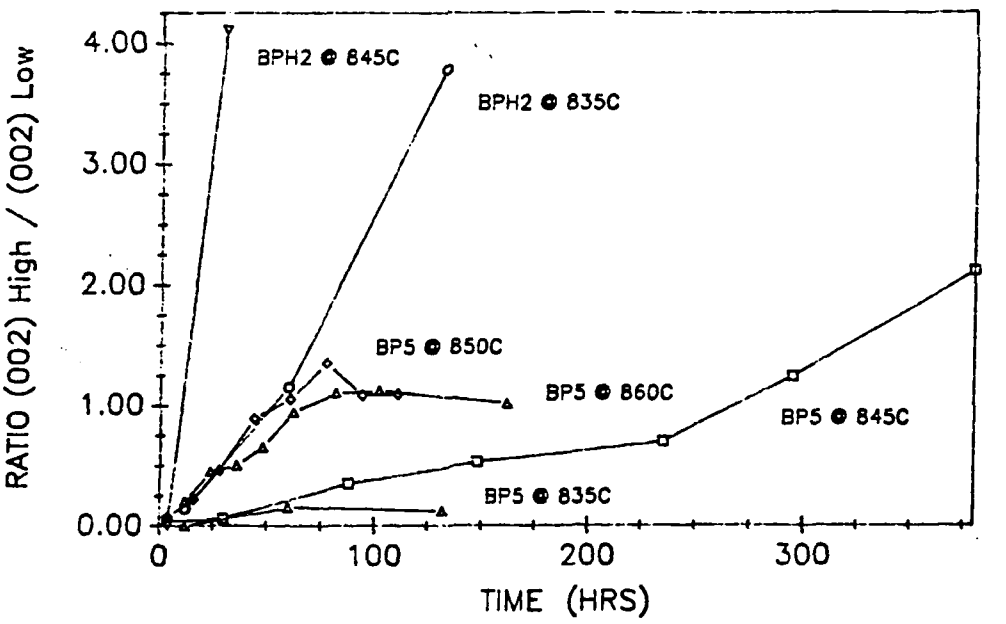


Figure 2.2.2 Peak Height Ratios for (002) Diffraction Lines for the "High Temperature" Bi-2223 Phase And the "Low Temperature) Bi-2122 Phase Versus Calcination Time and Temperature for Compositions $Bi_{1.7}Pb_{0.3}Ca_2Sr_2Cu_3O_\delta$ (BPH2) and $Bi_{1.2}Pb_{0.8}Ca_2Sr_2Cu_3O_\delta$ (BP5)

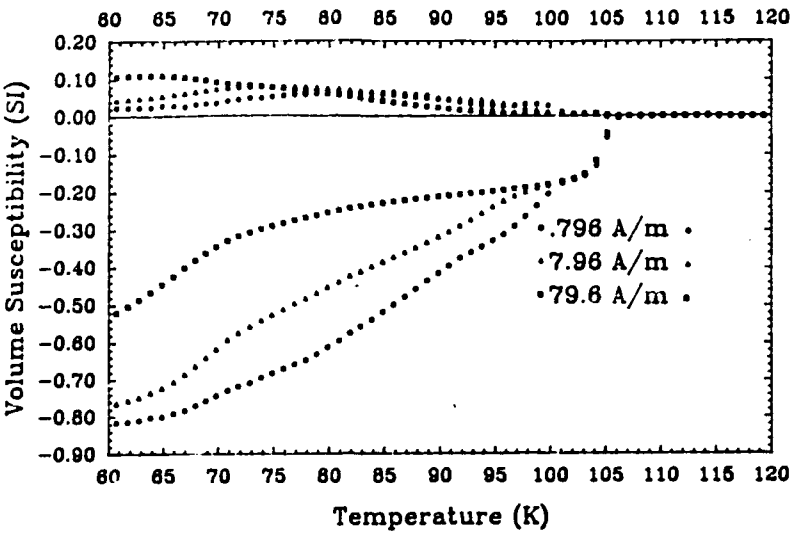


Figure 2.2.3 AC Susceptibility of $Bi_{1.7}Pb_{0.3}Ca_2Sr_2Cu_3O_\delta$ Pellet After Calcining 6 Hours at 775°C and sintering 30 Hours at 845°C. Closed Symbols: Real Part Open Symbols: Imaginary Part

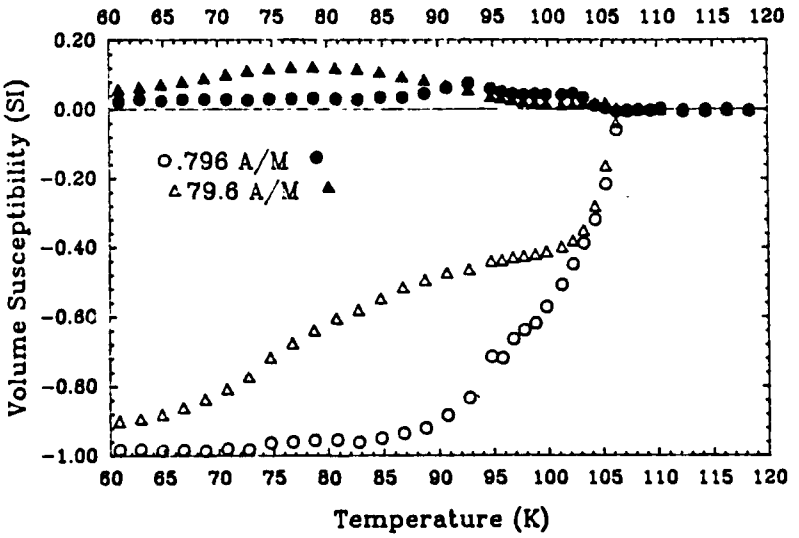


Figure 2.2.4 AC Susceptibility of $Bi_{1.7}Pb_{0.3}Ca_2Sr_2Cu_3O_\delta$ Pellet After Calcining 6 Hours at 775°C and sintering 132 Hours at 845°C. Closed Symbols: Real Part Open Symbols: Imaginary Part

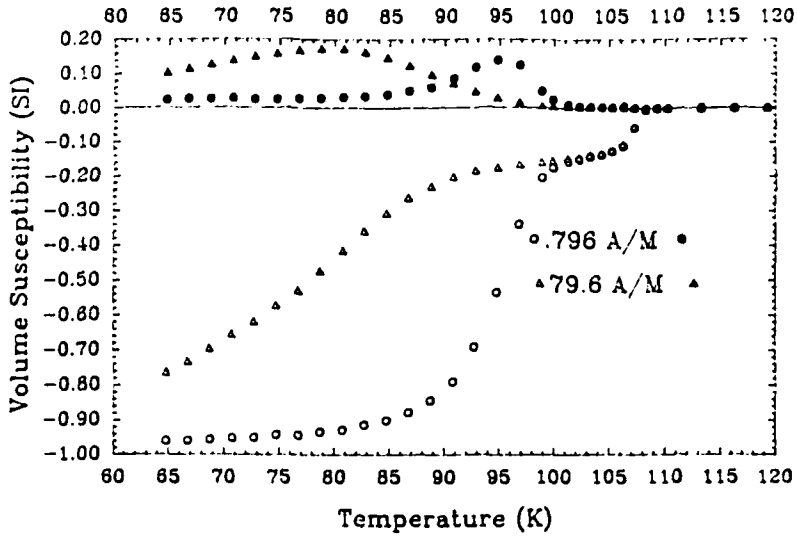


Figure 2.2.5 AC Susceptibility of $Bi_{1.2}Pb_{0.8}Ca_2Sr_2Cu_3O_6$ Pellet After Calcining 380 Hours at 845°C and sintering 30 Hours at 845°C. Closed Symbols: Real Part Open Symbols: Imaginary Part

2.2.3 Green fiber spinning

Green fiber is the starting point for our wire process. We use it as bare fiber or green clad fiber, and as monofilaments or braided multifilaments. Green fiber production and process development is done in the Albany International Research Company subcontract. A significant amount of effort occurs at CPSS to evaluate and test the fiber. The fiber is prepared to either a standard formulation or an experimental formulation as continuous monofilaments up to 3 kilometers long. Figure 2.2.6A is a photograph of a 1.5 kilometer spool prepared early this year. We now use a large diameter flanged spool, wound as neatly traversed package to despool without tangles. Figure 2.2.6.B shows two of these spools, with bare green fiber and green clad fiber.

Throughout this year our standard green fiber has been a 125-micron diameter monofilament prepared from the 1.6 micron stoichiometric powder using the high density polyethylene (HDPE) polymer system at a solids loading of 50 volume percent. We have explored the effect of changes in particle size, polymer system, and solids loading, identifying a number of promising alternatives, but have not yet found an alternative fiber with decisive advantages over our standard.

2.2.3.1 Experimental fibers

"Experimental" fibers are anything other than our standard green fibers. These include fibers with the ordinary polymer system, but a different ceramic composition to evaluate composition-property relations such as off-stoichiometric Y-123, as well as fibers made from the standard stoichiometric powder with novel polymer systems. Some of the more novel polymers systems are still being tested

with barium titanate powder as a low cost surrogate for Y-123.

Much recent effort was aimed at fibers with higher solids loading. We had some encouraging preliminary data showing acceptable spinnability and improved critical current density in sintered bare fibers from fibers at 60v% solids loading. We attempted to evaluate whether we could adopt 60 volume percent as our standard loading. A number of spinning experiments were undertaken at 60v% to further develop the higher solids green fiber. It proved to be difficult to reproduce 60v% Y-123 green fibers with the standard HDPE formulation. Spinning rates were much slower, and significant differences in spinnability were seen between powder lots. Powder lots with poor spinnability had specific surface area in the high end of our specification range ($2.3+/-0.2 m^2/gm$), while the satisfactory lots tended to the lower end of the surface area range. Subsequent work indicates that the 60 v% fibers are not easily reproduced, and often are no better than the 50 v% fibers. We have returned to the lower solids loading as our standard.

A variety of fibers were made from off-stoichiometric Y-123 compositions, for use in several sintering, rapid thermal processing, and melt texturing experiments. These included Y-123 mixed with Y-211 and Y-123 doped with 1%, 3%, 5%, and 10 wt% CuO. Composite green fibers were fabricated from 123+30 v%Ag, using a mixture of standard 123 powder and 2-micron spherical silver powder. An attempt to replace the metallic silver with $Ag_2O$ failed due to a vigorous reaction between the silver oxide and the polymer during compounding.

Several spinning runs were conducted with BiSCCO powders to produce 125-micron fiber and 1375-micron rod. The BiSCCO material is very easy to spin using the conventional HDPE formulation. Excellent fiber was produced from both hand ground powder and jet milled powder, indicating that spinnability is not

sensitive to particle size. One powder lot was used to prepare a very large quantity of fiber consisting of several 1.5 kilometer spools totaling more than 5 kilometers of green fiber.

2.2.3.2 Alternate polymer systems

High density polyethylene (HDPE) is a satisfactory carrier polymer for green fiber. It has good compounding behavior and spinnability, and provides good green strength, and acceptable binder burnout characteristics. However, it is not ideal. It supports only limited draw during spinning, so the fiber diameter cannot be made much finer than the die diameter, giving us a practical lower limit around 100 microns. Also, drawn fibers have excessive shrinkage during re-heating, which is caused by relaxation of the stretched polymer. We believe that crystalline polymers like HDPE are particularly susceptible to this relaxation problem. Finally, slow heating is required for successful burnout, which will eventually limit wire production rate. Consequently we continue to evaluate alternative carrier polymers. During this year we evaluated more than ten different polymer systems, emphasizing amorphous polymers from systems we expect might have more facile burnout. Spinning experiments were usually done with barium titanate, a surrogate we have used in place of costly Y-123 for initial trials. Many of these systems were marginally useful, some did not work at all. The most promising alternative polymer was polyvinyl butyral (PVB).

Polyvinyl butyral is an excellent carrier polymer for barium titanate, offering good green strength and much better draw. Results with PVB-based Y-123 fibers are mixed. They do offer improved draw, and so could lead to finer fiber diameters, but the "spinnability" is not as good. The PVB/Y-123 blends are not as predictable and reproducible as the HDPE/Y-123 blends. Initially it

seemed to have advantages in binder burnout, allowing faster burnout than HDPE for larger diameter fibers. More recently, however, anecdotal evidence leads us to suspect that PVB leaves a deleterious carbon residue. This may be why Y-123 fibers prepared with PVB have so far demonstrated inferior electrical properties after sintering. It appears that PVB is not useful for sintered polycrystalline wire. We plan to continue evaluating PVB, however, since the lower sintered properties may not be an important for Y-123 wires which will be subsequently melt textured, and may not be an issue for BiSCCO wire.

Acrylics and methacrylates may be promising, as certain acrylic binders are known to have particularly clean burnout in ceramics. We successfully spun flexible green fiber from an acrylic system, but the fiber had poor green strength. Several attempts were made to produce flexible fiber with methacrylates, using several new grades of polymer and lubricant but all of the methacrylate fibers have been too brittle.

2.2.3.3 Multifilament Fiber Development

Finer green fibers will make more flexible wire. Currently, monofilament green fiber cannot be practically handled at diameters finer than 125-microns, primarily because the tensile loads associated with spooling and handling break the finer fibers. The solution is to prepare multifilamentary tows of finer fibers, which distribute the handling loads onto a large number of filaments.

We have had some success on multifilament spinning using a die with six 125-micron holes. The effort was aimed at producing the fine filament diameters, so a 50 volume% barium titanate/PVB formulation with good drawdown ability was chosen. Multifilament fiber was collected continuously with diameters as small as 75 microns per filament. Preliminary sintering experiments looked good.

2.2.4 Braiding of Y-123 green fibers

A braiding machine capable of producing flat braids was obtained and set up early this year. Flat braids are more appropriate for the multifilamentary wire than the tubular round braids we had previously produced. Excellent progress has been made in handling the green fiber more gently during the braiding process, allowing the standard 125-micron green fiber to be braided without breaks. About 10 meters of a 16-filament braid were produced with bare 125-micron fiber. Figure 2.2.6A shows the 16-filament braid in the green state. A preliminary experiment indicated that the braid would could be sintered, but no further work was done on sintering of bare braids, as the filament-filament contact defeats the purpose of multifilamentary wire. The next experiment was on silver coated green clad fiber. About 540 meters of 125-micron fibers were coated as described in the following section. The green clad fiber was re-spooled onto 17 smaller spools to supply the braiding machine. Braiding was done with no fiber breaks, but the green cladding was damaged. Reformulating the coating to improve adhesion and flexibility solved this problem, so by the next attempt it was possible to prepare flaw-free braid. We have made successfully-sintered Ag-clad braids from 125-micron and 250-micron fibers. They appear to have particularly interesting electrical properties, since the transport $J_c$ is not dependent upon specimen size up to 1-meter long gage length. (See Section 2.3.6.) Most recently we have produced 68-filament braids by braiding 17 sets of four twisted 125-micron fibers. These have relatively rapid burnout (more like 125-micron fibers), but greater cross section to increase the amp rating. Figure 2.2.7B is a photo of the green 68-filament braid.

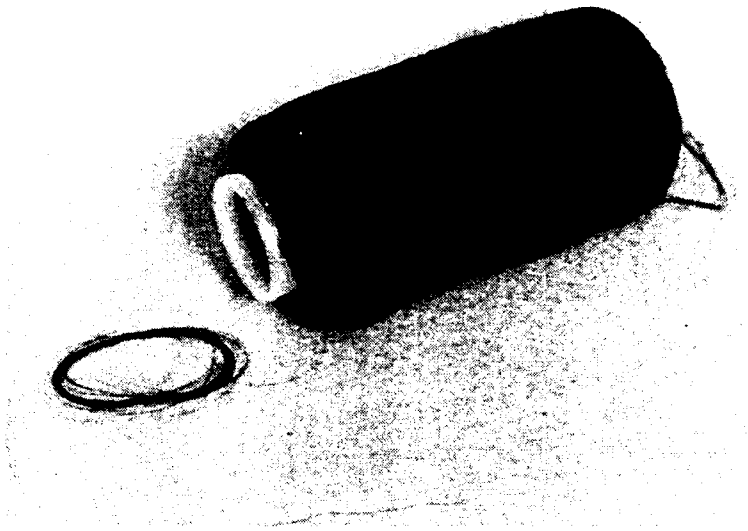

Figure 2.2.6A Photograph of 1.5 Kilometer Spool of Y-123 Green Fiber

Figure 2.2.6B Two Recent Spools of Y-123 Green Fiber
Left: Bare Fiber Right: Two Ends of Green Clad Fiber

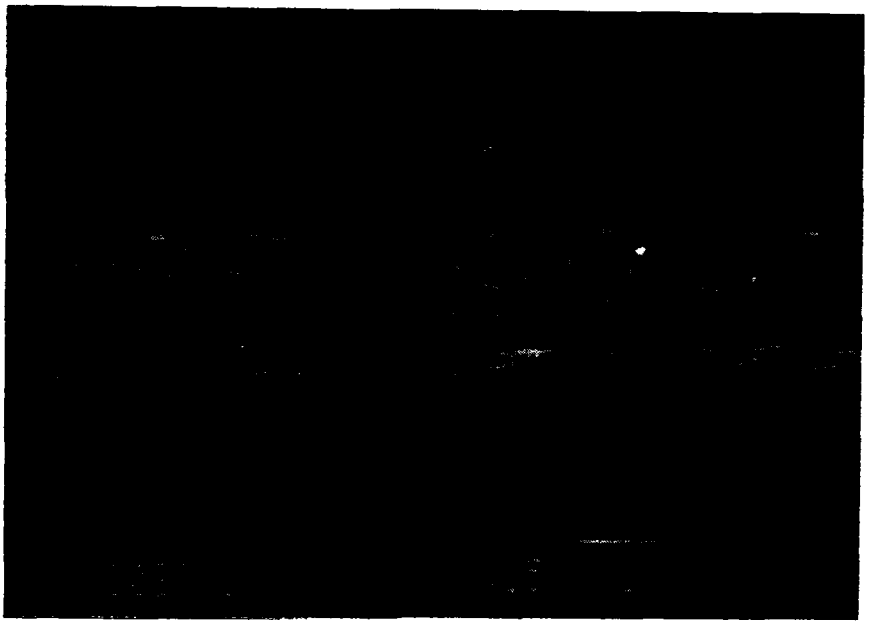

Figure 2.2.7A Sixteen Filament Flat Braid of 125-Micron Y-123 Green Fiber

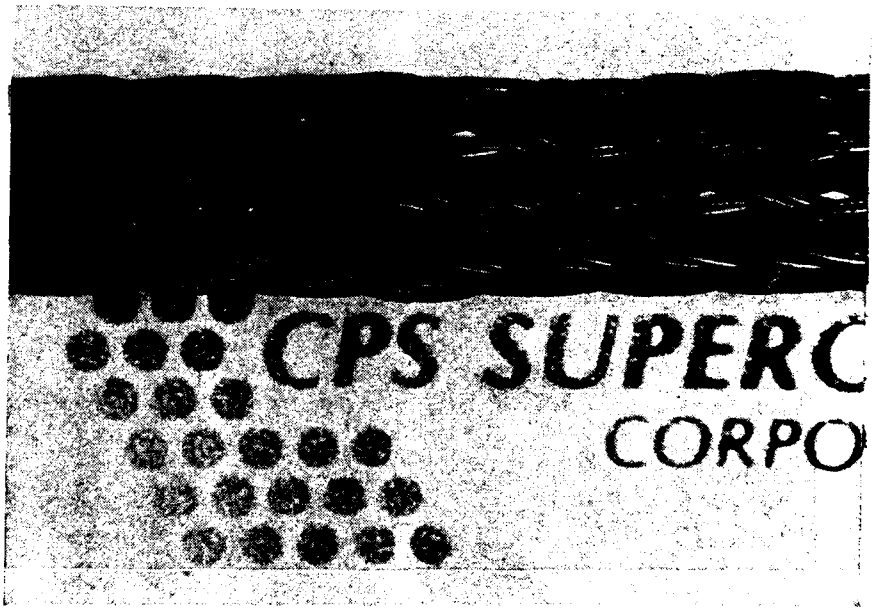


Figure 2.2.7B Sixty Eight Filament Flat Braid of 125-Micron Y-123 Green Fiber

## 2.3 Cladding and Sintering

All of our work on sintered polycrystalline wire is now involves co-fired silver alloy coated monofilaments or braids. These are made by coating the green Y-123 (or BiSCCO) fiber with a powder-metal (PM) silver alloy coating, and "co-firing" to simultaneously densify the Y-123 and the PM silver alloy. The tasks involve developing the PM coating, and determining successful burnout and sintering profiles. The "green cladding" step is done as a separate operation in which we coat up to 0.8 kilometers at a time. The clad fiber is sintered, and later oxygen annealed. Although these are separate operations, the silver coating influences the burnout and sintering, so the cladding and sintering are interrelated. We discuss them together in this Section. We also report on oxygen annealing of short wires, done in a tube furnace, and of long coils in a batch retort.

### 2.3.1 Cladding and co-firing

Since last year we have done a continuing series of reformulations of the PM silver coating materials and process, which have improved thickness, smoothness, and uniformity of the cladding substantially. The cladding apparatus has been greatly improved, so that now we can coat hundreds of meters with minimal attention by the operator. Figure 2.3.1 shows a 125-micron green fiber (on left) and a similar fiber with a 40-micron thick green PM silver coating (on right), illustrating the uniform thickness and smooth surface. The silver thickness can be easily adjusted between 20 and 100 microns, allowing variation of the metal/superconductor ratio between 1 and 8. The thickness is controlled by adjusting the applied thickness per coat and the number of repeated coatings.

The use of repeated coatings also allows us to change the composition of each layer, providing an extra degree of freedom. The improvement in uniformity arises primarily from an improved coating material which has better dispersion of the metal powder and rheology.

Process improvements have also been made to improve concentricity, insure more constant fiber motion, and eliminate vibrations. The cladding apparatus was rebuilt several times, and presently features synchronized pay-out and take-up spooling system (which produces neatly wound green clad fiber packages suitable for use in the sintering apparatus), a syringe pump to supply material to the coating tube, and an improved drying zone. These improvements permit the green cladding operation to be conducted without constant operator attention.

We have explored a large number of green claddings. We have grades with improved adherence and flexibility (formulated for braids) and other grades appropriate for monofil wire. Grades which use flaky metal powders give dense, metallurgically sound claddings, which are strong even at relatively small thicknesses. The dense claddings are hermetic, however, so oxygen must diffuse through the metal during the anneal. Other grades use spherical silver powders, which form porous claddings through which oxygen can more easily permeate. The porous claddings must be thicker for adequate strength. These are illustrated in Figure 2.3.2, comparing sintered silver coating prepared with flakey and spherical powders. We do not yet know which is better. A typical cross section of recent wire is shown in Figure 2.3.3.

Co-firing introduces several challenges. Binder burnout was at first a problem, since green clad fiber behaved differently than bare fiber. We learned how to adjust the belt speed and temperature profile for each grade of fiber and cladding. The thickness of the cladding is very important, and the more loosely

packed spherical silver powders behave differently than the densely packed flaky powders.

Surprises occurred frequently. In one episode, cladding defects appeared as occasional bare spots which were eventually identified as regions of local melting of the silver. After a while we realized that the melting occurred in the 100-400°C burnout zone (rather than the 910° sintering zone), due to local ignition of the polymer binder in the silver cladding. Quite a few "fixes" were tried before the problem disappeared, apparently due to subtle changes in the burnout profile.

Binder burnout also effects densification and grain growth in the subsequent 910°C sintering zone. The same green fiber, coated with different green claddings and then sintered with the same profile, will develop noticeably different microstructures. Gross problems occasionally arise when the microstructure is seriously degraded by liquid formation, which is probably related to retained carbon. Usually changing the cladding causes subtle changes in the microstructure, which can be overcome by tinkering with the profile.

After the high temperature exposure, the metal usually adheres tenaciously to the Y-123 filament. Sometimes incorrect sintering conditions or local damage of the coating causes cladding defects such as tears and delaminations. These were common in the early wire, and wire breaks occurred at these defects. They gradually became less frequent as we gained more experience. It is now possible to sinter about 100 meters without these defects.

Co-firing has been done with Ag and Ag/Pd coatings. Silver-palladium alloys were originally chosen to raise the melting point of the cladding above the sintering temperature of the stoichiometric Y-123 fiber. With Ag-18Pd coatings we have been able to achieve high density Y-123 after continuous

sintering at a peak temperature of 965°C in air. Attempts to sinter above 970°C have been unsuccessful, due to a reaction between Pd and Y-123 which degrades the microstructure of the superconductor. We have studied this reaction and have demonstrated that palladium promotes the peritectic decomposition of Y-123. The extent of reaction increases with temperature, time, and Pd concentration in the alloy. We have identified some sintering profiles which avoid degradation from the reaction.

More recently we have learned to densify wire with pure silver cladding. Silver is much less expensive than palladium, and high quality silver powders are more readily available. The silver claddings are strongly adherent, very ductile, and of good metallurgical quality. The disadvantage of silver is that its melting point is very close to the sintering range of our stoichiometric Y-123. We find that our silver coatings melt at temperatures greater than about 930°C in air, due to formation of the Ag-$Ag_2O$ eutectic. But under appropriate conditions, our standard fiber reaches adequate sintered density (optimal for critical current density) safely below the melting point at 910°C.

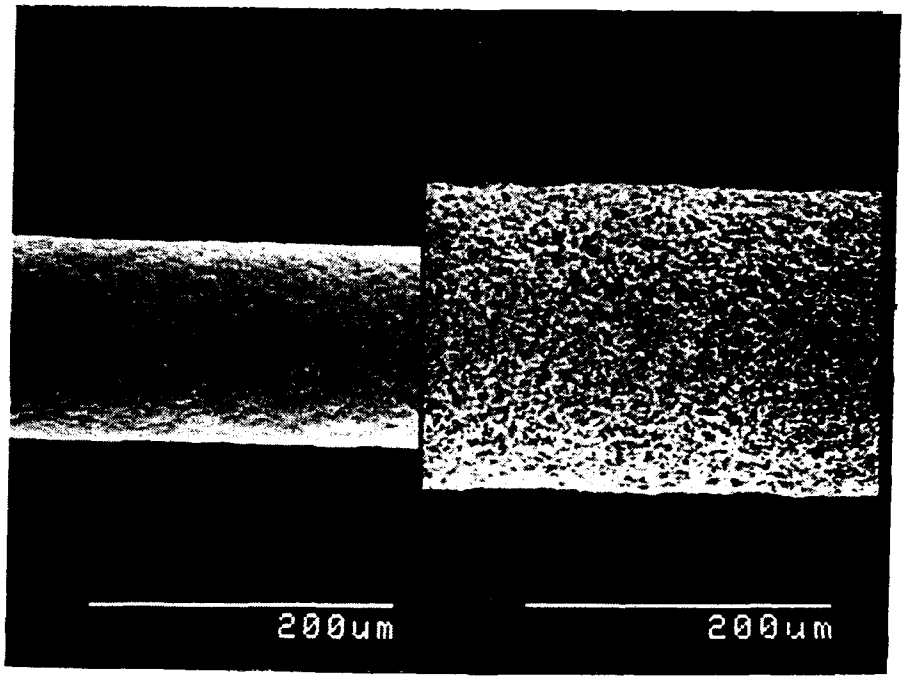


Figure 2.3.1 Green Fiber Before and After Coating With PM Silver Green Cladding

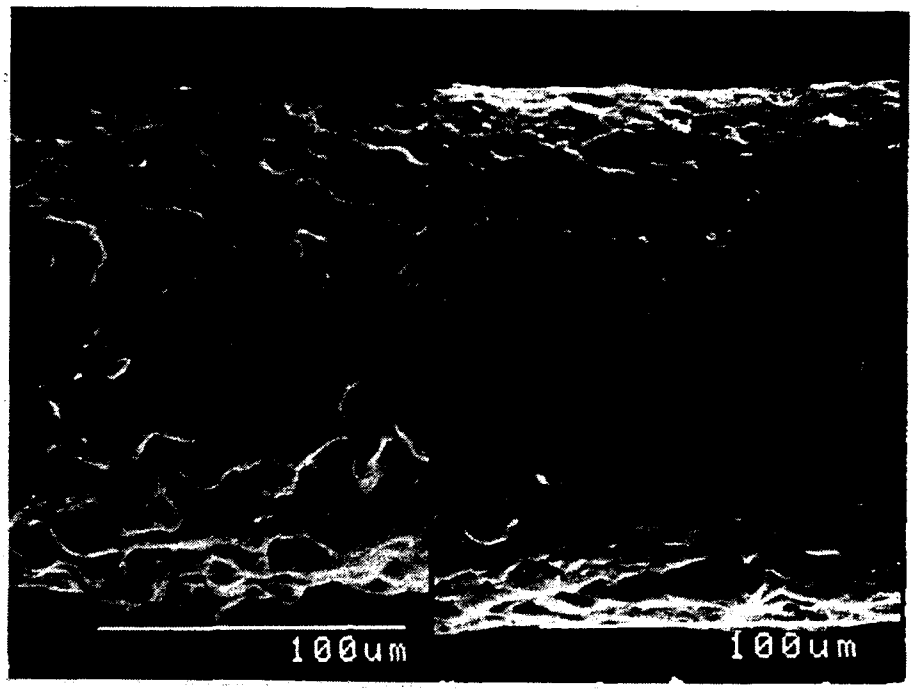


Figure 2.3.2 Comparison of the Porous Silver Coatings form Spherical Powders (left) with Dense Silver Coatings from Flakey Silver Powders (right)

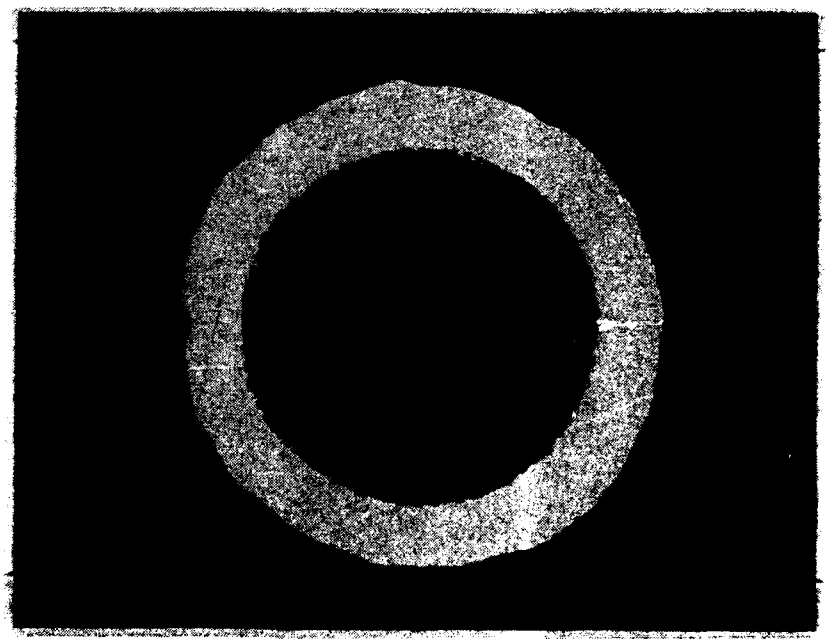

Figure 2.3.3 Cross Section of Recent Ag-Clad Sintered Polycrystalline Y-123 Wire

### 2.3.2 Continuous sintering

A larger scale facility for continuous sintering of wire was designed, built, and brought into service during the winter months. The facility features a large extension of the binder burnout section built onto the RTC furnace. The furnace extension is 3.3 meters long with five separately controllable zones with resistance heating and atmosphere control which can be independent of the RTC furnace (which now serves as the high heat section). The complete facility is about 5.5 meters long with eight heating zones. Green fibers are payed out onto a woven Nextel belt to be carried through the burnout section, sintering section, and cooling zone, and taken up on a spool at the exit. A rubber roll drive mechanism eliminated a previous problem of wear of the Nextel belt.

An important part of the sintering facility is the speed control system which synchronizes the speeds of the payout spool, take up spool, Nextel drive, and the RTC metal mesh belt drive. After these systems were installed and adjusted it was possible to run the machine unattended for long periods. In practice, the take-up spooling rate is matched to the belt speed to take up the sintered wire without slack. The pay-out spooling rate is adjusted to maintain a constant slack. The speeds of the pay-out and take-up are not the same. Usually, the pay-out speed is faster by a factor of 1.045, suggesting that the fiber undergoes 4.5% axial shrinkage during continuous sintering.

The new sintering facility worked properly on its first trial in March. The first continuous sintering run involved simple bare Y-123 green fiber to establish a baseline. We were pleased to find the sintered bare fiber was much stronger than it was with the old semicontinuous sintering treatments. We

could handle the 100-micron sintered quite easily and hold 2-meter lengths by the ends. In contrast, the bare fibers sintered according to the same schedule by the old semicontinuous method were much more fragile. In fact, the bare fiber could be easily spooled, so new take-up spooling procedures could be developed using simple bare fiber. Apparently true continuous burnout and sintering is much more gentle than our previous semicontinuous sintering method, which involved one or more intermediate spoolings of partially sintered fiber.

Production of kilometer-long continuous wire will require the sintering facility to operate 24 hours per day unattended by operators. We have made significant progress in unattended operation. One of the early attempts at unattended operation lasted two hours before a problem interrupted the run, but by the end of March we were able to run about 13 hours without an interruption. Progress has come by solving a series of problems. These have been very practical matters involving such things as guiding the green fiber from the spool to the belt, arranging for the green fiber to pay off from the spool without tangles, etc. Many difficulties were related to the neatness of the green fiber on the spools. Unlike conventional textile fibers, which can be wound with high tension to give a tight and orderly "package" on the spool, our green fibers must be wound with very low tension, so the packages were loose and prone to tangles. Our green cladding and re-spooling operations had been done by hand and wound in a random fashion. More recently we built special low tension spoolers and changed to large diameter flanged spools to produce the orderly packages we need. This has helped a great deal.

Now we often can run all day with no breaks. With the present conservative sintering profile, belt speed is slow, so production rate is

increased by using several parallel fiber lines. We routinely do two lines, although four have been successfully done (and there is room for a dozen). The longest continuous wire to date is 40 meters.[4] Longer wires, up to 166 meters long, are produced by splicing a number of smaller lengths.

### 2.3.3 Oxygen Annealing

The oxygen intercalation anneal is the last step the wire production process, and is the last one we have scaled up to long wires. Previously we have done all of our oxygen anneals as a batch process in which 5-10 cm pieces of wire and fiber were annealed in a batch furnace. Our main interest was focused on upstream process steps, so we tended to batch anneal a number of assorted samples together in "standard" anneals. Our old standards typically involved a simple isothermal anneal at 500-600°C for about 10 hours. This was effective for last year's bare fibers, but often inappropriate for silver clad wire. A laboratory tube furnace is also inappropriate for large amounts of long wire. This year we undertook a process optimization study to improve the annealing temperature-time profile, and developed a new process for annealing large amounts of spooled wire.

The process optimization work used bare fiber and wire with both the dense and porous silver claddings, each with several cladding thicknesses. We examined the effect of temperature-time profiles on the 77K transport $J_c$ and on the AC susceptibility down to 60K (the latter proved more useful). Profiles were based on a schedule as follows: 1) heat to a peak temperature and dwell; 2) first cooling ramp; 3) isothermal hold temperature and dwell time; 4) second cooling ramp; 5) power off. We found that peak temperatures of 600-650°C were

---

[4]. The break occurred when the fiber snagged on a seam in the Nextel belt.

better, and peak temperatures above 700°C were poor. We found a cooling ramp rate of 25°/hr to be satisfactory. Slower ramp rates were no better, while 50°C/hr was too fast. The isothermal hold temperatures between 350° and 400°C produced $T_c$ above 77K in 1-3 hours, while temperatures of 450°-550°C were inferior. Finally we learned that it was helpful to slowly cool after the isothermal hold down to 325°C. Several experiments involving simple slow cooling ramps also proved to be effective. From this work we arrived at our general purpose tube furnace anneal for short lengths of experimental wire: in flowing oxygen 1) heat to 670°C hold 2 hours; 2) cool at 25°C/hr to 375°C; 3) hold at 375°C for 10 hours; 4) cool at 25°C/hr to 325°C; 5) power off. This anneal, applied to "good" experimental wire, usually produces material with 1500-2000 A/cm$^2$.

The major effort in recent months was developing an annealing process for long wires on spools. The concept is to collect a large amount of sintered (tetragonal) wire on suitable refractory spools, and batch anneal one or more spools. Inconel 601 was chosen for the spools, since it has a relatively close match with Y-123 for the thermal expansion coefficient. We made the Inconel annealing spools the same size as the plastic spools used elsewhere in the process, so they are quite large: 28.3 cm diameter, 6 cm high, with a flanges about 3 cm deep. This size has the advantage that we can use our standard fixtures and speeds, and provides a large capacity. Each turn uses about 0.88 meters of wire, so a spool loosely wound one layer thick will hold 180 meters of wire. (With coils 100 layers thick, the capacity is 18 kilometers/spool). At 4.5 kilograms, the Inconel spools are rather heavy.

We anneal the spools in a large batch kiln. Since this involves a significant volume of heated oxygen, safety demands the use of a sealed retort.

We built a retort capable of holding three spools, consisting of an Inconel 601 cylindrical chamber, with oxygen inlets and outlets, and a removable lid. This was installed in a Bailey kiln. A present, the spool annealing process is only partially developed. After a number of trials, we have profile which produces wire having short-sample $J_c$ values around 500-1000 A/cm$^2$. This is typical for early stage process development, and we expect to attain values in the 1500-2000 A/cm$^2$ range shortly.

Process development is slowed by the scale of the experiments. The most recent trial used 77 meters of wire wound about 85 turns. The present annealing cycle [ 1) heat to 670°C, hold 2 hours; 2) cool at 7.5°C/hr to 300°C; 3) power off] actually requires about three days to complete because of the thermally massive furnace and retort. The present problems involve practical matters, such as leaks at seals, controller glitchs, and oxygen supply. We also need to learn how to wind (at low tension) a neat package onto the Inconel spool, and prevent it from sagging and tangling during the anneal.

### 2.3.4 Fabrication of Homopolar Motor Field Coil Segments

We have had encouraging progress winding sintered wire in the configuration of the field coils for the Emerson homopolar motor. These will require producing large amounts of annealed superconducting wire, insulating the wire, and winding it onto the bobbins supplied by Emerson. The homopolar field coils are to be wound on 1.3-cm wide, 20.4 cm diameter stainless steel bobbins made from 1-mm thick 304 stainless steel. The outside of the bobbins have 8-mm high flanges forming a channel 10-mm wide and 8-mm high to contain the wire. The design of each magnet requires six segments, each a bobbin with 500 meters of wire. We had hoped to complete at least one 776-turn/500-meter

coil segment by the end of the second year, but this is still beyond the scale of our process. At this point we have demonstrated that our process is workable by winding three experimental coils on the bobbins, with up to 30 meters of wire in the largest 45-turn coil. It is especially encouraging that the critical current density does not appear to be degraded by the winding process.

We cannot use the conventional high speed winding machines at Emerson Motor Division, since are not gentle enough to handle our relatively inflexible wire. For the prototype coils, we have designed and built a machine to wind coils from the sintered and anneal wire. The payout spool is the Inconel annealing spool (from the oxygen annealing retort) and the takeup is the Emerson bobbin. The winding machine allows both to be independently driven. We slowly transfer the wire onto the Emerson bobbin, using a manually-controlled traverse. As the wire touches the bobbin, conventional magnet wire insulating varnish is applied with a brush. This varnish serves both to insulate the wires from each other and to fix the wire permanently onto the bobbin. The varnish is cured overnight. The winding apparatus has a solder joining assembly, which we use for splicing wire and applying voltage probes. The splices consist of approximately 1-cm lap joints bonded with pure indium solder. Voltage probes are copper wires bonded to the superconductor with indium solder. Voltage taps are applied in intervals of length along the coil, typically every two or three turns. Figure 1.1.2 (Section 1) is a photograph of the second coil, showing the bobbin with eight terminals for current leads and voltage taps. In this photograph, the eleven turns of superconducting wire are barely visible in the channel.

The first coil trial -- coil 1 -- used 3.8 meters of wire, with one

splice near the end of the wire. Unfortunately this wire became tangled on the Inconel annealing spool, and was damaged as it was unwound. The tangling was related to the fact that the wire was not uniformly traversed onto the spool as it was taken up from the sintering furnace, resulting in a rather messy "package". Further, is was not adequately secured, so the wire moved as the spool lay on its side during the oxygen anneal.

The current density of the wire in coil was measured in liquid nitrogen over five different areas. In one 86-cm long section, covering 1.3 turns, the critical current density was 500 A/cm$^2$, which was comparable short samples of the wire. Figure 2.3.4 shows the E vs. J data for this 86-cm segment. In the other four segments, $J_c$ varied from 56 to 120 A/cm$^2$, reflecting the damaged caused when the tangled wire was unraveled.

The next coil- coil 2 - was made from wire which was uniformly traversed upon pickup after sintering, so was not tangled after the oxygen anneal. We were able to pay out this wire from the annealing spool and place it onto the bobbin without apparent damage. Unfortunately, this batch of wire was poor due to a failure of the oxygen supply during final stages of the anneal. The short sample critical current density was only 100-400 A/cm$^2$. Coil 2 was made from 7.14 meters of wire, coming to 11 turns of wire (each turn uses 64.4 cm of wire). This coil was more uniform. The critical current density, measured over a 7.14 meter gage length was 106 A/cm$^2$. Figure 2.3.5 shows the E-J characteristic for the entire coil, and five individual segments within the coil. Except for one short segment, the critical current densities range between 88 and 138 A/cm$^2$. The slopes in the post-$J_c$ range, however, are quite different.

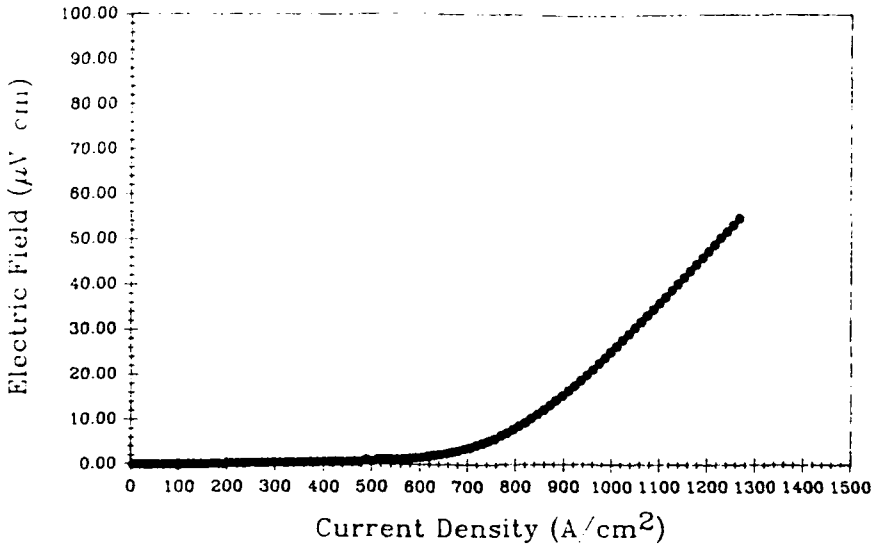


Figure 2.3.4 Electric Field vs. Current Density for a 1.3-Turn, 0.86 Meter Long Segment in the Center of Coil 1, Showing a $J_c$ of 500 A/cm$^2$

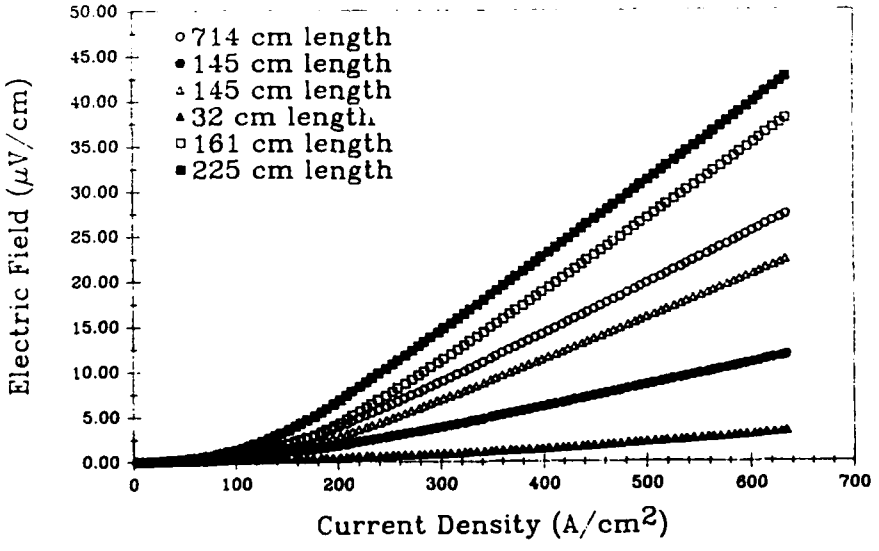


Figure 2.3.5 Electric Field vs. Current Density for the Entire 11 Turns, 7.14 Meters of Coil 2 and Five Partial Segments

### 2.3.5 Properties of SP Wire

#### 2.3.5.1 Mechanical Behavior

The 125-micron diameter for the fiber was chosen to be fine enough to wind around a 10-cm radius of curvature without damage. Fracture occurs at a bending radius around 4 centimeters for bare fibers. The silver cladding increases the strength, but should not significantly change the flexibility, since the brittle core inside the cladding will fail. If the cladding is thin ( 5-microns for dense silver), clad wire breaks in a typically brittle fashion. Thicker claddings (eg. 20 micron dense silver or 30 micron porous silver) impart apparent ductility to the wire. The wire appears to be ductile, and can be bent plasticly like an ordinary metal wire, without causing fracture. Inside the wire, however, the brittle Y-123 core fractures, so the damage threshold in flexure for clad wire is similar to the bare fiber.

We are beginning to collect mechanical property information on the sintered polycrystalline wire made from the 125-micron diameter fibers. We would like to know the threshold load and stress level at which the electrical properties are degraded. We have not done that yet. So far we have only examined the fracture properties under tension.

Tensile measurements have been made on sintered wire (before oxygen annealing) by determining the fracture load for single wires. A tab-card method is used to avoid problems with gripping a fine filaments. A 7.5-cm sample of wire or fiber is tabbed by bonding the top and bottom 2.5-cm of the sample to a card with an acrylic adhesive, with the center section free. The card is mounted in the test fixture, so that the card, rather than the wire, is gripped. The tab card between the adhesive bonds is removed, exposing the free

center of the fiber. Fiber gage length is 6 mm. The fiber is loaded until fracture occurs.

Figure 2.3.6A shows the distribution of loads at fracture, plotted as a Weibull distribution, for 100-micron diameter bare Y-123 sintered fiber, and co-fired wire with either a 48-micron thick cladding of porous silver (from the spherical silver powder) or a 23-micron thick cladding of dense silver (from flaky powder). The bare fiber has a median breaking load of 80 grams. The dense silver cladding doubles the median load to 165 grams. The porous silver cladding, while much thicker, only increases the median load at fracture to 135 grams. The same data, converted to strength by dividing by the total cross sectional area, appears in Figure 2.3.6B. This shows the bare fiber with a median strength of 74 MPa, over a range of 60-130 MPa (which is similar to previously reported indirect measurements[5]). The wires with the dense silver cladding have a similar median strength as the bare fibers. The thick porous silver cladding significantly reduces the strength.

---

[5]. Recall that First Annual Report presented some strengths inferred from the bending fibers until they fractured. Strain at fracture was calculated from the bending radius, and converted to strength using an elastic modulus of 131 GPa. The resulting "strength" values ranged from 109-187 MPa.

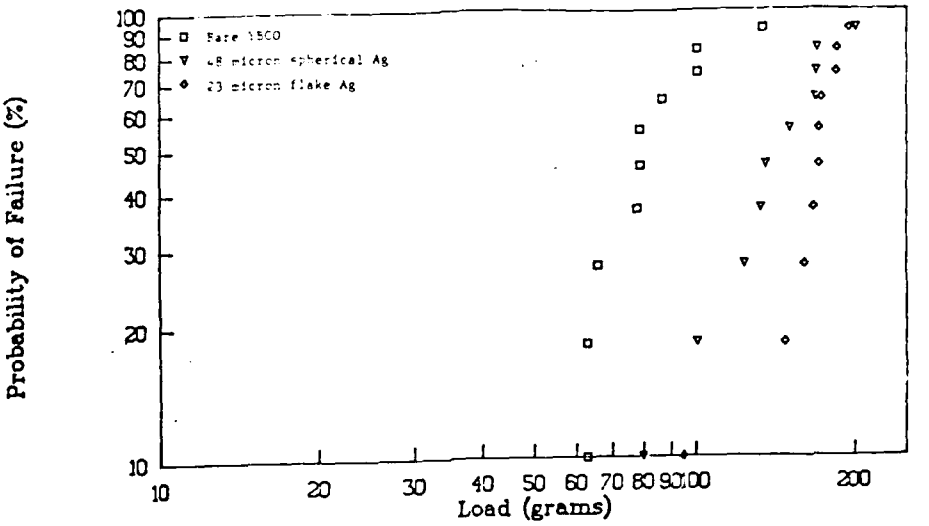


Figure 2.3.6A Tensile Properties of Sintered Y-123 Wire, Comparing Load at Fracture Distributions for Bare Fiber, Wire with 23-Micron Thick Cladding of Dense Silver, and a Wire with 48-Micron Thick Cladding of Porous Silver

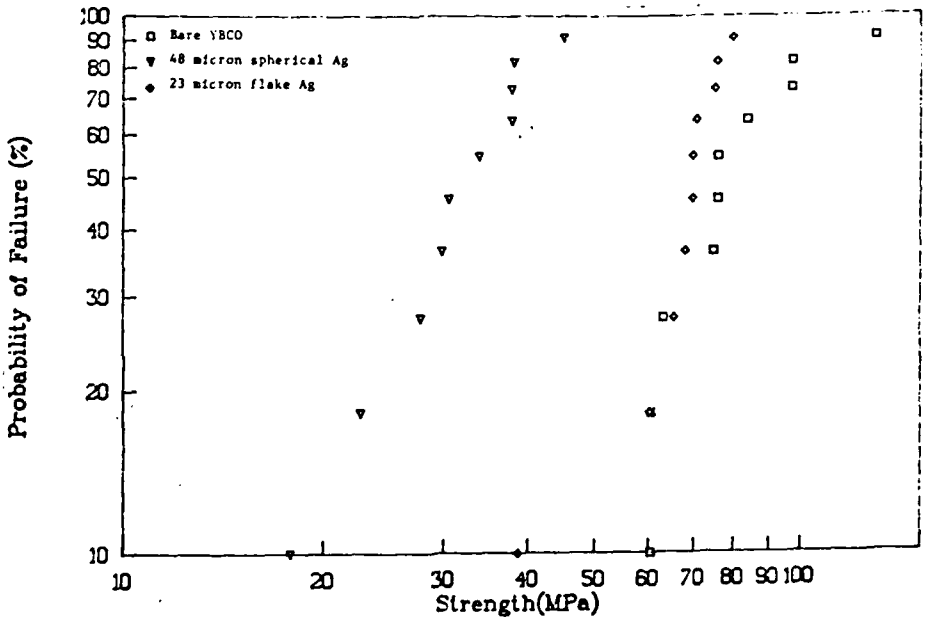


Figure 2.3.6B Tensile Properties of Sintered Y-123 Wire, Comparing Stress at Fracture Distributions for Bare Fiber, Wire with 23-Micron Thick Cladding of Dense Silver, and a Wire with 48-Micron Thick Cladding of Porous Silver

2.3.6 Processing of BiSCCO Fiber and Wire

During the last quarter we have began to apply our fiber process to the BiSCCO system. Using an early composition and calcining process, we produced about a kilogram of $Bi_{0.7}Pb_{0.3}$-2223 powder to enable the spinning of a spool of 125-micron BiSCCO green fiber. With this fiber we were able to demonstrate each of the process steps for sintered wire. About 30 meters of BiSCCO fiber were green clad with 25 microns of spherical silver. A 10 meter sample of green clad fiber was continuously sintered at a peak temperature of 840°C, which resulted in a coherent silver clad wire. The wire was used as feedstock for experiments on anneals aimed at developing the 110K 2223 phase, but we were unable to achieve zero resistance from this early grade of wire. Subsequent experiments with small lots have resulted in zero resistance tapes above 100K, as reported in Section 2.2.2. Early experiments with the SP BiSCCO wire demonstrated that the silver clad wire could be cold rolled to make a tape shaped wire. This was very encouraging, and forms the prototype of our future activities with this material. Figure 2.3.7 shows the BiSCCO wire in each stage of the process. We expect to produce rolled tape BiSCCO wire from monofilament wire and as multifilamentary tape by rolling braided wire.

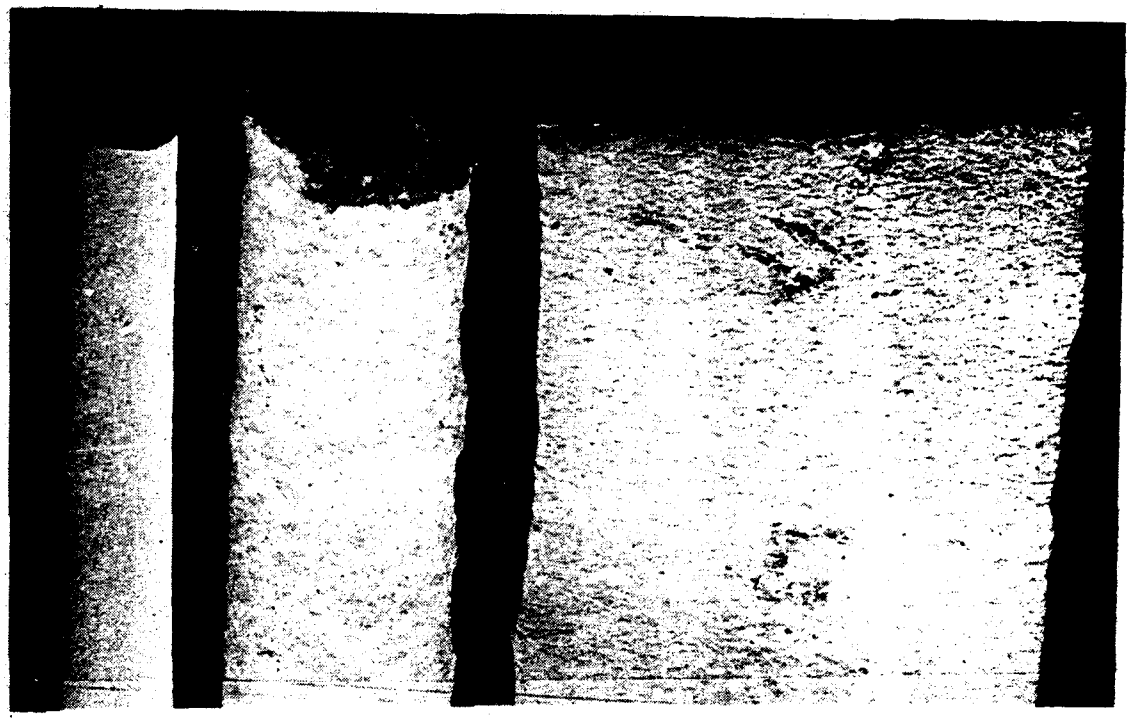

Figure 2.3.7 Stages in the Production of Prototype BiSCCO Wire. From Left: Green fiber, Green Clad Fiber, Sintered Wire after Rolling

2.3.6 Braided Sintered Wire

The multifilamentary braided wire is made by co-firing green clad braids in the continuous sintering facility. With the finer 125-micron green clad fiber, braids have been sintered in a continuous mode. Slower belt speeds are used with braids since binder burnout is more difficult. Most of the recent work has used 250-micron green fiber which, in a braid, requires inconveniently slow belt speeds for binder burnout[5]. In those cases, we used the burnout section of the furnace as a long batch oven. Green braids up to 1.5 meters long were fed into the burnout section while the furnace was cold. Once inside, the entire length of the burnout section was uniformly heated according to the burnout schedule. Once burnout was complete, the belt drive was started to transport the braid through the high temperature sintering section. Thus the braid was burned out in a batch mode, but sintered continuously. Meter-long sintered braids were then oxygen annealed, again using the burnout section as a batch oven.

Figure 2.3.8 shows the seventeen filament braid of after continuous sintering. Each filament retains its identity, and is insulated from other filaments by the silver cladding when the filaments are in the superconducting state. The critical current density, around 1000 A/cm$^2$, is similar to the monofil wire. The critical current for these 17-filament/250-micron diameter braids is 8-10 amps, reflecting the larger cross section, which is an attractive feature of the multifilamentary braids. More importantly, the critical current of the braids do not depend upon gage length of the wire.

---

[6]. The recent 68-filament braids made with 125-micron fiber (Section 2.2.4) are an effort to make binder burnout fast enough to accomplish continuous sintering, while keeping the same conductor area as the 17-filament/250-micron braids. Preliminary results are encouraging.

Measurements have been made over gage lengths between 1- and 103-cm, with identical results. Moreover, a wind-and-fire coil made from braids was uniform over all of its turns. These results are discussed in Section 2.4.2.

We have measured the transport properties of the braids over gage lengths around one meter, and were pleasantly surprised to find that the braids have no gage-length effect on the critical current. Figure 2.3.9 presents the electric field vs. current density data at 77K for a long silver clad braid, showing that the middle 50-cm section has the same E-J behavior as the entire 106-cm length. This contracts sharply with the monofilamentary wire, which has significantly lower $J_c$ in longer gage lengths, reflecting the effect local "bad" sections along the length of the fiber.See Section 2.4.6). Apparently there is a beneficial averaging effect by having 17 filaments in parallel. There also may be current transfer through the silver cladding from one filament to another, which could allow local bad sections of any particular filament. The behavior of the braids in magnetic fields is similar to the monofil sintered wire. This data appears in Figure 2.3.10, showing the usual drop in $J_c$ as weak links are extinguished in the 1-1000 gauss range, followed by a residual strong linked fraction beyond 1000 G. The residual $J_c$ for this braid specimen is more than twice as high as our monofil wire, but this may not be significant.

The gage length effects observed with monofil wire were worrisome, since coils require very long wires. We were unable to wind coils from sintered braids, since they were too rigid, so we attempted to make coils with a wind-and-fire technique. This worked well. By winding some of the 17-filament green clad braid around a mandrel, we made a small test coil (3.5 cm diameter by 6 cm high) with 8 turns. Figure 2.3.11 shows the and E vs. J for the braided coil. Once again there is no length effect, as the center two turns

behave the same as the full eight turns. The coil had a critical current of 2.8 amps (or about 335 $A/cm^2$), producing about 28 gauss. This is approximately what would be expected by interpolating the $J_c$ vs. B data of the straight braids. The coil behaved the same in three separate tests.

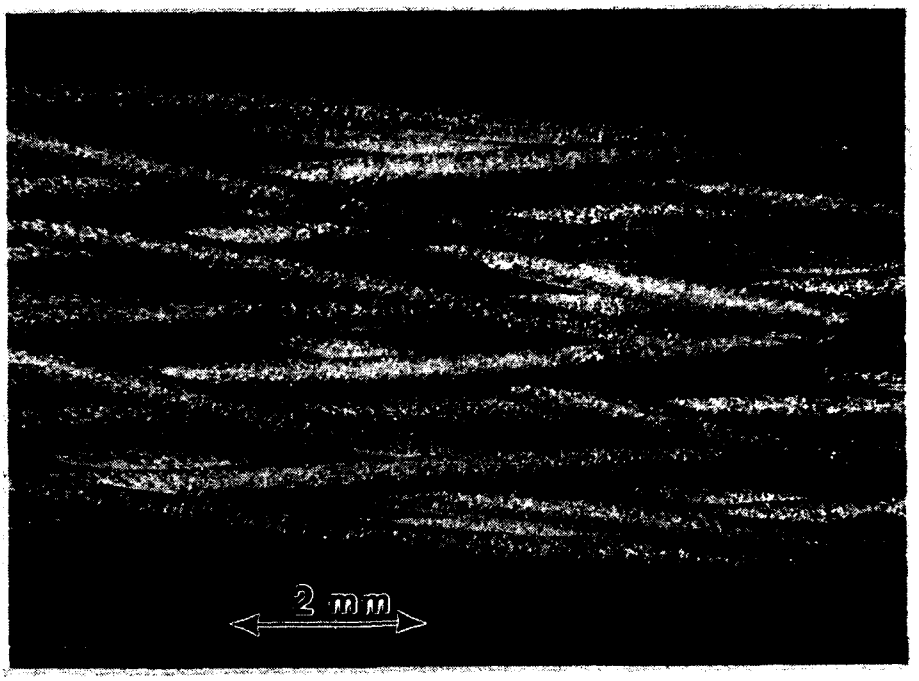


Figure 2.3.8 Seventeen Filament Braid of Silver Clad Polycrystalline Y-123 Wire Continuously Sintered using Braided Green Clad Fiber

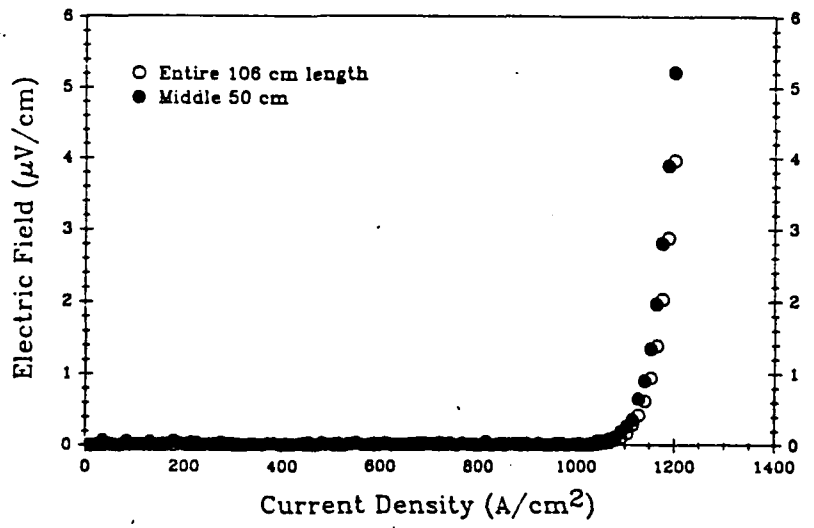


Figure 2.3.9 Electric Field vs. Current Density at 77K for Seventeen Filament Braid Silver Clad Polycrystalline Y-123 Wire, Comparing the Middle 50-cm Section with the Entire 106-cm Gage Length

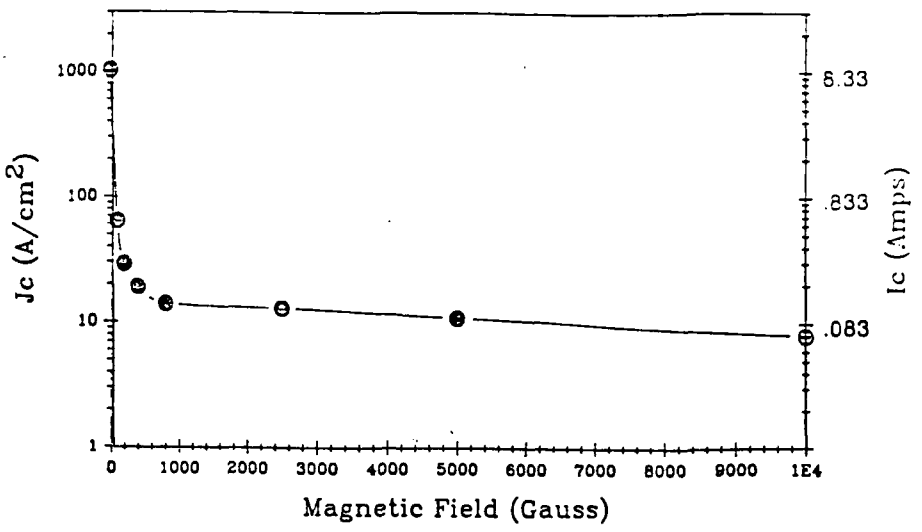


Figure 2.3.10 Critical Current Density vs. Magnetic Field at 77K for Seventeen Filament Braided Silver Clad Polycrystalline Y-123 Wire

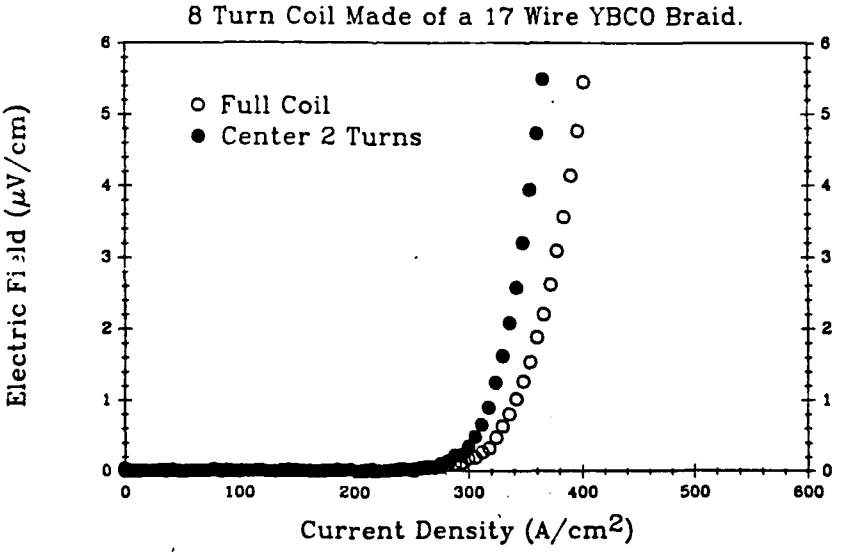


Figure 2.3.11 Electric Field vs. Current Density at 77K for 8-Turn Coil Made With Braided Silver Clad Polycrystalline Y-123 Wire, Comparing the Central Two Turns with Complete Coil

## 2.4 Electrical Characterization

The effort in electrical characterization was predominantly the determination of self field transport critical current densities in support of the wire development effort. This involved more than 800 measurements on mounted short wire and fiber samples, largely serving to evaluate the effect of processing conditions upon properties. A number of studies were undertaken to examine effect of specimen length and the specimen-to-specimen variability in the transport data. Selected specimens were characterized in applied magnetic fields up to one tesla. Magnetic susceptibility measurements were made using an AC Susceptometer to obtain the real and imaginary susceptibility down to 70K.

The self field 77K $J_c$ values of the sintered polycrystalline wire ranged up to 2800 A/cm$^2$, with "good" wires in the range of 1500-2000 A/cm$^2$ for short samples. It is hard to define a typical wire, since the wire and process was continually progressing throughout the year. With each major upgrade in the process, the early self field $J_c$ would drop to the 100-500 A/cm$^2$ range (or even become resistive), and gradually recover to the 2000 A/cm$^2$ range after about a month of development work. This was true when we progressed from short bare fibers sintered in the tube furnace to meter-long fibers in the RTC furnace; when we moved from meter-long pieces to semi-continuous fibers; from bare fibers to clad wire; from semi-continuous to true continuous; from thin to thick silver cladding. There was always a lag between the older (better understood) process yielding wire in the 1500-2000 A/cm$^2$ range and the newer (less understood) process, which gives temporarily poor electrical performance. Most recently we have progressed to oxygen annealing up to 70 meters of

sintered clad wire on a spool. So far the spool-annealed wire has $J_c$ in the 100-500 A/cm$^2$, but is steadily improving.

### 2.4.1 Measurement Technique

Short wire or fiber specimens are suspended on free-standing 5-mil copper lead wires, which connect to the pins of a standard fixtures with four copper wires attached to a connector. Specimens are placed on the wire and attached with silver paint, with voltage tap separation of 15-20 mm. Part of the fixture is shown in Figure 2.5.1. This method allows convenient measurement of fine fiber specimens.

Contacts to metal clad co-fired wires are simply made with commercial silver paint, and seem entirely satisfactory. Contacting bare fibers is done by painting silver pads to sintered filaments, which are subsequently re-fired to mature the silver pad. Some difficulties are occasionally still encountered when we make contact with bare fibers.

Figure 2.4.1 illustrates the E-J characteristics of good examples of the co-fired wire and bare Y-123 filaments, respectively. The current density in the clad wire is calculated on the cross-sectional area of the Y-123 core, rather than the net wire diameter. These represent the best performance to date on materials sintered as meter-long specimens. The difference in the E-J curves in the flux-flow region beyond the critical current density is related to current sharing in the silver cladding of the wire.

### 2.4.2 Critical Current Density in Applied Magnetic Field

Magnetic field measurements are routinely done on clad wire and bare filament to supplement the self field data. Standard practice is to determine

$J_c$ at 100 G for all specimens with a self-field value above 1000A/cm$^2$. The full $J_c(B)$ characteristics is determined for selected specimens. Figure 2.4.2 and 2.4.3 are examples of a recent clad wire and bare filament. For the bare filament, critical current density drops rapidly from the 2200A/cm$^2$ value at self field to about 10/cm$^2$ at 100G, then gradually drops to 5A/cm$^2$ at 1000G. This value is still above the lower limit of measurable values for our apparatus.

2.4.2 Magnetic Susceptibility

Magnetic susceptibility data on our sintered filaments were taken with a Lake Shore Cryotronics Model 7000-1 AC Susceptometer. This instrument has become a workhorse in our laboratory. The specimen is typically several filaments mounted coaxial with the magnetic field, although we are able to measure a single filament. Volume susceptibility at 200 Hz is calculated on a sample volume on the order of a few tenths of cubic millimeters (corresponding to a sample mass around a milligram). Typically the measurements are done a 1G or 0.1G.

2.4.2 Statistical and Spacial Variations in Critical Current Density

We have observed specimen-to-specimen variations and within-specimen variations in $J_c$ for bare Y-123 filaments and Ag-clad wires. The intent was to examine a rather large sample of "identical" wires and look at gage length effects in longer wires. The study was done on a large lot of wires with a 10-micron thick porous silver cladding made with the spherical silver powder. Unfortunately, this particular wire lot was rather low quality, so most of the transport $J_c$ values were around 500 A/cm$^2$.

Green clad fiber was sintered continuously according to the standard profile, with the peak sintering temperature zones corresponding to 30 minutes at 920°C. The 3-meter long sintered wire was cut into a large number of "small" pieces (for 2-cm. gage length tests) and "long" pieces (for multiple contact experiments up to an 8-cm gage length). All of the wires were annealed together in a tube furnace for the then-standard oxygen anneal: heat to 830°C; ramp down to 520°C at 50°C/hr; dwell 10 hours at 520°; furnace cool. The short wires were mounted for conventional 4-point measurements, and the long wires were mounted with six contacts, allowing 4-point measurements to be taken over 2-,4-, and 8-cm gage lengths.

The specimen-to-specimen scatter in $J_c$ values fit a normal distribution. Figure 2.4.4 shows the distribution function for the 2-cm gage lengths data from the short wires. The mean is 730 A/cm$^2$ with a standard deviation of 77 A/cm$^2$. This can be compared with the long wire data over the 2-cm gage length. One expects these to be identical, but Figure 2.4.5 shows a significantly lower mean of 550 A/cm$^2$ and a larger standard deviation of 182 A/cm$^2$. It is surprising that 2-cm segments of long wires could be different from 2-cm segments of short wires.

The long wire data shows that longer segments tend to have lower mean $J_c$ values and less scatter, as might be expected. This appears in Figure 2.4.6, comparing the 2-cm, 4-cm, and 8-cm gage lengths based on the multiple contacts experiments on three long wires.

The multiple contact wires provided an opportunity for exploring spacial variations three of these wires. Figure 2.4.7 illustrates the values obtained

when $J_c$ was measured over five of the combinations for 4-point measurements.[7] This shows variations of more than a factor of two from one location to another. For example, in wire #3, the first 2-cm segment (2-3) had a $J_c$ of only 255 A/cm$^2$, while the next 2-cm segment (303) carried 624 A/cm$^2$. We are investigating the origin of this variation.

The longer gage length critical current density is not quite the same as the lowest local $J_c$ value. Although the criterion for $J_c$ is an electric field of 1 microvolt/cm, one actually measures the potential difference between two leads, and uses the gage length to obtain an average field $E_{av}=\delta V/L$. To illustrate the difference we have in Figure 2.4.8 the actual voltage differences measured at the 4 taps on one of the long wires. The upper right plot shows the distribution at a current density of 305 A/cm$^2$ (well below the critical current density for the wire). Notice that three sections have zero resistance, while the left segment, at an average field of 1.5$\mu$V/cm, is beyond the criterion. At a higher current density of 407 A/cm$^2$ (upper right) the whole wire is near its $J_c$. The middle segment, however, is still at zero resistance. This persists at 509 A/cm, with the center still superconducting while the wire is well beyond $J_c$. Finally, notice that the voltage distribution is still nonuniform at 1005 A/cm$^2$, even though the current density is far beyond the $J_c$ of all segments.

The causes of the spacial variation and specimen-to-specimen variations are still obscure. We have, however, that the self field transport $J_c$ correlates well to the real AC volume susceptibility at 77K. Figure 2.4.9 shows the transport critical current densities plotted against susceptibility

---

[7]. Each wire had six leads. Leads 1 and 6 were used for current leads, while we measured the voltage across lead pairs 2-3, 2-4, 2-5, 3-4, and 4-5. Each $J_c$ corresponds to the usual 1 microvolt/cm criterion.

for a variety of wires, including bare fiber, porous silver, and dense silver cladding of various thicknesses. If one can attribute the volume susceptibility to the fraction of superconducting phase, the interpretation is that the extent of oxygenation (and therefore fraction of superconducting phase) dominates the transport data. This supports the idea that variations in $J_c$ arise from differences in oxygenation.[8]

In sharp contrast to monofil wire, we find that the critical current of multifilamentary braids does not depend upon the gage length of the wire. Measurements have been made over gage lengths up to 103-cm are identical with 1-cm gage length results. Moreover, a wind-and-fire coil made from braids was uniform over all of its turns. (These results were discussed in Section 2.3.6.) Apparently there is a beneficial averaging effect by having many filaments in parallel with current transfer through the silver cladding between HTSC filaments to circumvent any local bad sections.

Very long wires are required to make coils, so the gage length effects we have observed with monofil wire are very bad news. Clearly multifilamentary wire is preferred for long coils, so it is encouraging that we have been able to make prototype coils a wind-and-fire technique. In the long run, however, we need to develop either melt textured monofil wire that has no gage length effect, or else a flexible multifilamentary melt textured wire.

---

[8]. An alternative reason for the correlation relates to weak link behavior. The susceptibility might not be so simply related to "volume fraction superconductor" for a weak link material, since the measured susceptibility is lowered by weak links. If both $J_c$ and susceptibility are dominated by the severity of the weak links, the correlation provides no useful information.

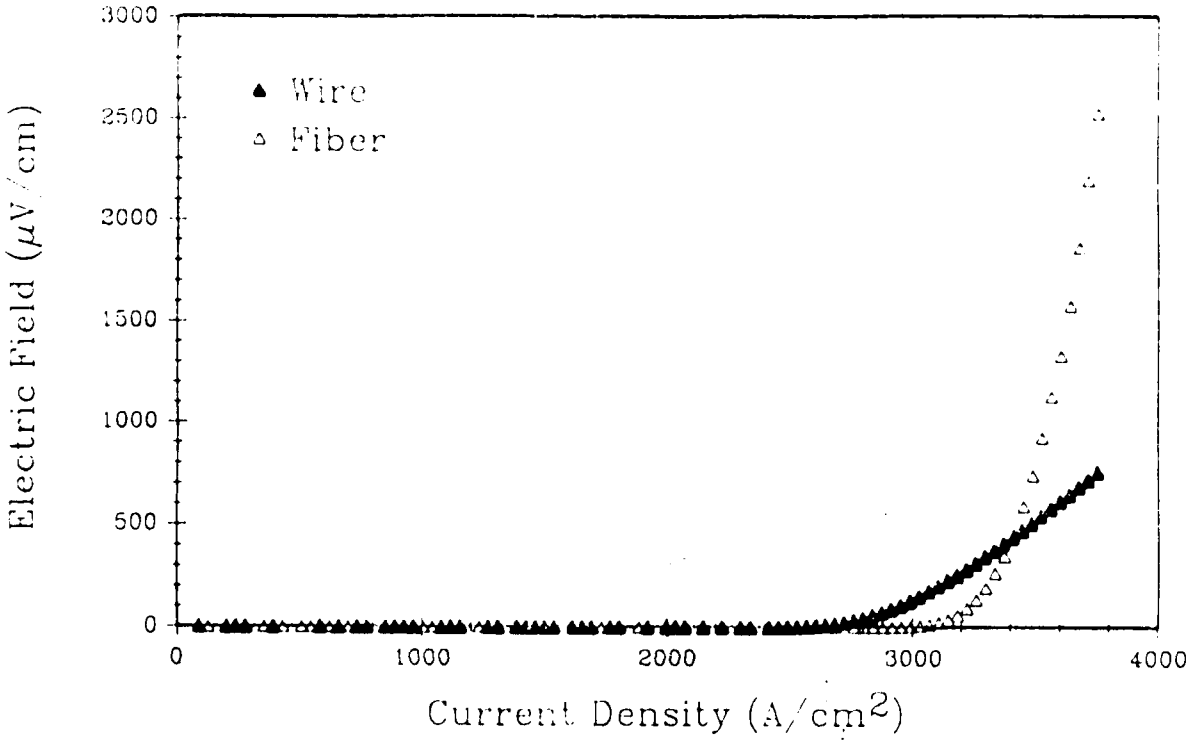


Figure 2.4.1 Electric Field vs. Current Density at 77K in Self Field for Bare Filament and Clad Wire

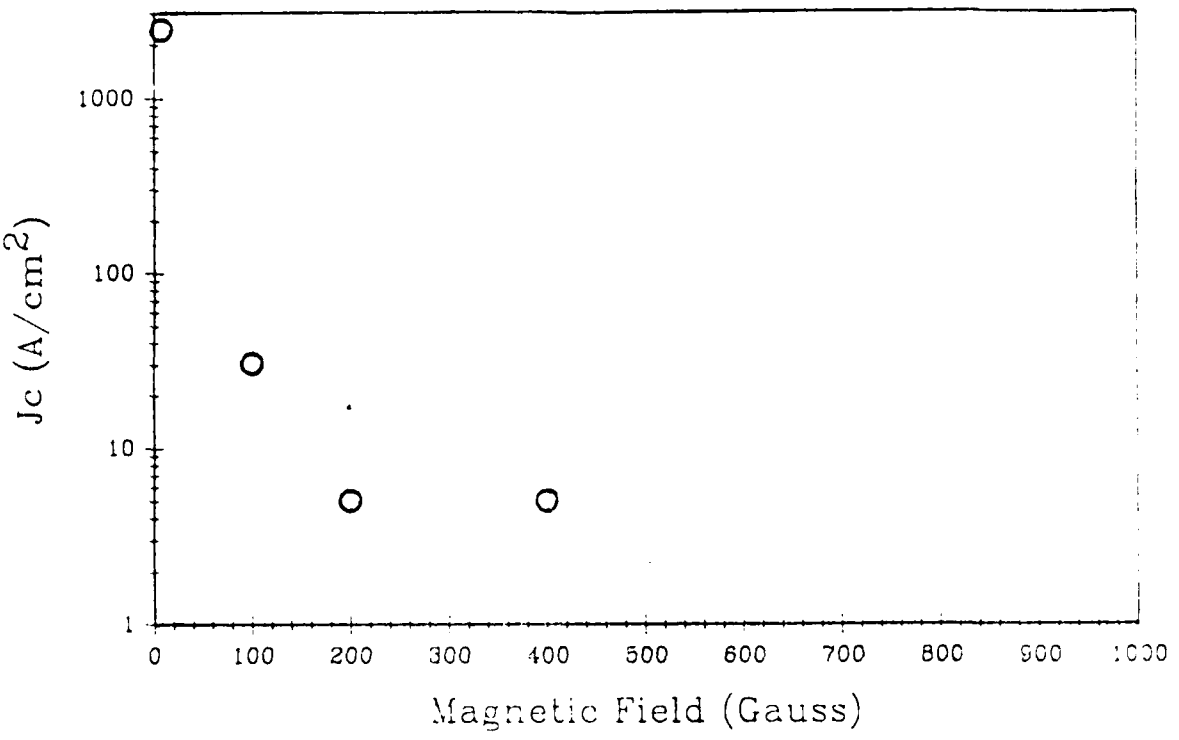


Figure 2.4.2 Critical Current Density vs. Magnetic Field for Clad Wire at 77K

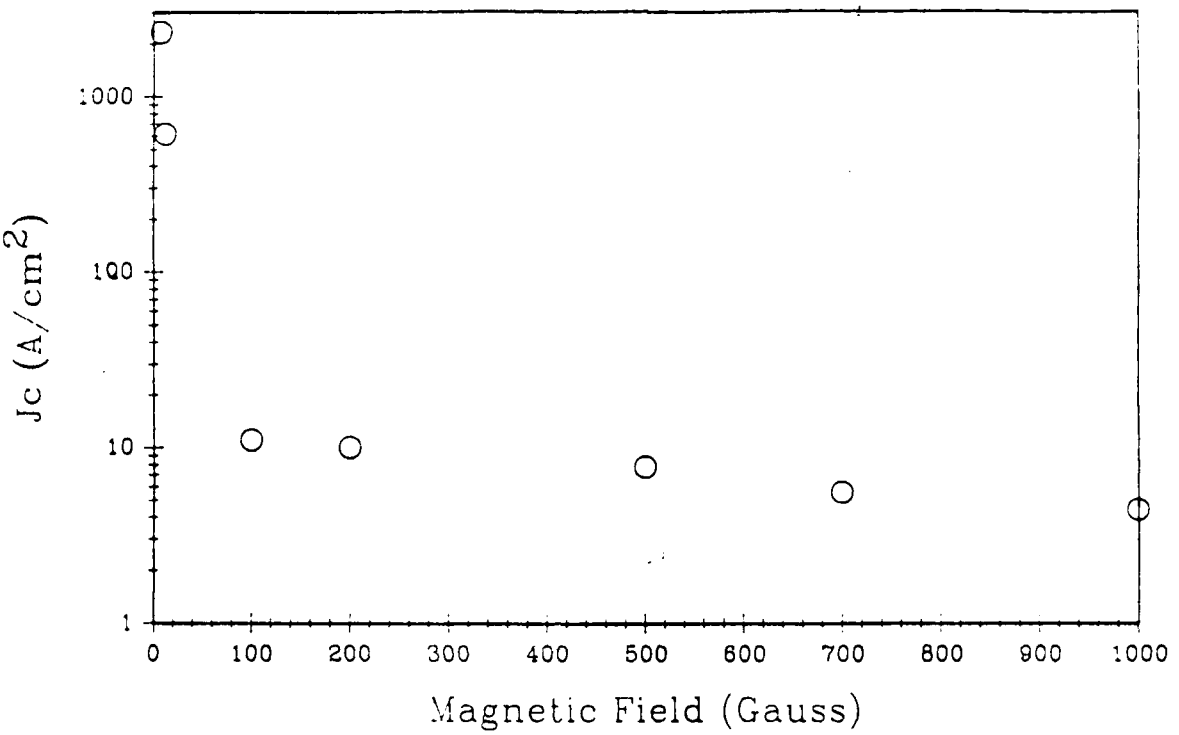


Figure 2.4.3 Critical Current Density vs. Magnetic Field at 77K for Bare Y-123 Filament

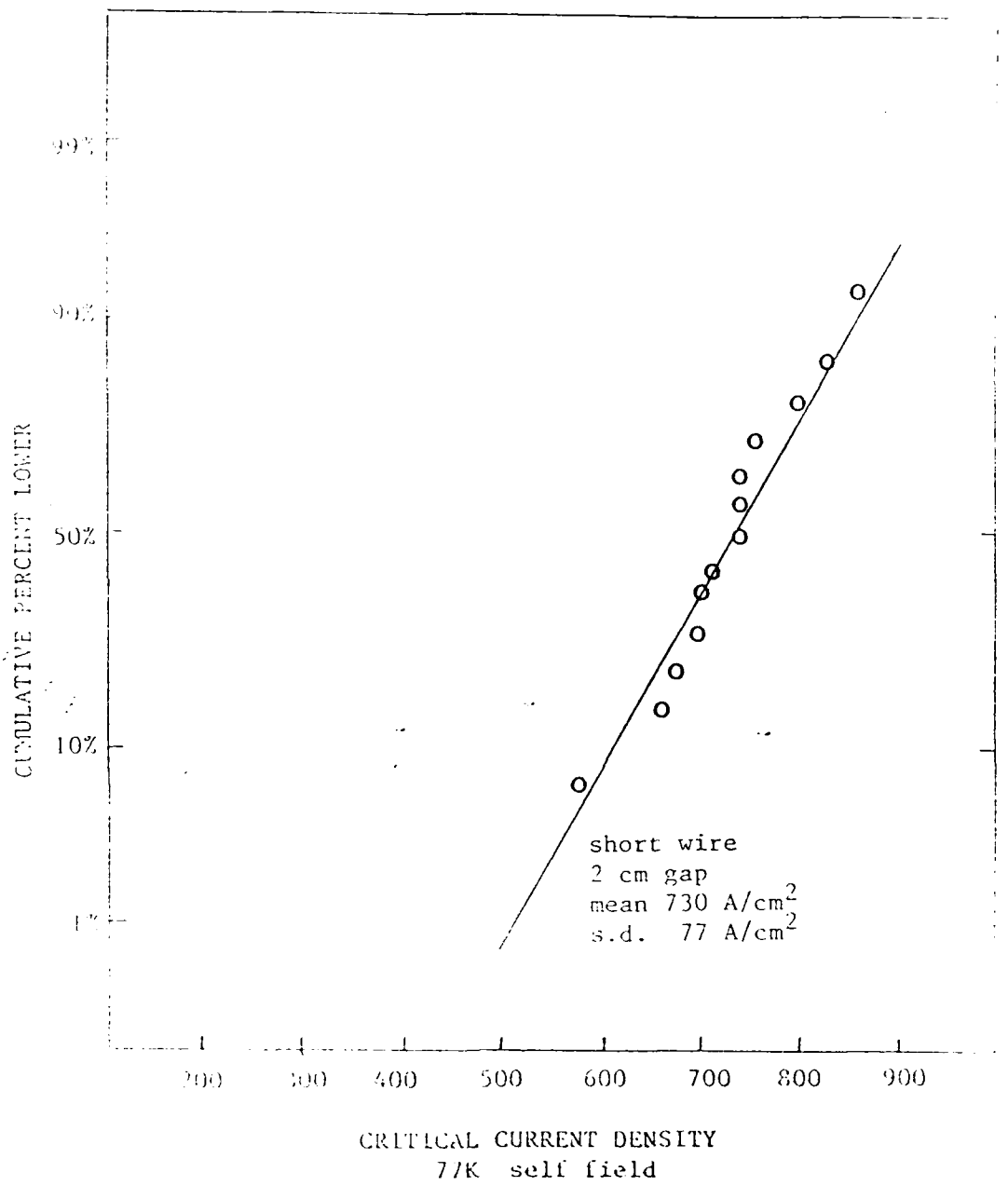


Figure 2.4.4 Distribution of $J_c$ Data for Short Wire Samples

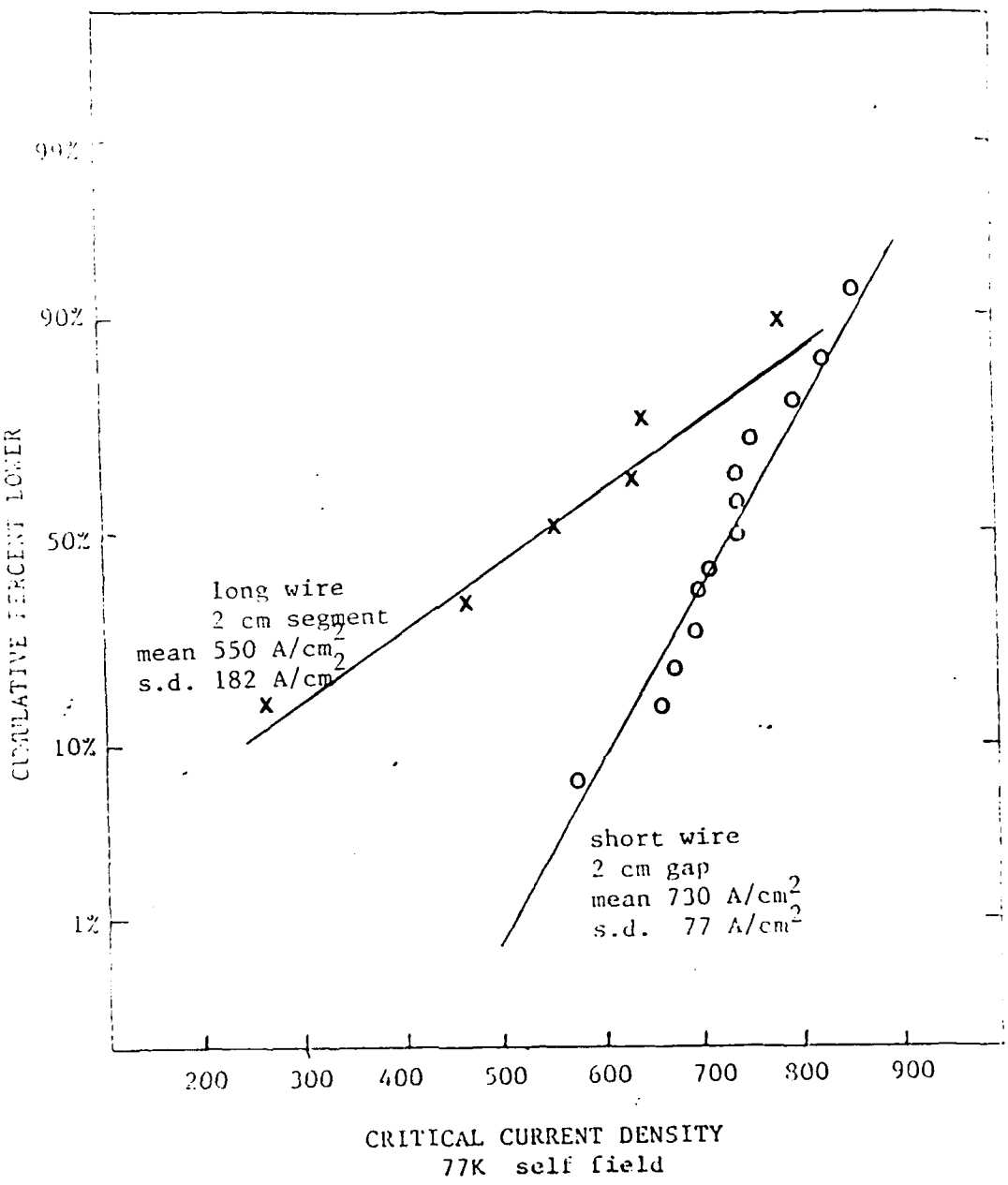


Figure 2.4.5 Distribution of $J_c$ Data for 2-cm Segments of Long Wires Compared with Short Wire Samples at 2-cm Gage Length

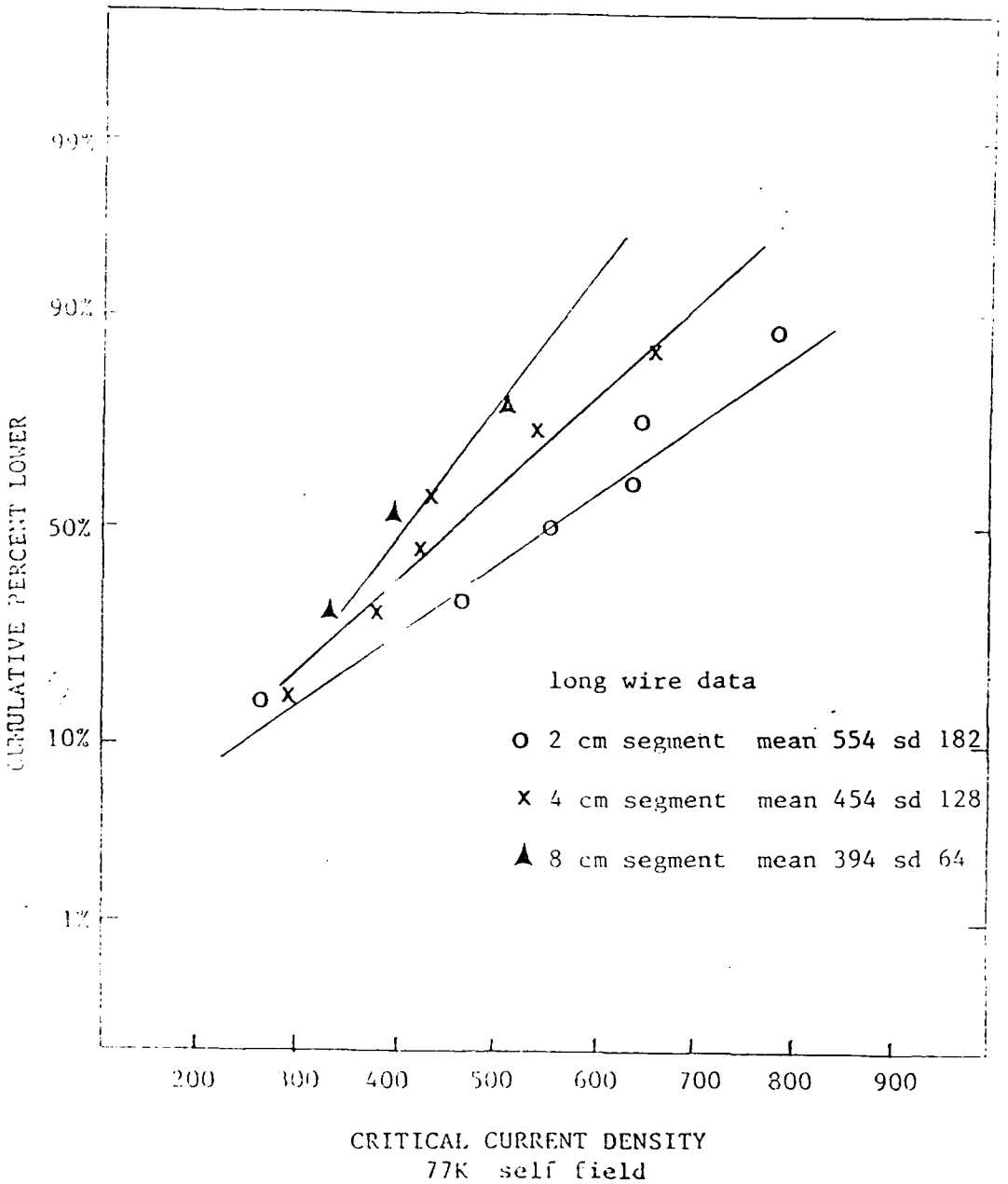


Figure 2.4.6 Distribution of $J_c$ Data for 2-cm Segments, 4- cm Segments, and 8-cm Segments of Long Wires

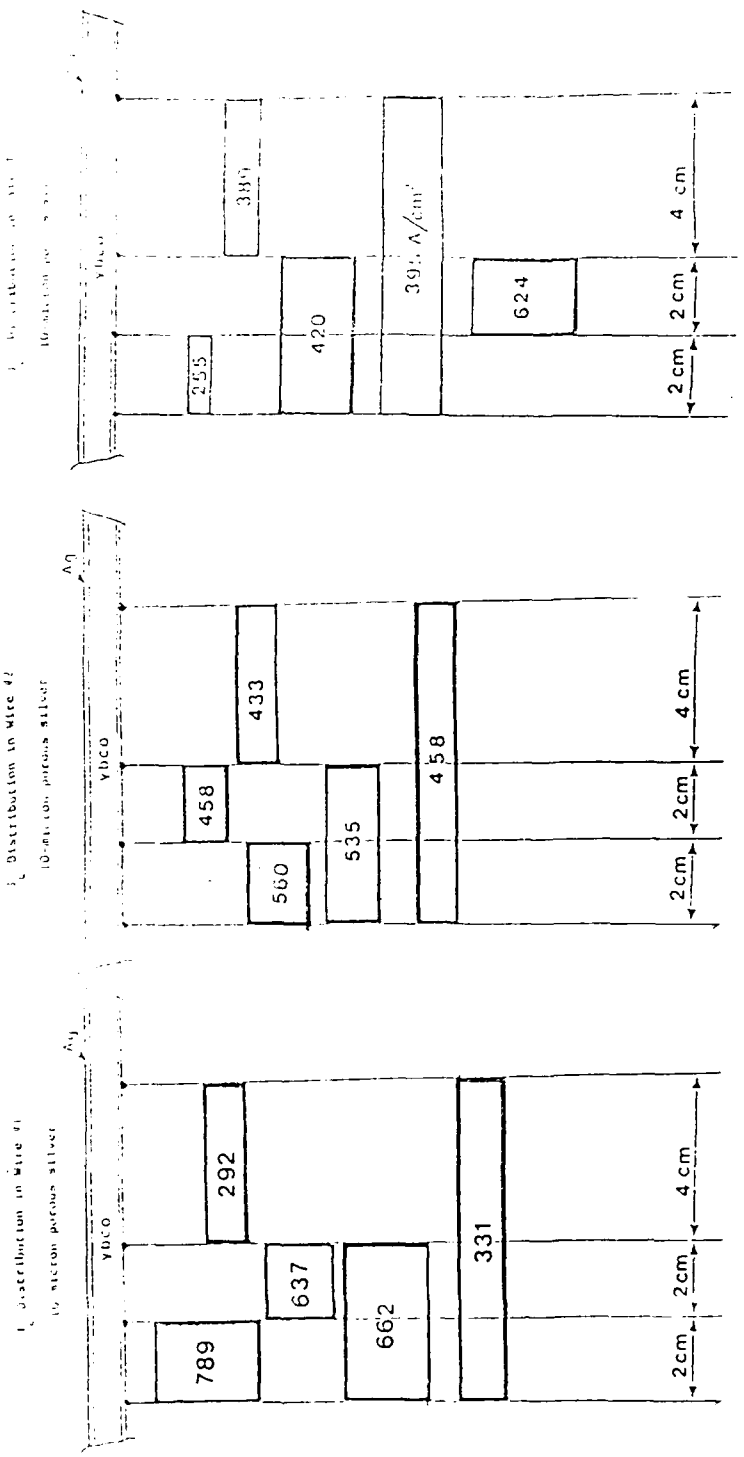


Figure 2.4.7 - Spacial Variations of $J_c$ Within Three Long Wires

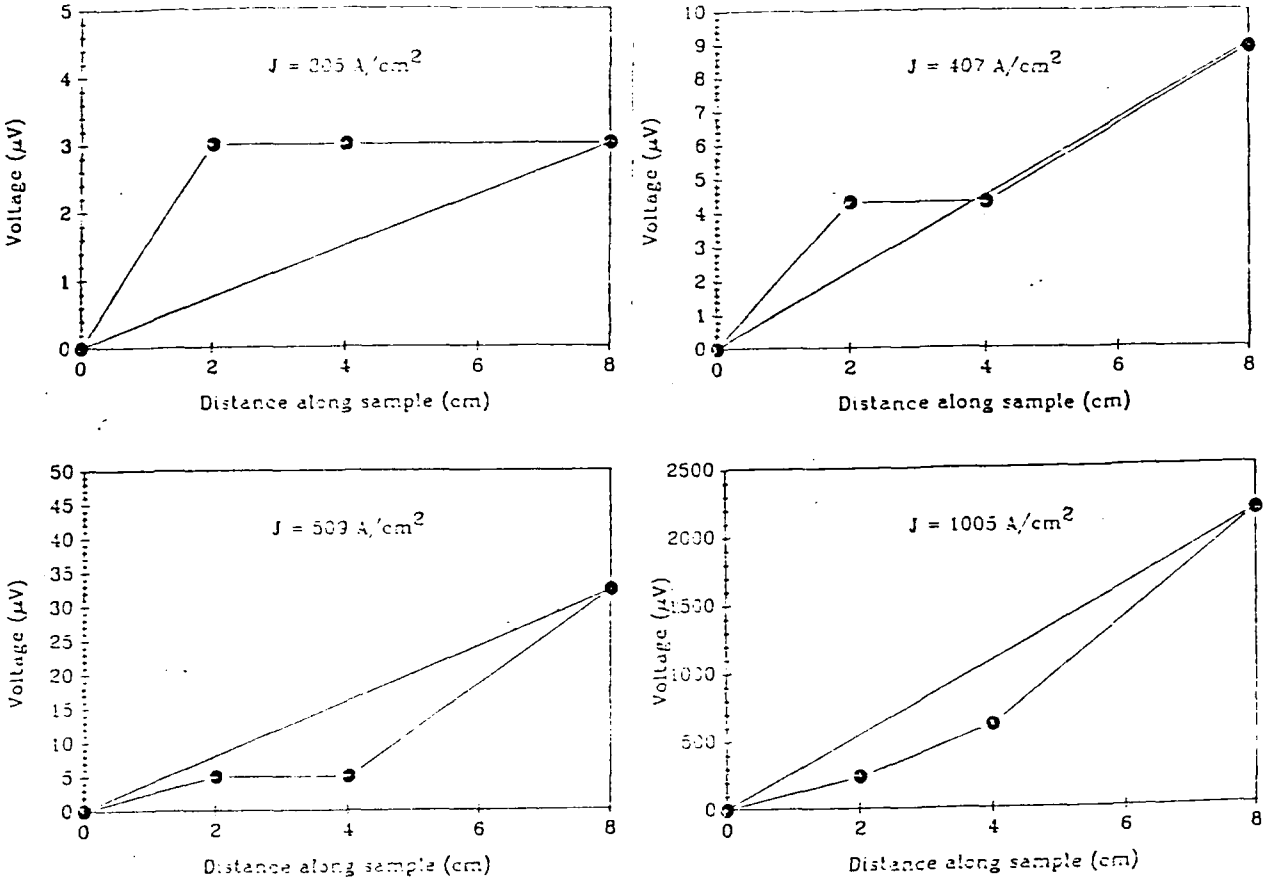


Figure 2.4.8 Voltage Measured at Each of the Four Taps in a Multiple Contact Long Wire at Current Densities of 305-,407-, 509- and 1005 A/cm²

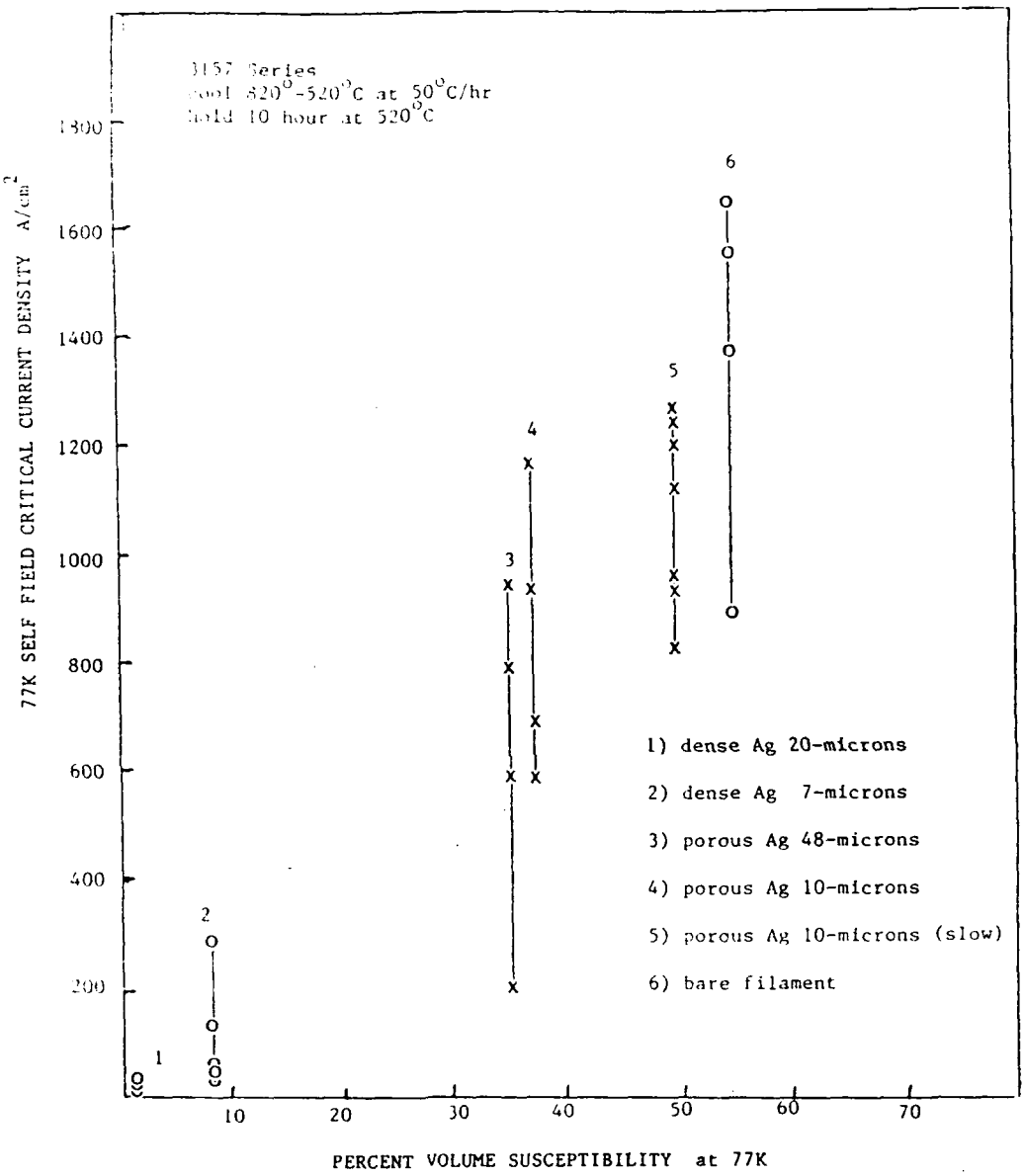


Figure 2.4.9 Transport Critical Current Density vs. Volume Susceptibility at 77K

## 2.5 Melt Processing of HTSC Wires

The third and most critical stage of Y-123 wire manufacture is the directional solidification post-process to create a high $J_c$ wire. This was not part of the original project plan, and only recently has the program been restructured to address this issue. Recognizing that melt texturing is the only demonstrated bulk method to make strong-linked Y-123, a major change was made in the contract late last year to focus research on methods to melt texture our Y-123 wire. Resources were reprogrammed from advanced HTSC motor development to materials development to fund new activities aimed at a manufacturing process for high critical current density Y-123 in the form of wire. This supports expanded activities in-house at CPSS and two new subcontracts at Arthur D. Little and at the HTSC Pilot Center at the Oak Ridge National Laboratory.

We have had very encouraging results with our in-house program, and have succeed in converting 125- to 250- micron bare sintered wire into high $J_c$ melt textured wire up to 50-cm long, using a continuous melt texturing process.

### 2.5.1 Melt Processing Activities at CPSS

At CPSS we have made melt textured YBCO fibers and pellets. The fibers are our ordinary sintered bare fibers, and are the prototypes for melt wire fabrication. This has been a recent, but intensive, activity. The work on melt texturing of pellets has been a longer, lower intensity effort, originally considered to be a convenient way to explore compositions and heat treatment schedules. The pellet work, however, now has high priority, since we will fabricate the magnet replicas for the "trapped flux" motor from melt textured

pellets.

2.5.1.1 Continuously melt textured wire

Melt textured fibers are made in a simple apparatus in which sintered fibers, up to 0.5 meters long, are slowly pulled through a small "microfurnace" with a 25 mm long hot zone. The microfurnace was fabricated with a simple winding of heater wire around a small diameter ceramic tube, using a variac as a power supply. For most experiments, the peak temperature in the microfurnace has been around 1100°C, with a temperature gradient around 150°C/cm at the peritectic. The fibers are pulled vertically through the microfurnace. So far we have employed only two transverse speeds: 4.2 mm/hr and 1.3 mm/hr. The best results have come from the 4.2 mm/hr speed, which corresponds to a cooling rate through the peritectic of around 65°C/hr. Fibers melt textured at 1.3 mm/hr have an almost perfect "bamboo" grain structure, which seems to be associated with inferior properties.

Our first generation microfurnace is not well controlled. There are some thermal excursions due to voltage fluctuations, air currents, and the motion of the fiber as it waves in the breeze. These will be corrected in the second generation microfurnaces which are now being designed.

Several of the melt textured wires were shown in Figure 1.1.3 (Section 1) to illustrate the length of the recent 250-micron and 125-micron diameter wires. Shorter samples of the wires were broken from the wires and given an oxygen anneal[9] and mounted for transport measurements. Figure 2.5.1 is a photograph of one of the first mounted samples. The electric field vs. current

---

[9]. Two schedules have been used. Schedule A: heat in oxygen to 670°C, hold 2 hours, cool at 25°C/hr to 375°C, hold 10 hours; and schedule B: heat in oxygen to 600°C, cool at 6°C/hr to 300°C. Preliminary data suggests that schedule B is superior.

density data in self field (80 G) and in a 1 tesla applied field ($\underline{J}$ normal to $\underline{B}$) appear in Figure 2.5.2. These data are limited by contact heating (as evidenced by vigorous boiling of nitrogen at the contacts), so represent a lower limit of the actual $J_c$. Better contacts are being developed.

We have characterized several melt textured wires in an attempt to relate microstructure to properties. One example is shown in Figure 2.5.3, which has the E vs. J characteristics for four regions of a single wire. This data was obtained from a 10-cm long wire which had been electroded with five sets of voltage taps. Sections "C" and "D" had a self field $J_c$ value of 11,770 A/cm$^2$ and 8,630 A/cm$^2$, respectively, while the adjacent sections "A" and "B" only had values of 940 A/cm$^2$ and 1450 A/cm$^2$, respectively.[10] The entire wire has been sectioned and polished to begin the study of microstructure vs. $J_c$. Complete results are not yet available, but "good" sections tend to have a microstructure similar to Figure 2.5.4A, with a small number of oriented grains running down the axis of the fiber. Examples of microstructures of "poor" sections appear in Figure 2.5.4B, showing poor orientation, or Figure 2.5.4C, showing an abrupt termination of a single crystalline segment of wire. We are aggressively investigating the processing-structure-properties relationships for these wires.

The AC susceptibility of a melt processed wire appears in Figure 2.5.5, showing a very sharp onset of the real susceptibility at 88K, dropping to 80% at 77K, with a peak in the imaginary susceptibility at 87K.

### 2.5.1.2 Melt Textured Pellets

---

[10]. One recent M-T wire had a 5-mm long segment with a $J_c$ which exceeded 15,000 A/cm$^2$ at 1 tesla.

We are working on melt texturing of pellets to get baseline data and more conveniently explore compositions and time-temperature profile. These pellets will also be used to fabricate "magnet replicas" for the trapped flux motor. Melt textured pellets have been prepared from a variety of feedstock, including stoichiometric Y-123 powders, mixed powders of Y-123 and Y-211, and mixtures of yttria, barium cuprate, and copper oxide. Some experiments were done on premelted materials similar to the Nippon Steel QMG process. Considerable effort was spent to find a convenient way to support pellets during the process to prevent loss of liquid, reaction, and slumping. Once an effective technique was found, we began an exploration of the temperature-time profile.

Our most complete data is for stoichiometric Y-123. We find the critical temperature range for recrystallization for this composition is 980-990°C. This is significantly below the peritectic temperature in air. At higher temperatures, between 990 and 1010, the recrystallization is much slower. The stoichiometric material always crystallizes to leave excess 211 and 011 (barium cuprate). The 211 resides as discrete particles trapped within the 123 grains and the 011 exists as thin precipitates parallel to the growth direction.

After melt texturing, the pellets are annealed in oxygen, typically at 450°C for up to 96 hours. Figure 2.5.7 shows the AC susceptibility of one of these samples, indicating a rather sharp onset at 91K, reaching a fraction of 80% at 80K. We have made a preliminary attempt to characterize flux trapping. Annealed pellets were cooled in an applied field up to one tesla. After being removed from the applied field, the pellets were magnetized by the trapped flux, and displayed both the levitation and suspension effects. The remnant magnetization was qualitatively assessed by measuring the flux density at the

surface with a Hall probe held on the pellet surface. One pellet, exposed to a 1 T applied field, had a trapped flux density of 300 G at the disc surface.[11] This is similar to the values reported by Weinstein et al. at the University of Houston.[12] More quantitative methods to measure trapped flux are being developed.

2.5.2 A. D. Little Laser Float Zone Program

This subcontract began in the last quarter. ADL has demonstrated that they can propagate a floating zone down a 1mm rod of CPS YBCO. More than 40 laser floating zone runs have been completed, to begin the exploration of composition and process variables. Figure 2.5.8 is a photograph of several 70% Y-123+ 30% Y-211 rods after the LFZ treatment. The microstructures of the LFZ rods have been characterized at CPSS. Microstructure varies dramatically with LFZ conditions. Figure 2.5.9 shows a polished section of the first LFZ rod, CPS 1, after a post anneal. In the as-grown condition, XRD showed that the rod consisted primarily of barium cuprate and 211, indicating that the cooling rate was too fast for the reverse peritectic reaction. The 211 phase was directionally solidified and located in a central core. In LFZ, the center of the rod is cooler, so the primary crystallizing phase (211 in this case) tends to segregate there. The barium cuprate was found in a thick surface layer. A post-anneal was done in an attempt to reform the Y-123 phase. After 32 hours at 850, XRD showed Y-123 as a major phase, with significant retained

---

[11]. If we assume that each trap corresponds to one flux quantum, the remnant magnetization should be proportional to the trap density: $B_{remnant} = \Phi N_{traps}$ so 300 G corresponds to 15 traps/square micron, or $1.5 \times 10^9$ traps/cm$^2$.

[12]. R. Weinstein, In-Gann Chen, J. Liu, D. Parks, V. Selvamanickam and K. Salama, Applied Physics Letters. 56 (15) 1475, 9 April 1990

barium cuprate and 211 phase. However, comparing the ordinary light with the crossed polarized images of Figure 2.5.9 shows that the Y-123 (bright contrast in crossed polars) grew as fine crystals between the barium cuprate and the directionally solidified 211 core. This points out the need to prevent gross segregation and to do the peritectic anneal more carefully.

We are exploring directional solidification in the primary crystallization field of Y-123. This would promote direct crystallization of Y-123, although at the primary Y-123 would be combined with a large amount of a eutectic of barium cuprate, CuO, and Y-123. The literature has poor agreement about the location of the Y-123 primary crystallization field, so we have underway an experiment to establish regions of Y-123 crystallization.

### 2.5.3 Oak Ridge National Laboratory Pilot Center Program

We have a program pending at the HTSC Pilot Center at Oak Ridge National Laboratory in the form of a funds-in cooperative program. Lynn Boatner's group in the Solid State Division at Oak Ridge National Laboratory will supply the resources of a complete crystal growth/solidification group. The program will involve a number of ORNL scientists, with Brian Sales and Brian Chakoumakos as the primary investigators. The major thrust is to identify Y-123 alloys with better solidification behavior, and outline the most favorable solidification conditions. They also will conduct directional solidification experiments on rods and filaments made at CPS Superconductor, using an arc image apparatus and a resistive apparatus. They will also help us develop "metal jacketed zone melting", an approach using silver alloy-clad wires. The ORNL group also will coordinate all advanced characterization work.

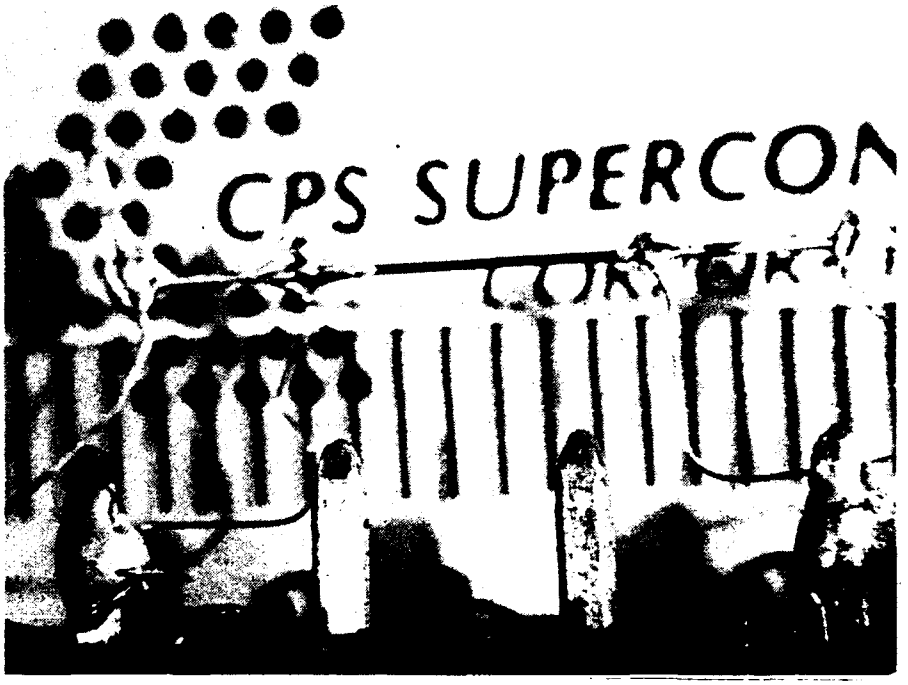


Figure 2.5.1 Continuously Melt Textured 250-Micron YBCO Wire Mounted for Electrical Testing

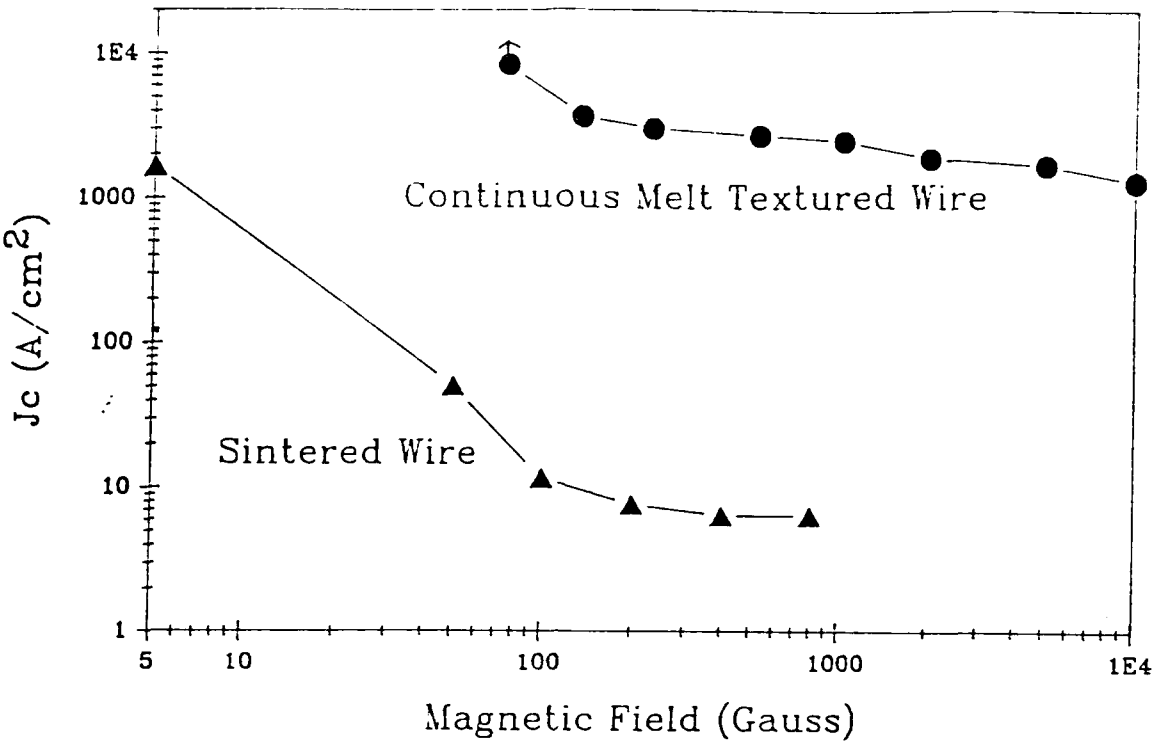


Figure 2.5.2 Critical Current Density at 77K vs. Magnetic Field for the 250-micron Diameter Melt Textured Wire Shown in Figure 2.5.1, Compared with Sintered Polycrystalline YBCO Wire

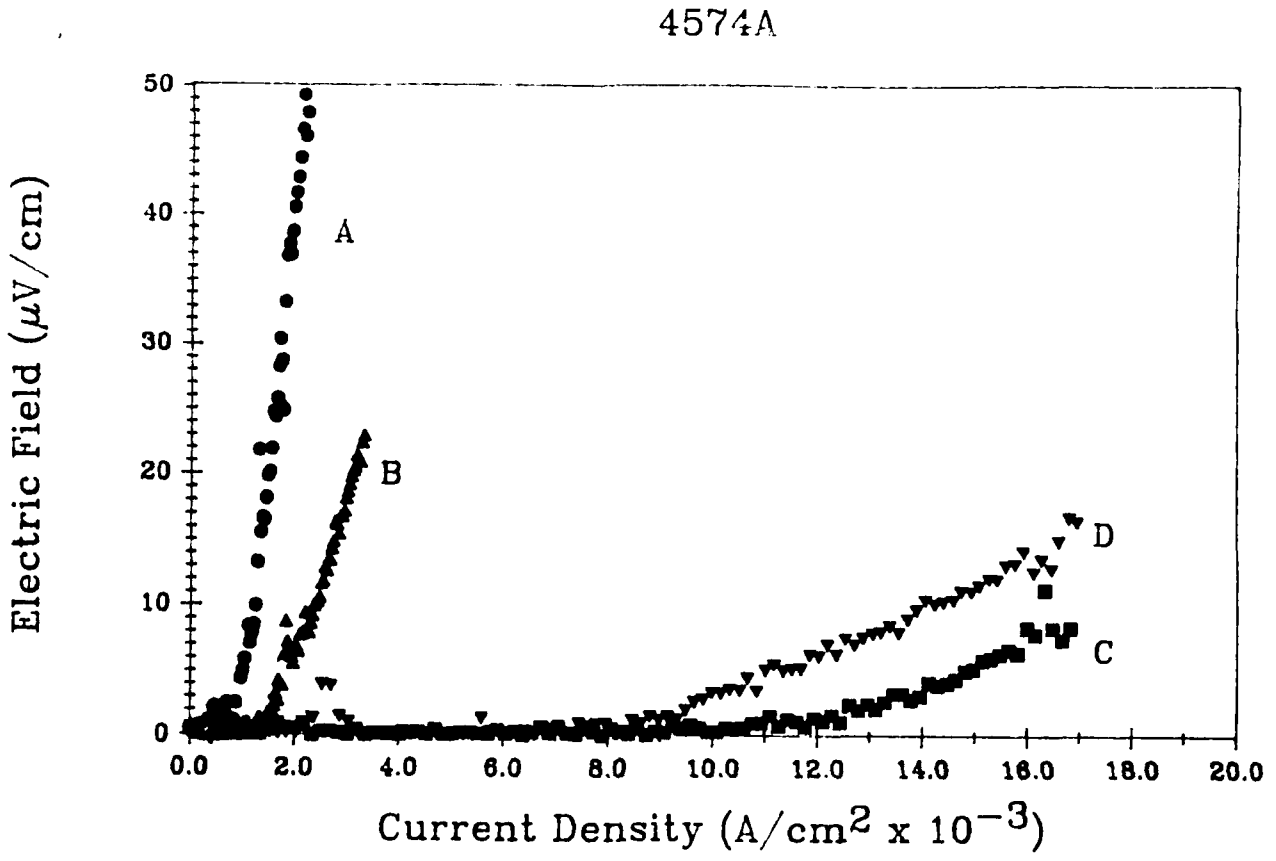


Figure 2.5.3 Electric Field vs. Current Density at 77K in Self Field for Four Adjacent Regions of a 10-cm Long Melt Textured YBCO Wire

Figure 2.5.4A Microstructure of a "Good" Region of a Melt Textured YBCO Wire, Showing Several Well Oriented Grains Crossed Polars 200X

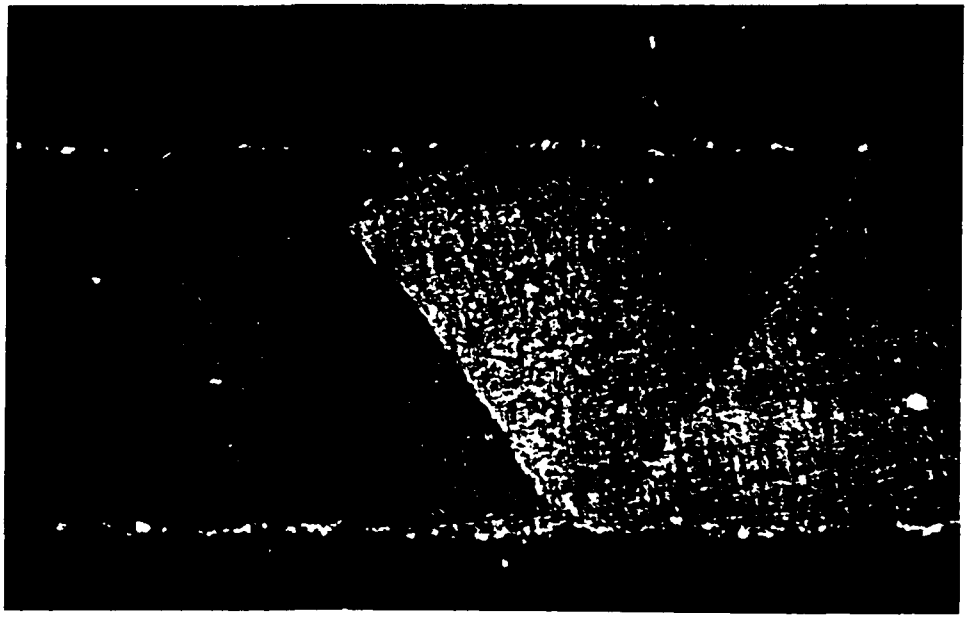

Figure 2.5.4B Microstructure of a "Poor" Region of a Melt Textured YBCO Wire, Showing Poor Orientation of Grains Crossed Polars 200X

Figure 2.5.4C Microstructure of a "Poor" Region of a Melt Textured YBCO Wire, Showing Abrupt Termination of Oriented Grains
Crossed Polars 200X

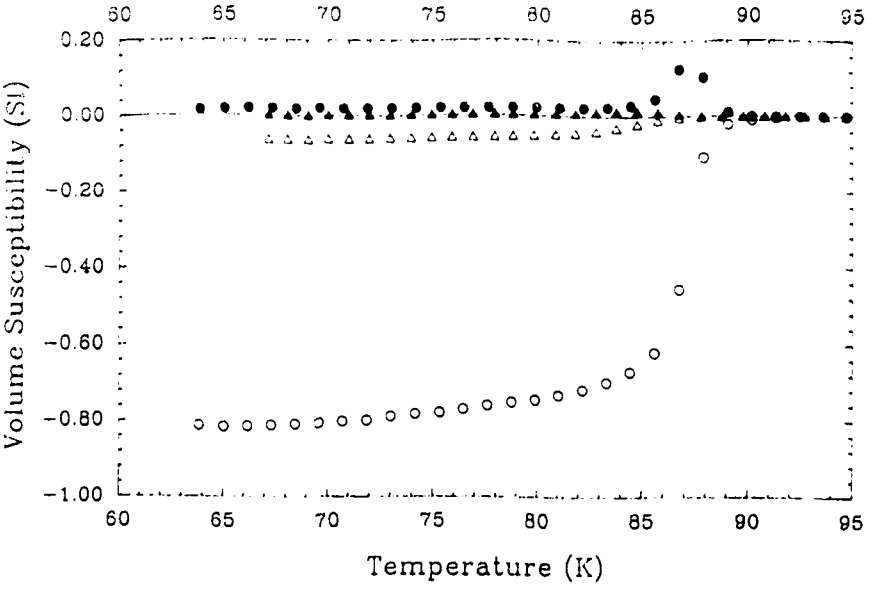


Figure 2.5.5 AC Susceptibility vs. Temperature for 250-Micron Melt Textured YBCO Wire

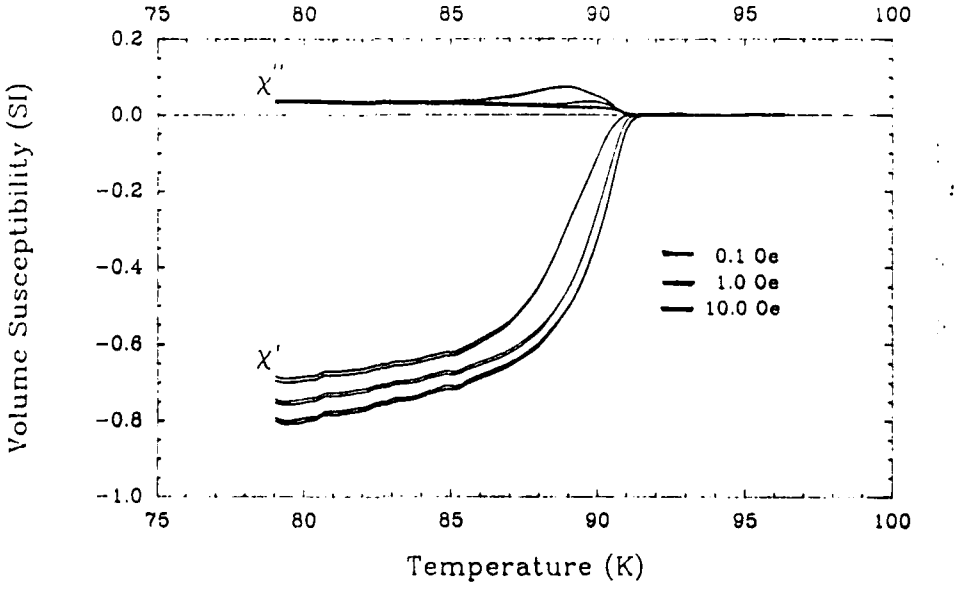


Figure 2.5.6 AC Susceptibility vs. Temperature for Melt Textured YBCO Pellet

CPS #24

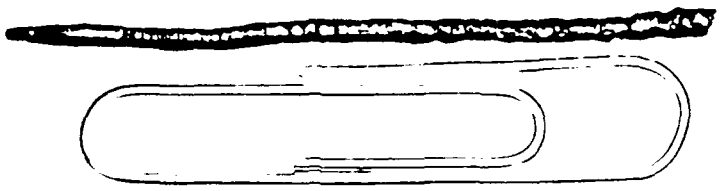

CPS #27

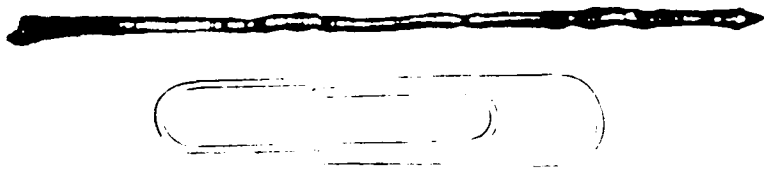

Figure 2.5.8 Laser Float Zone Processed Y-123+Y-211 Rods

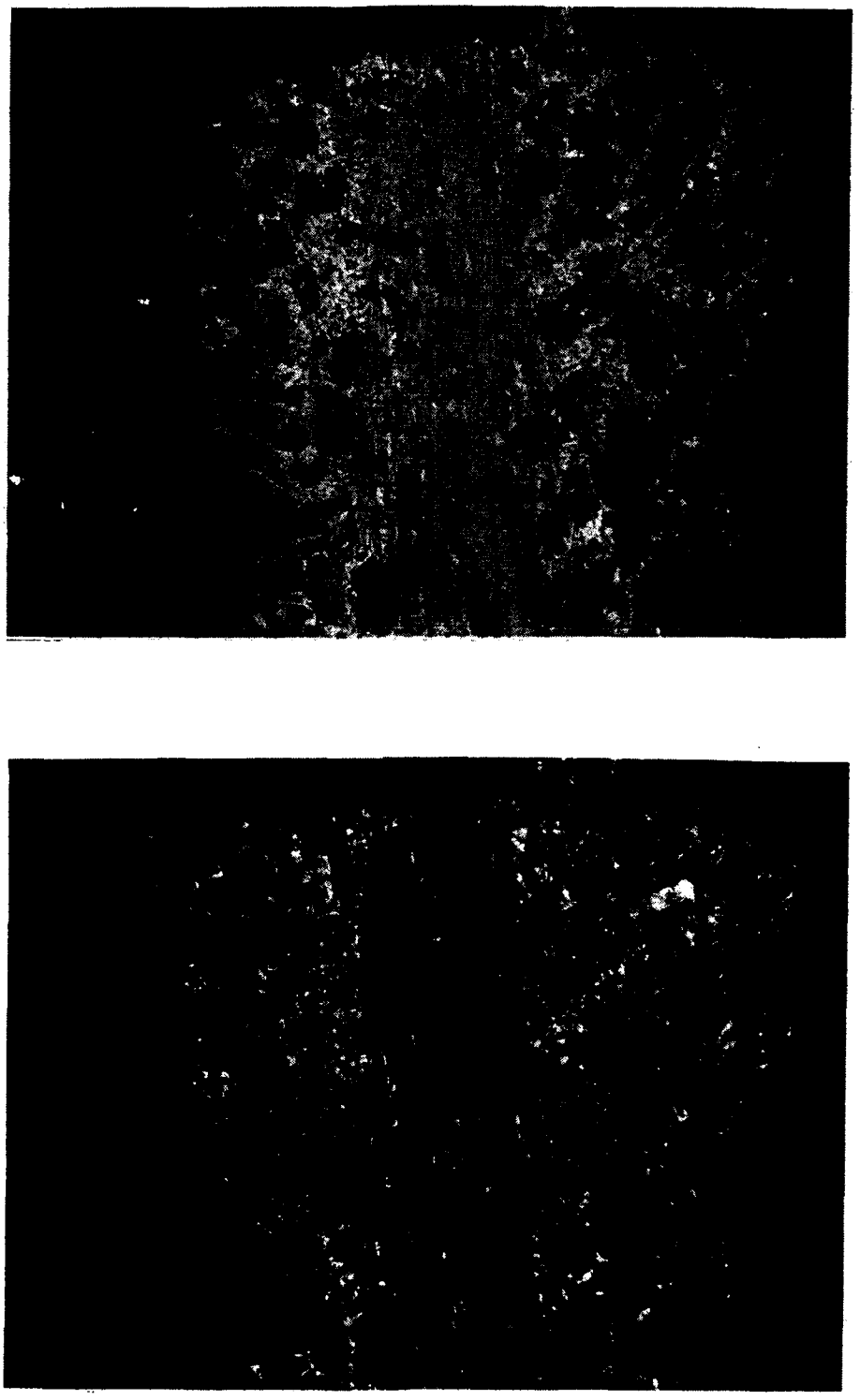

Figure 2.5.9 Polished Section of Laser Float Zone Processed Y-123 Rod CPS-1, after Post-Anneal at 850°C
Above: Ordinary Light Below: Crossed Polars 200X

2.5.4 Rapid Thermal Processing

In an informal collaborative project with David Ginley at Sandia National Laboratory we have explored rapid thermal processing of HTSC fibers. Rapid Thermal Processing (RTP) uses heat treatments of 2-4 sec. around 1000°C with a 3 min. cool down in oxygen to densify (burned out) green fiber or oxygenated presintered fibers. Rapid thermal processing rapidly densifies unsintered material, creating a microstructure characteristic of the fiber composition, RTP temperature and time. Green fibers are rapidly densified, displaying microstructures characterized by large grains with distinctive blocky or elongated morphology. Presintered Y-123 fibers do not undergo drastic microstructural change after RTP, but are rapidly oxygenated by the treatment.

Of particular interest is the fact that RTP annealed Y-123 is superconducting immediately after the RTP anneal, without requiring the 500°C oxygen anneal which is conventional for Y-123. Indeed, conventionally sintered Y-123 fibers, which are semiconducting in their as-sintered state, become superconducting after an RTP treatment, indicating that very rapid oxygenation occurs during RTP. Experiments with RTP of tetragonal Y-123 fibers made by pre-sintering in $N_2$ show that re-oxygenation by RTP in oxygen occurs during the 1-4 second isothermal hold at 1000°C, rather than during the 3-minute cooling ramp. Twinned orthorhombic Y-123 grows predominantly from grain boundaries, suggesting grain boundary diffusion of oxygen during the RTP anneal.

RTP has produced Y-123 material having, at best, similar properties to conventionally sintered Y-123 fibers, with $T_{c,r=0}$ of up to 90K and self field $J_c$ to 1200 A/cm$^2$. To date, all RTP specimens have been weak-linked. We are

continuing to explore the technique and, with NASA funding[13], are exploring RTP of continuous wires.1

Appended to this report is a paper in which we discuss in more detail the development of the microstructure when sintering occurs by RTP and characterize the phenomenon of rapid oxygenation by examining superconducting properties of pre-sintered Y-123 after RTP treatment.

[13] NASA-Lewis Research Center SBIR contract NAS 3-25876

SECTION 3

# HIGH TEMPERATURE SUPERCONDUCTOR MOTOR DESIGN AND FABRICATION

ALAN CRAPO AND JERRY LLOYD

EMERSON MOTOR COMPANY

MOHAMED HILAL

UNIVERSITY OF WISCONSIN

## 3.1 Introduction

The Emerson Motor Division (EMD) of Emerson Electric Company is responsible for the design, construction, and testing of HTSC motors, and related engineering activities in the application of superconducting wire to motor technology. In designing and building HTSC motors, there are two major objectives. The first is to develop a motor or motors which will test the HTSC wire produced by CPS Superconductor, to verify that the wire meets its performance goals in a real motor. The second major objective is to design and build a motor or motors that are optimized to take advantage of the characteristics of the newly developed HTSC wire.

While CPS is working toward short term and long term goals of wire performance, EMD is working on motor designs based on the near term and long term wire performance goals. The short term goal for superconducting wire that we were working to a year ago was a critical current density of 1000 $A/cm^2$ in a field of 100 Gauss or 0.01 Tesla. A homopolar DC motor that could

be used as a test bed motor to evaluate wire, was designed and built based on these near term wire goals. The details of the motor design, construction, and testing are discussed in the report.

The long term goal for wire is a critical current density of up to 100,000 A/cm$^2$ in a field of up to three Tesla. Motor designs based on higher performance wire are discussed, with particular details on brushless DC motors using flux trapping to maintain the rotor field.

## 3.2 Iron Core Homopolar Motor

Since the bulk HTSC wire of a year ago had critical current density values($J_c$) which were very sensitive to magnetic field, we designed the homopolar DC motor to have as much magnetic flux as possible in the air gap while keeping the flux density at the coil as low as possible. This is accomplished with a solid iron rotor. The flux carrying iron rotor is also the conductor of electrical current in the rotor. Figure 3.2.1 shows a side view cross section of the homopolar motor with various parts labeled. Figure 3.2.2 is an end view cross section showing the brush system layout.

The current collection system is made up of copper graphite brushes sliding on a steel slip ring. To improve the contact resistance, helical grooves have been added to the steel slip ring. Since the main purpose of this motor is to test and evaluate HTSC wire in a motor environment, we did not feel an expensive, elaborate current collection system with low losses was justified.

To reduce the complexity of testing the motor, the motor was designed to operate submerged in liquid nitrogen. The brushes and bearings would operate in liquid nitrogen, with the liquid nitrogen acting as the lubricant

# SUPERCONDUCTING HOMOPOLAR MOTOR DESIGN

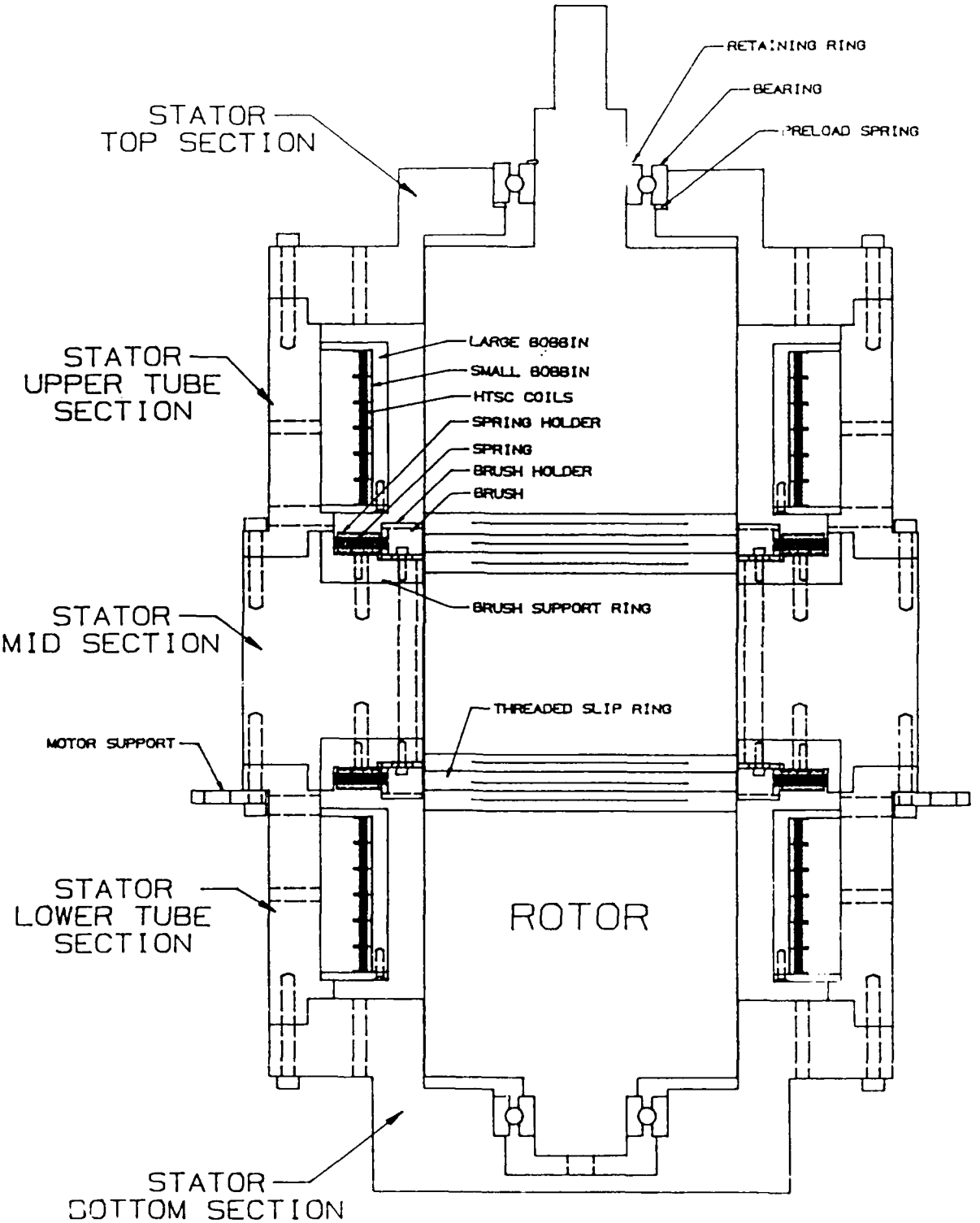


FIGURE 3.2.1

# MOTOR CROSS-SECTION (THROUGH BRUSH ASEMBLY)

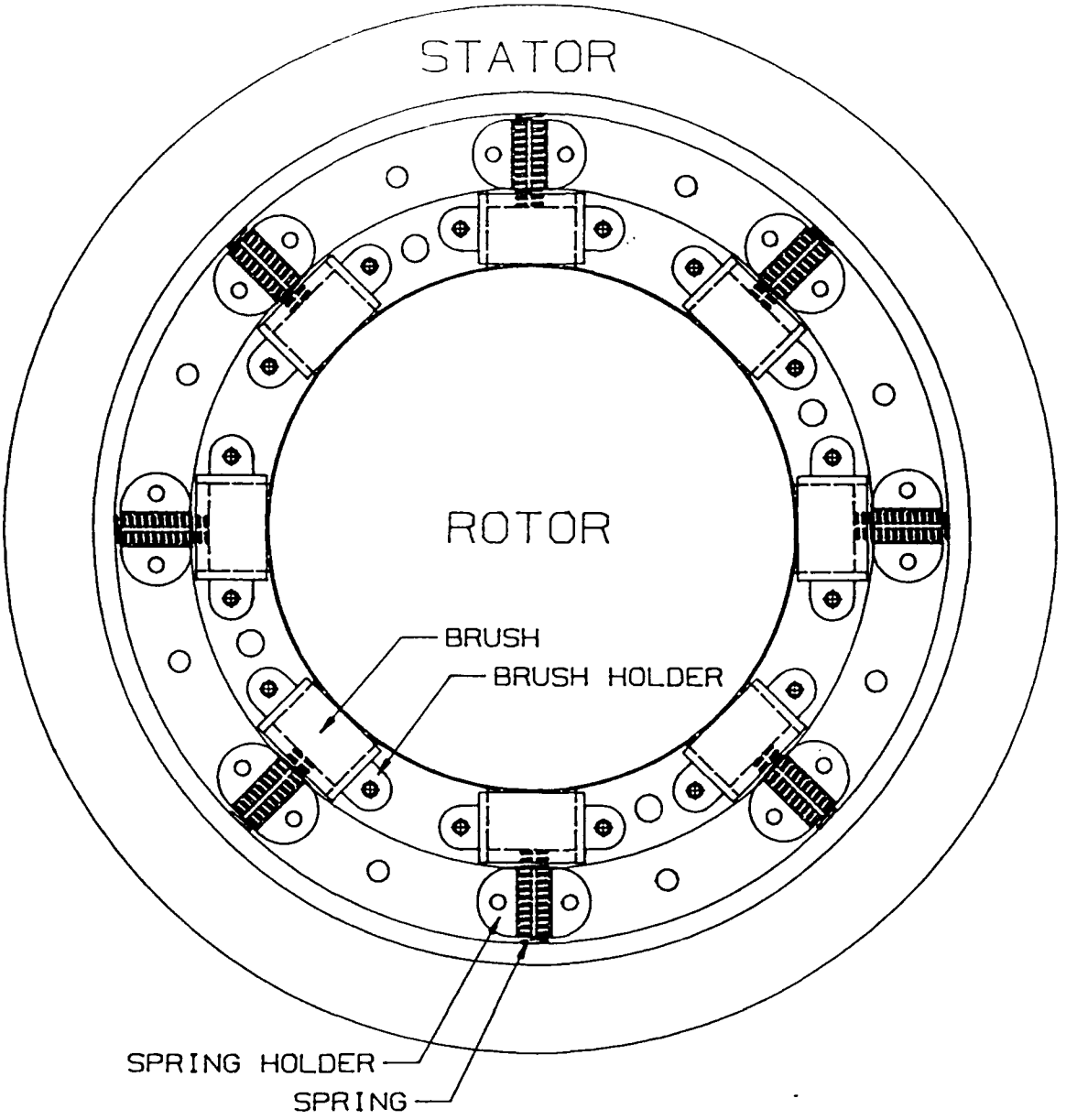


FIGURE 3.2.2

in the bearings. The bearing life of this test motor will not be as long as greased bearings at room temperature, but should be good for up to a hundred hours.

Since CPS has not yet produced enough HTSC wire to wind the homopolar motor, we built the first version using copper wire for the field winding. When the HTSC coils are available from CPS, we will swap coils and test the motor again. Using copper field windings first allows us to characterize the motor independent of the HTSC wire properties.

The copper wound motor has been built and we have begun testing the motor. The results are described in this report.

### 3.2.1 Brush Testing

Before finalizing the brush/slip ring design, we tested some small brushes and slip rings, with current at room temperature and submerged in liquid nitrogen. We tested the friction and the voltage drop.

#### 3.2.1.1 Brush Friction

A major component of loss in our homopolar motor will be brush friction. We made some friction measurements in order to calculate the frictional coefficient between the brush and slip ring material. This test was done with the threaded steel slip ring and both brush materials.

Using a DC motor as a prime mover, we rotated the slip ring assembly at 800 RPM. We measured the friction torque to be 2.74 oz-in for the 85% copper brush and 2.56 oz-in for the 65% copper brush. The brush area is 0.19375 inch$^2$. The drag force per brush is 2.19 ounce force for 85% copper and 2.05 ounce force for the 65% copper brush. With an applied spring force of

12.0 ounces on each brush, the pressure is 3.9 PSI, and the frictional coefficients are 0.18 and 0.17 for 85% and 65% copper brushes.

3.2.1.2 Voltage Drop tests

The best motor design from a magnetic point of view uses steel slip rings. We needed to make sure the steel slip ring would work as well as copper and brass. We tested two brush grades on four slip ring surfaces to determine the best combination for the motor. The two brush grades tested were 65% copper, and 85% copper mixed with graphite. We tested these brushes on slip rings made copper, brass, smooth steel, and steel with threads. These tests were done both at room temperature and in liquid nitrogen at a speed of about 1900 RPM on a 0.625 inch radius. The brush pressure was 3.9 PSI at room temperature in each case. The voltage drop across two brushes is series versus current density was recorded for each condition.

We had difficulty with the copper and brass slip rings at high current densities when submerged in liquid nitrogen in that there was some arcing and damage to the slip ring and brush. We did not attempt high current densities in room temperature air because of fear of overheating. We assumed that there would not be an overheating problem in liquid nitrogen.

The smooth steel slip ring did not have arcing problems but we found that as the brushes ran with current for very long (10-15 minutes), a high resistance film built up. The longer the brushes ran with current, the greater the resistance buildup. The data taken for the smooth steel slip ring was taken before much film buildup occurred. None of these smooth slip rings was acceptable.

We then found out that the correct way to use steel slip rings and not get the film was to put threads on the steel surface. The helical threads give a continuously changing edge between the copper and the steel. The threaded steel slip ring had no significant arcing, and no significant film buildup. The voltage drop characteristics were also pretty good. We used 16 threads per inch.

The following table lists the results of the tests:

**VOLTAGE DROPS**

| Brush %Cu | Slip Ring | Environment | Brush current density ($A/in^2$) 5.2 | 25.8 | 103 | 207 | 361 |
|---|---|---|---|---|---|---|---|
| 65 | Copper | Room Air | .055 | .21 | .43 | | |
| 65 | Copper | Liquid Nitrogen | .09 | .16 | .32 | .42 | .49 |
| 65 | Brass | Liquid Nitrogen | .29 | .43 | .73 | .89 | 1.05 |
| 65 | Smooth Steel | Liquid Nitrogen | .63 | .75 | .90 | 1.02 | 1.10 |
| 65 | Threaded Steel | Room Air | .045 | .18 | .46 | | |
| 65 | Threaded Steel | Liquid Nitrogen | .46 | .49 | .55 | .62 | .65 |
| 85 | Copper | Room Air | .015 | .07 | .23 | | |
| 85 | Copper | Liquid Nitrogen | .08 | .21 | .35 | .41 | .50 |
| 85 | Brass | Room Air | .018 | .057 | .18 | | |
| 85 | Brass | Liquid Nitrogen | | | .29 | .46 | .60 |
| 85 | Smooth Steel | Liquid Nitrogen | .18 | .26 | .34 | .40 | .48 |
| 85 | Threaded Steel | Room Air | .006 | .027 | .10 | | |
| 85 | Threaded Steel | Liquid Nitrogen | .065 | .15 | .26 | .33 | .39 |

The data on the above table is shown graphically in figures 3.2.3 through 3.2.10. For each set of data points, a best statistical fit is

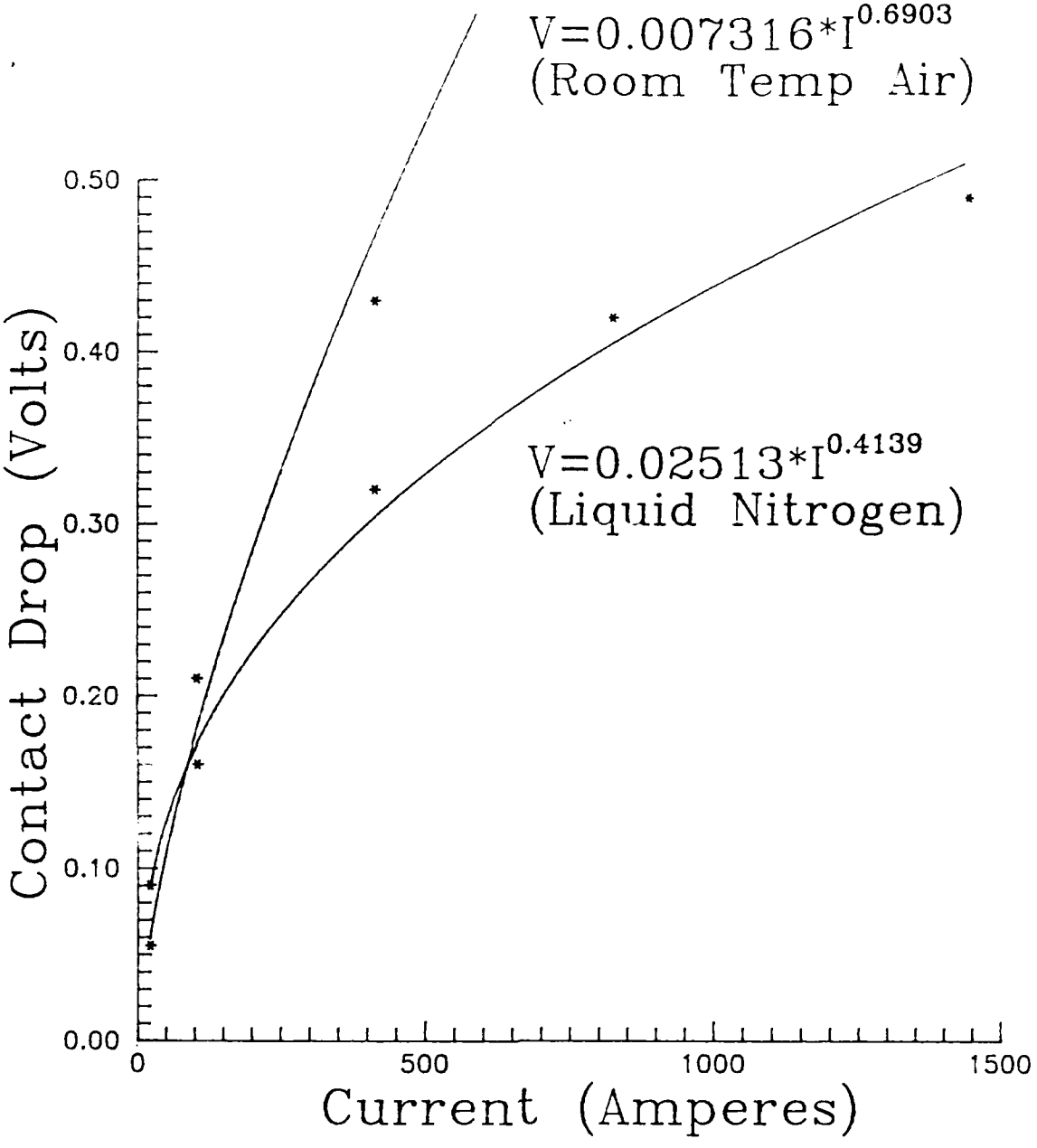


Figure 3.2.3
65% Copper Brush
Copper Slip Ring

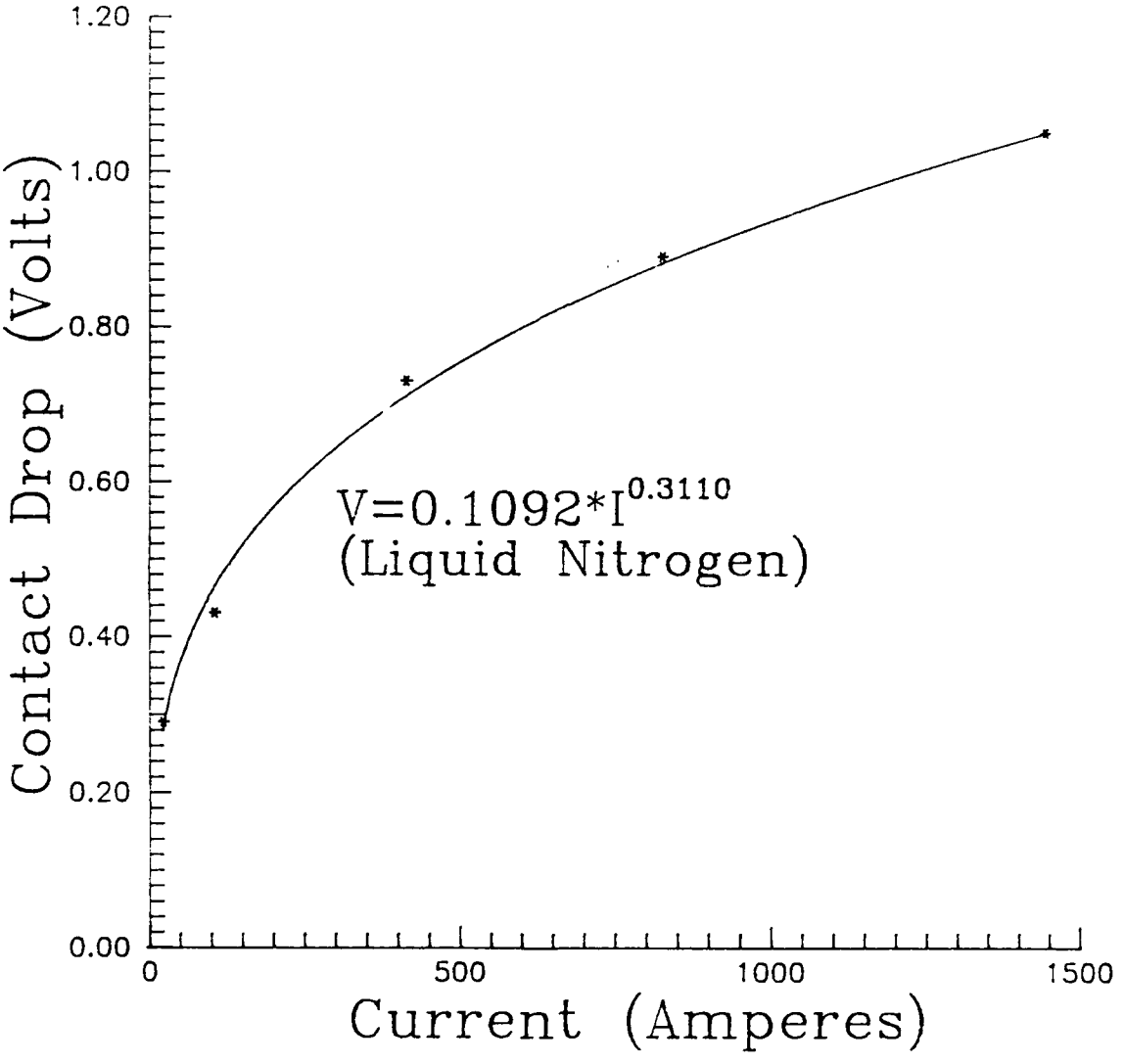


Figure 3.2.4
65% Copper Brush
Brass Slip Ring

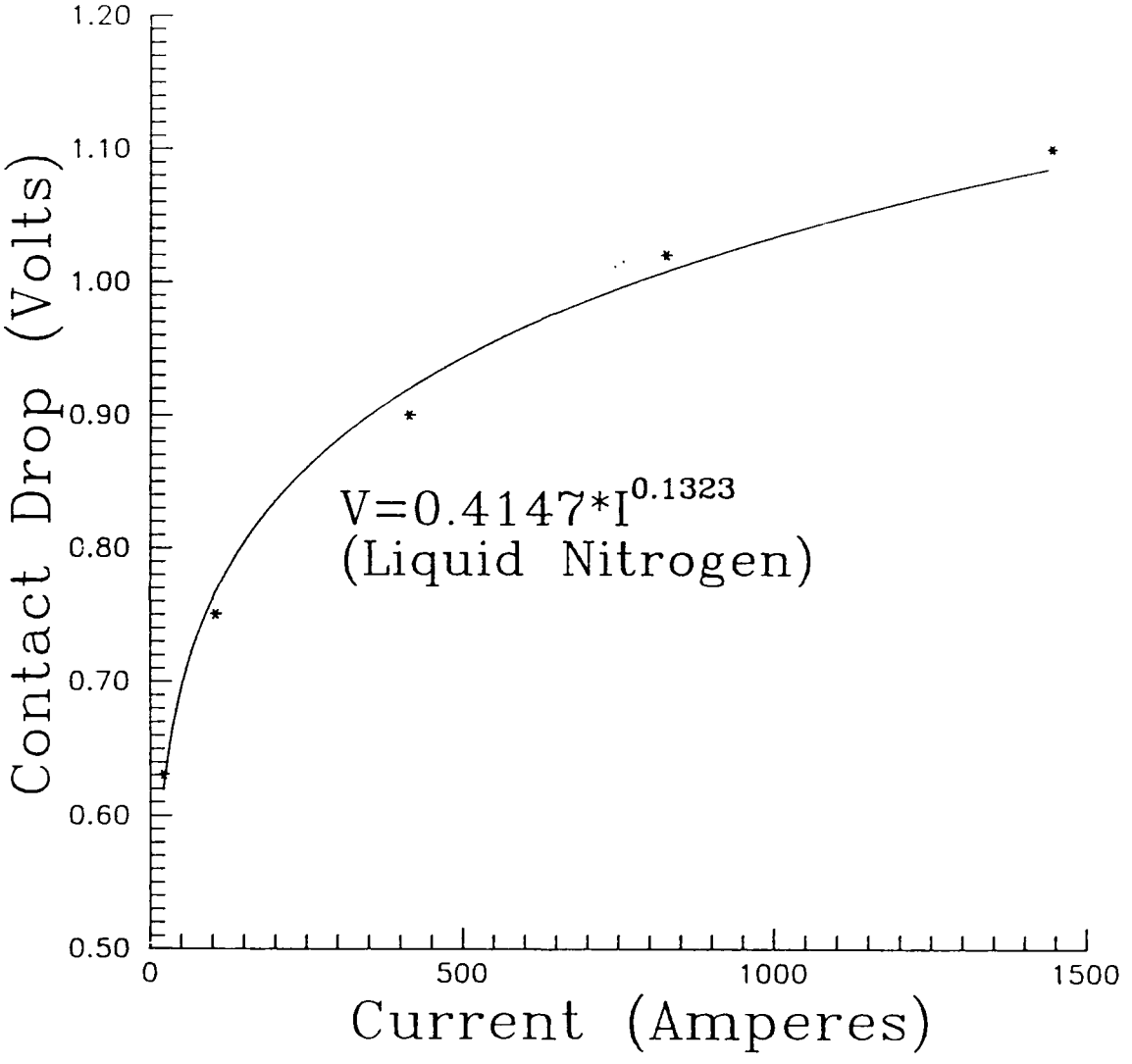


Figure 3.2.5
65% Copper Brush
Smooth Steel Slip Ring

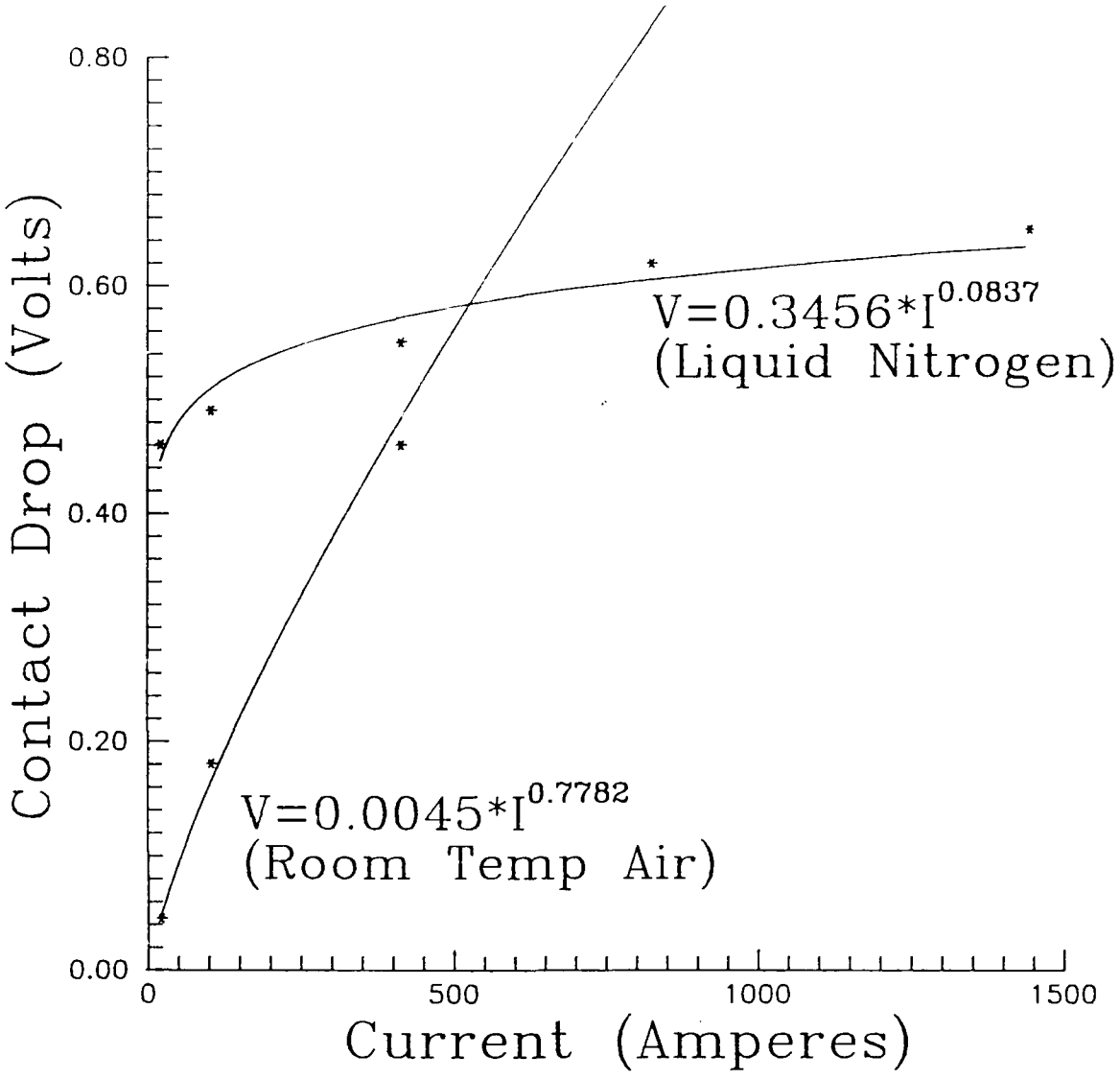


Figure 3.2.6
65% Copper Brush
Steel Slip Ring
(16 Treads per inch)

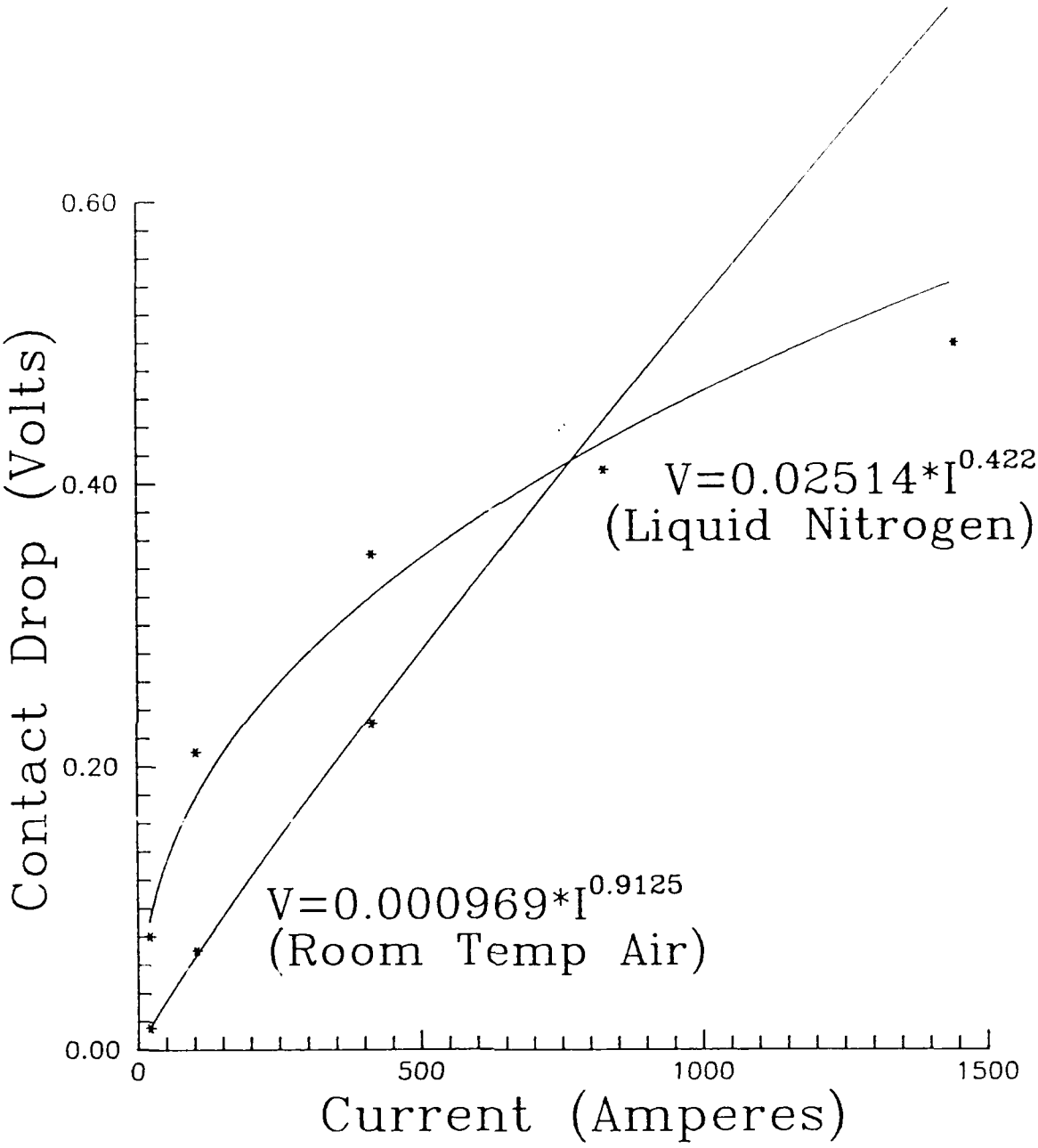


Figure 3.2.7
85% Copper Brush
Copper Slip Ring

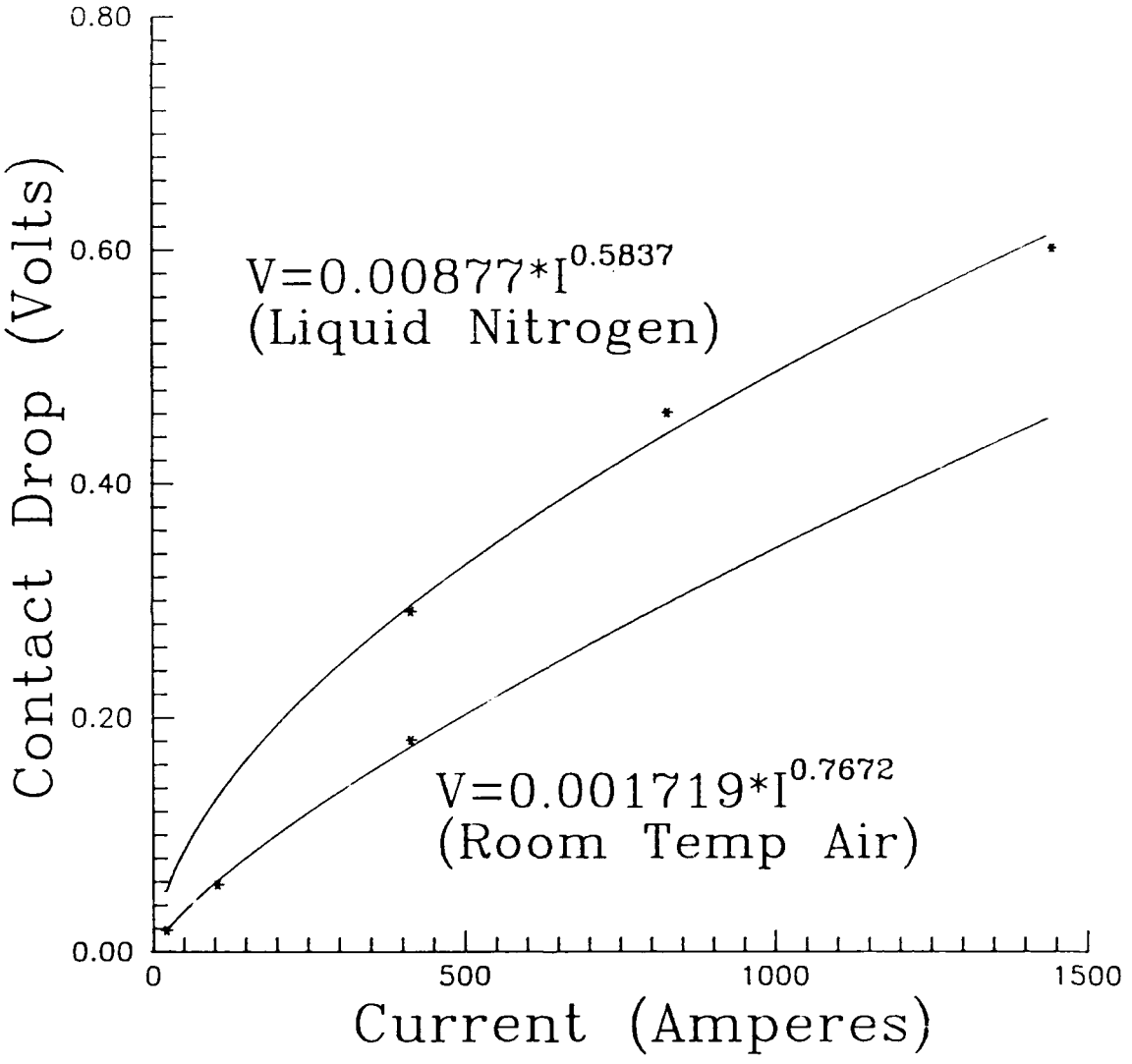


Figure 3.2.8
85% Copper Brush
Brass Slip Ring

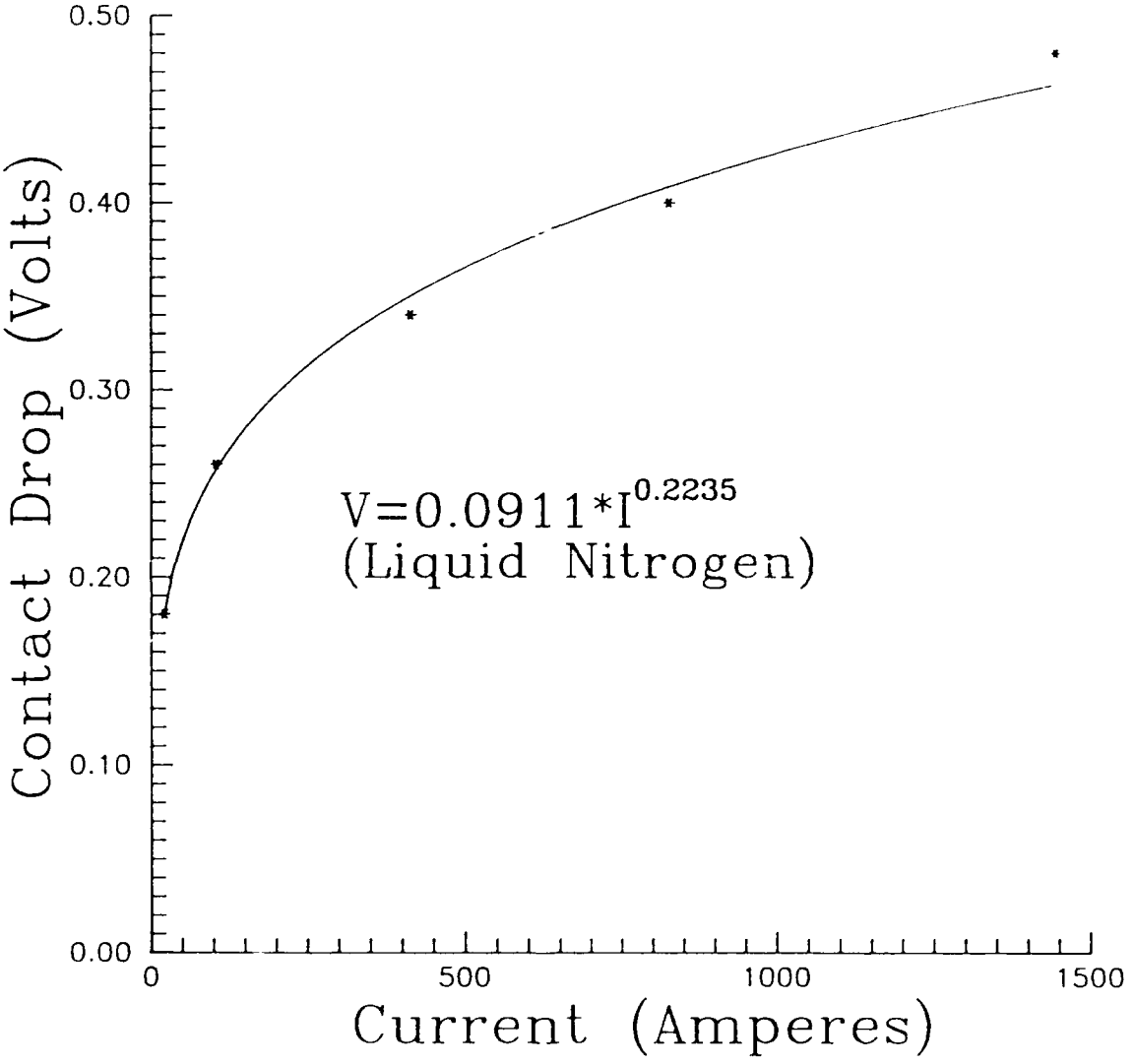


Figure 3.2.9
85% Copper Brush
Smooth Steel Slip Ring

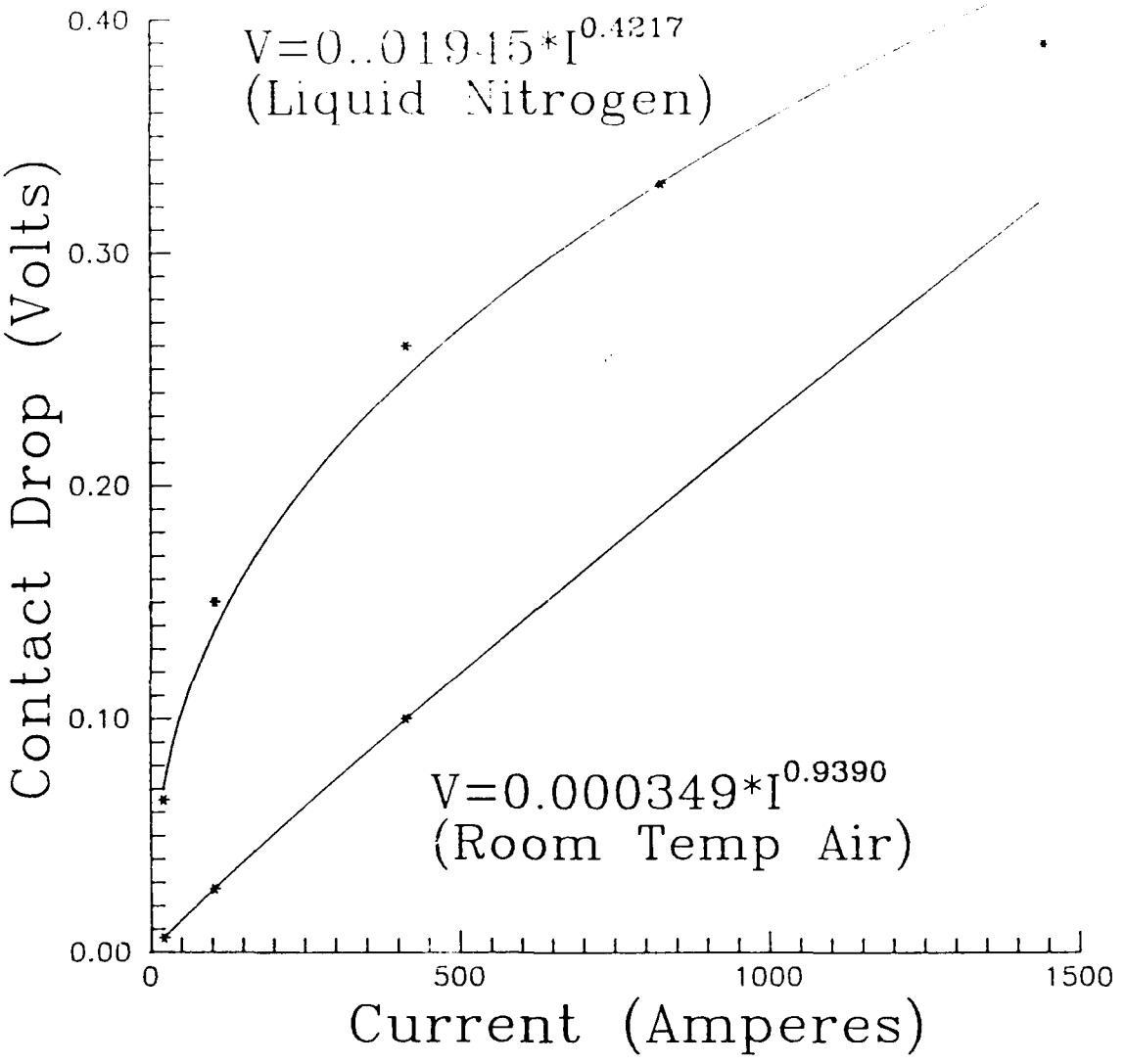


Figure 3.2.10
85% Copper Brush
Steel Slip Ring
(16 Treads per inch)

calculated based on a power fit of the form $V = A*I^B$ where A and B are constants. The film buildup on the steel slip rings is probably a factor in the low exponent in those cases. There may be some film or other effect caused by the liquid nitrogen. It's not clear if the fluid dynamics or the temperature is the main reason for the difference in shapes of the curves. The intent of this program is not to do a thorough in depth study of brushes and slip rings, but to find a system that will work to test wire.

### 3.2.2 Homopolar Motor Performance Calculations

#### 3.2.2.1 Original Designed Performance

Our coil design is based on our wire performance goal of 1000 Amperes/cm$^2$ in a field of 100 Gauss or 0.01 Tesla. This corresponds to 0.125 Amperes in a 0.005 inch diameter wire. 4600 turns on both coils gives us 575 Ampere turns per field coil.

In general, torque in a drum type homopolar DC motor can be expressed as:

Torque = Flux Density(B) X Current(I) · (Length of conductor path in B field) · (Radius)

or

Torque = B X I · l · r.

But B and I have non uniform distributions, and l and r vary. Finite element modeling was used to calculate B, I, l, and r throughout the active volume of the motor and calculate the torque. Figure 3.2.11 is a flux plot showing the distribution of B, with 575 Ampere turns per field coil, as a function of r (radial position) and z (axial position). Flux, current, and torque

STEEL CORE HOMOPOLAR
MOTOR FLUX PLOT

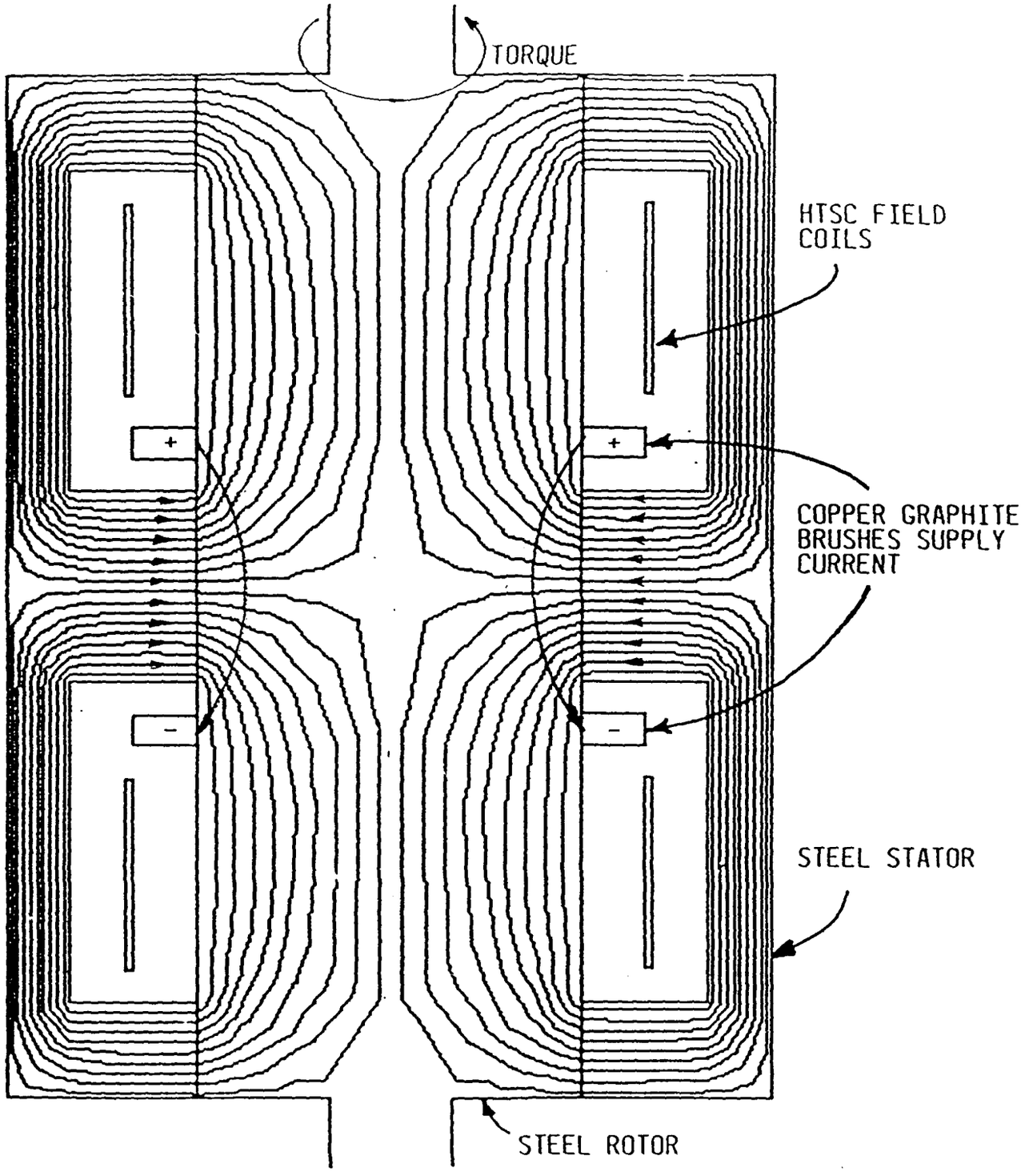


FIGURE 3.2.11

directions are identified. Figure 3.2.12 is a current contour map showing the current distribution as a function of r and z. The torque produced in each element was summed to give the entire motor torque:

Torque = 3.837 Nm with 1000 Amperes of current.

This is 95% of the torque calculated if we assume all of the current stays on surface of the rotor.

To calculate the actual shaft torque, the friction torque needs to be subtracted from the electrical torque. Friction torque comes mostly from the brushes and varies linearly with brush pressure. The input voltage required is the back EMF plus the voltage drops across the brushes. We can neglect other electrical losses for our first order calculations. The back Emf varies with speed and the flux of the motor. The voltage drops in the brush for a given brush and slip ring material vary with current in a nonlinear power relationship shown previously, and brush pressure. Brush textbooks show the voltage drop to vary with the brush pressure to about 0.6 power. The first calculations assume the field coils have the designed 575 Ampere turns on each coil, and there is no friction. In the actual motor, there will be friction, and we will not be able to get full design current in the coils due to the limitation of $J_c$ in the HTSC wire. The following equations which describe the motor performance include the field level as a percentage of the original design.

Electrical torque = 3.837Nm x (percent field/100)

Friction Torque = 0.488Nm x (Brush pressure in psi)

Shaft torque = Electrical torque - Friction torque

Mechanical power = Torque x Speed(radians per second)

Back EMF Voltage = 0.000402 x speed(RPM) x (percent field/100)

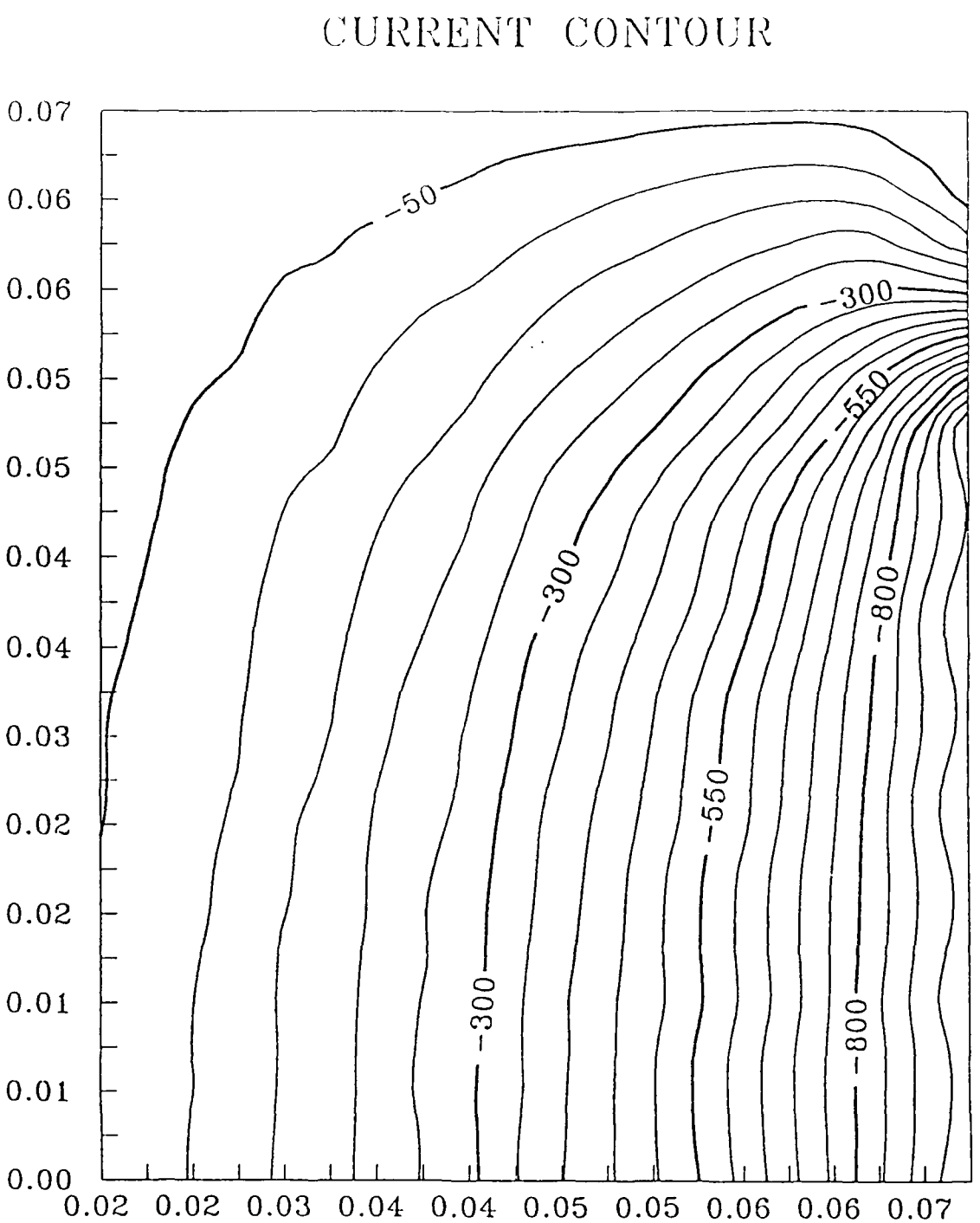
CURRENT CONTOUR
0.07
0.06
0.06
0.05
0.05
0.04
0.04
0.03
0.02
0.02
0.01
0.01
0.00
0.02 0.02 0.03 0.04 0.04 0.05 0.05 0.06 0.06 0.07
-50
-300
-550
-300
-800
-550
-300
-800

FIGURE 3.2.12

Voltage drop in Brushes =

$$0.01945 \times \text{Current}^{0.4217} \times (3.9 \times \text{Brush pressure in psi})^{0.6}$$

Input voltage = Voltage drop + Back EMF

Electrical power = Voltage x Current.

Losses = Friction power + Brush losses

Figure 3.2.13 shows the results of these performance equations plotted against brush pressure for the field at the original design level of 575 Ampere turns per coil. The losses are at their minimum value between 1.5 and 2.0 psi brush pressure. The output power with 1.5 psi brush pressure is calculated to be 976 Watts.

3.2.2.2 Effects of $J_c$ Reduced by Magnetic Field.

As previously mentioned our coil design is based on our wire performance goal of 1000 Amperes/cm$^2$ in a field of 100 Gauss or 0.01 Tesla. Wire built to date still does not reach this performance level. The present wire samples can carry 2600 Amperes/cm$^2$ in a zero Gauss field, but $J_c$ is greatly reduced in the presence of a magnetic field. Figure 3.2.14 shows how $J_c$ decreases as the field increases, based on uniform current distribution in the coil. The other two lines show the peak field produced at the coil as a function of the current in the coil for a 4600 turn and for a 9200 turn design. The line for 4600 turns intersects the wire line at a field of 25 Gauss and a $J_c$ of 250 Amperes/cm$^2$. This means the motor would operate at a maximum of 25% of the designed field level. This can be improved by increasing the turns on the coil. The 9200 turn (doubled) design would operate at about 35% of the designed field level with a $J_c$ of about 175

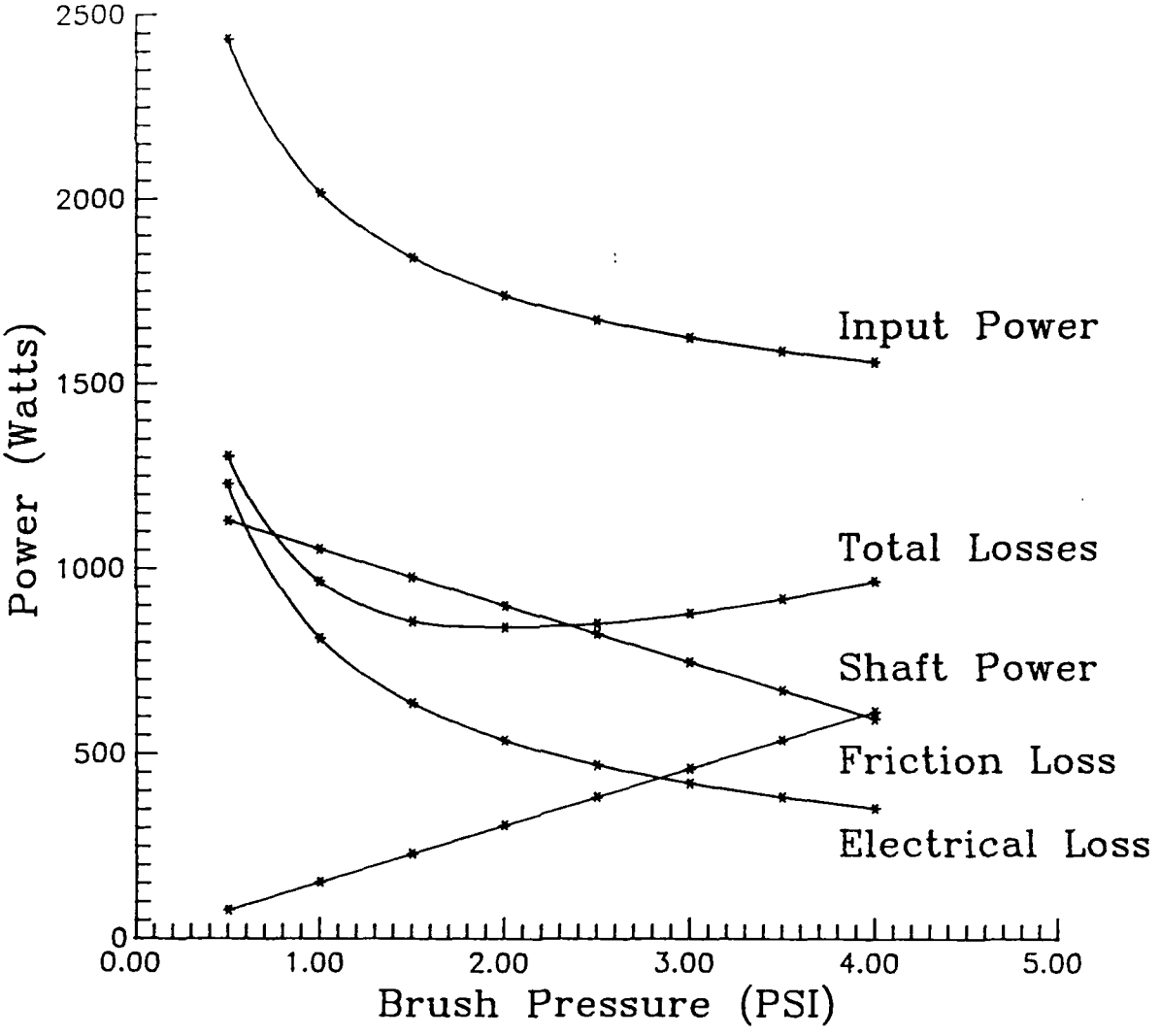


Figure 3.2.13 Motor Power and Losses Vs. Brush Pressure for 100% Field Coil Ampere Turns. Speed is 3000 RPM. Current is 1000 Amperes.

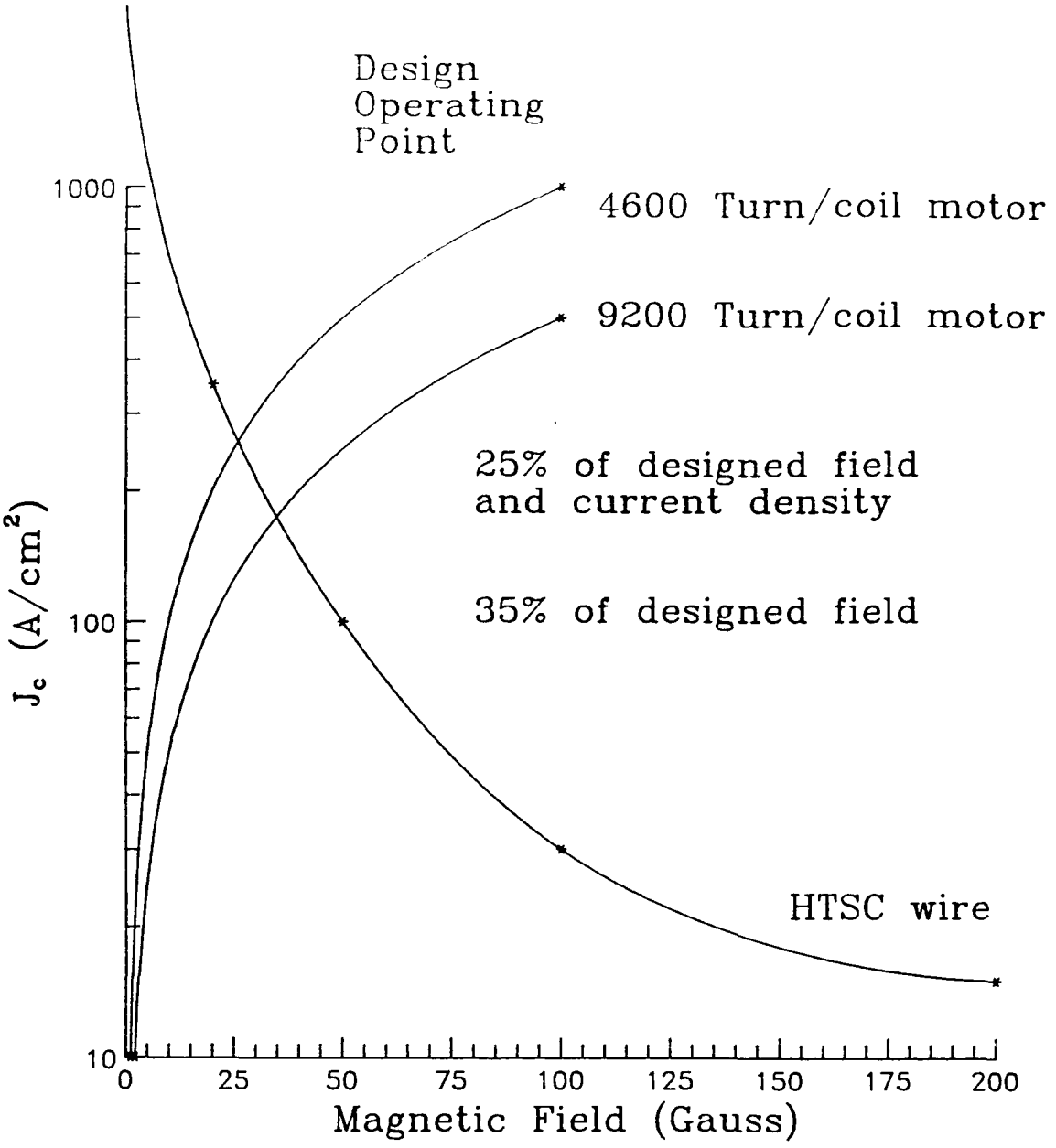


Figure 3.2.14 Current density Vs. magnetic field for HTSC wire and for motor coils.

Amperes/cm$^2$. This is a 40% improvement, but takes twice the length of wire. The additional turns would be very difficult to justify.

Figures 3.2.15 through 3.2.17 show calculated power and losses versus brush pressure for field strengths of 50%, 35%, and 25% of the designed level. As the field is weakened, the motor is capable of producing less and less torque. As previously shown, with the wire in its current state of development, with uniform current distribution, we should be able to get 25% of designed field from the coils.

We should be able to do better with a non-uniform current distribution. Since only the ends of the coil are at the maximum flux density, we can theoretically operate at a higher current density in the middle of the coil and get more total Ampere-turns than with one single coil. Figure 3.2.18 shows the current density versus magnetic field for the HTSC wire on an expanded scale. Since the magnetic field is lower in the middle of the coil, we can increase the current in those sections, resulting in more total ampere turns. Figure 3.2.19 shows the current density and flux density distribution of the coil divided into six smaller coils, each with separate excitation, optimized for maximum total Ampere turns.

This approach can theoretically give us 20% improvement over a uniform current density configuration, or an equivalent of 300 Amperes/cm$^2$ or 30% of the original designed field. Figure 3.2.20 shows power and loss curves versus brush pressure for the 30% field case. In actuality, we may be able to get even better improvement. Each coil is limited by its weakest section. Smaller coils reduce the likelihood of a really bad section. Since no two coils will be the same, we can characterize the coils and optimally place them

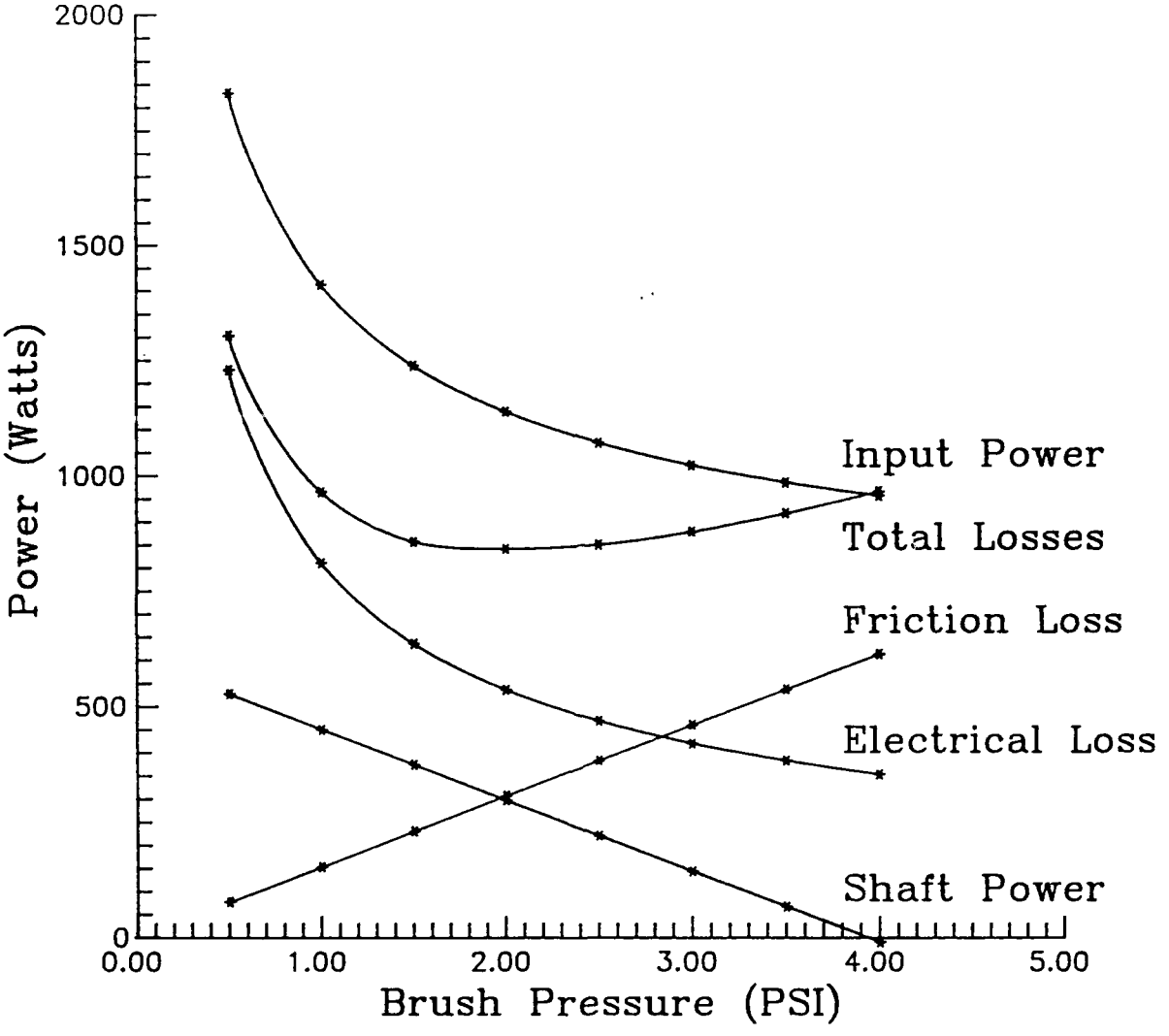


Figure 3.2.15 Motor Power and Losses Vs. Brush Pressure for 50% Field Coil Ampere Turns. Speed is 3000 RPM. Current is 1000 Amperes.

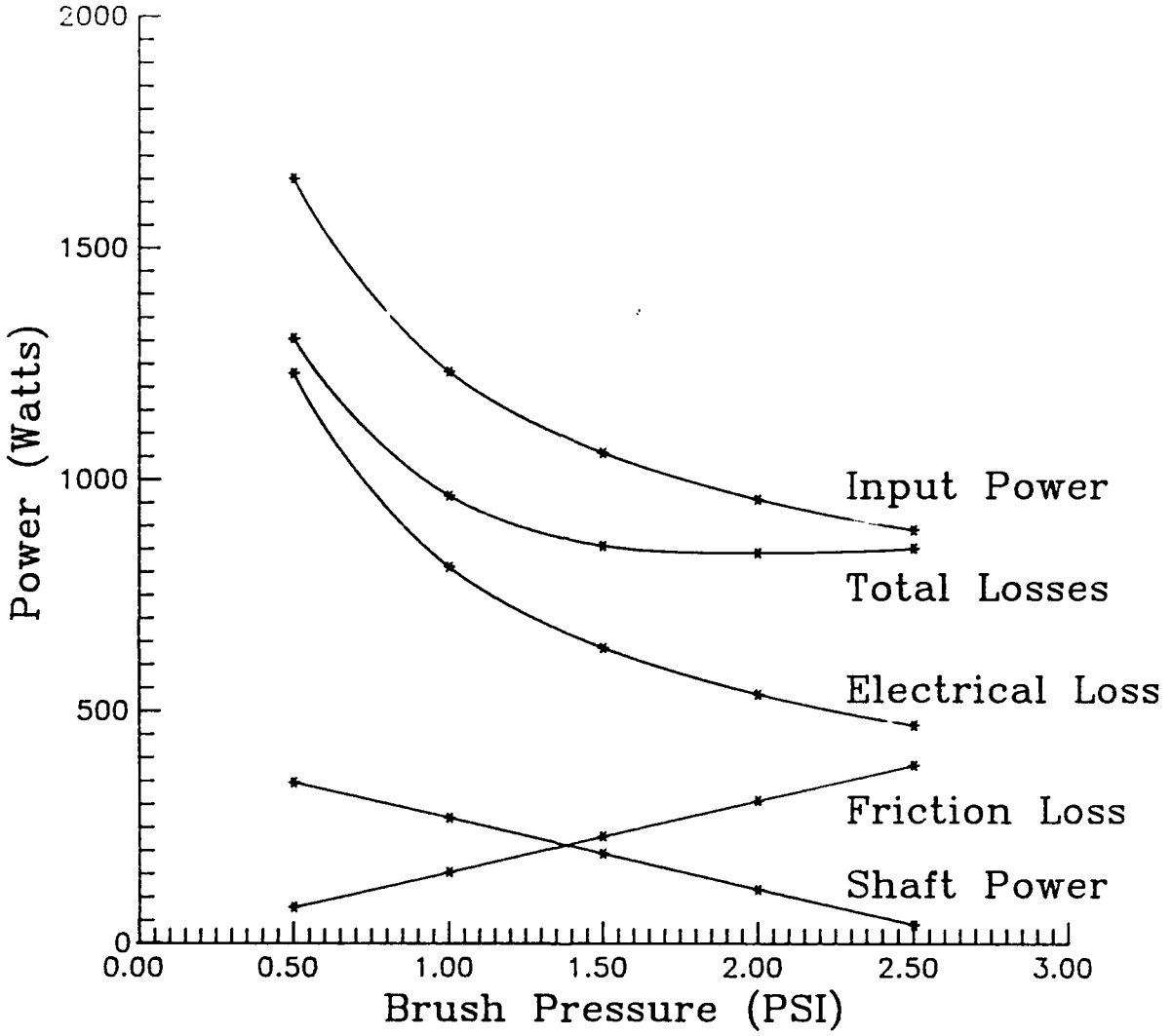


Figure 3.2.16 Motor Power and Losses Vs. Brush Pressure for 35% Field Coil Ampere Turns. Speed is 3000 RPM. Current is 1000 Amperes.

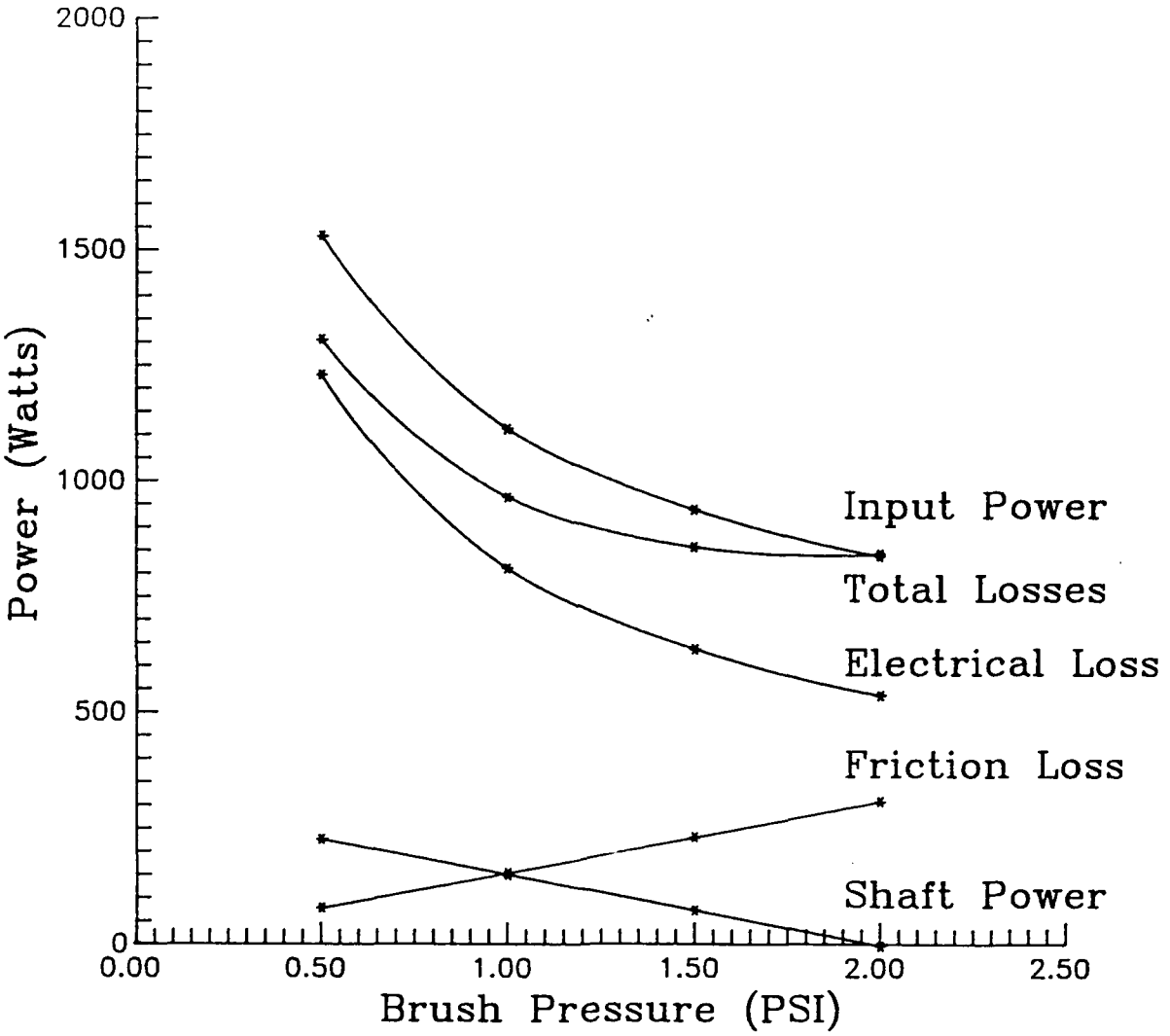


Figure 3.2.17 Motor Power and Losses Vs. Brush Pressure for 25% Field Coil Ampere Turns. Speed is 3000 RPM. Current is 1000 Amperes.

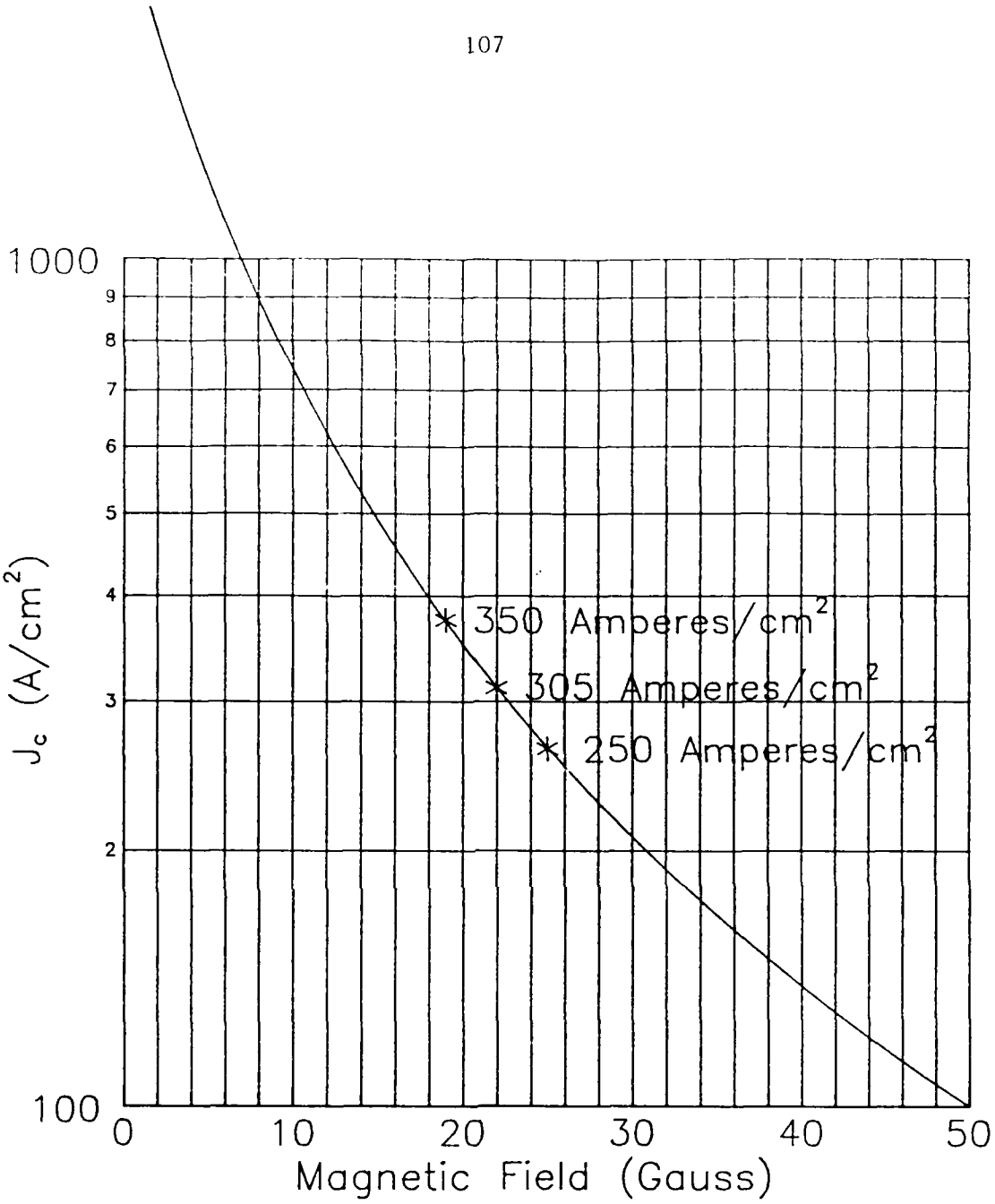


* Coil Operating Points

Figure 3.2.18 Current Density Versus Magnetic Field for HTSC Wire.

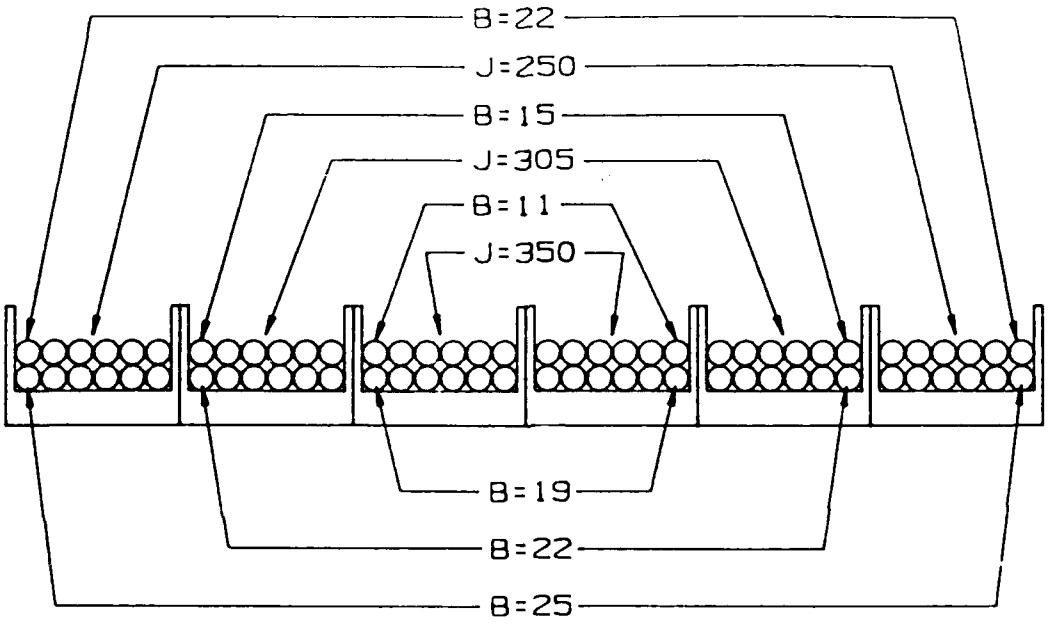


Flux Densities(B) in Gauss
Current Densities(J) in Amperes/cm$^2$

Figure 3.2.19 Flux Densities and Current Densities in Six Small HTSC Coils with Optimized Current Distribution

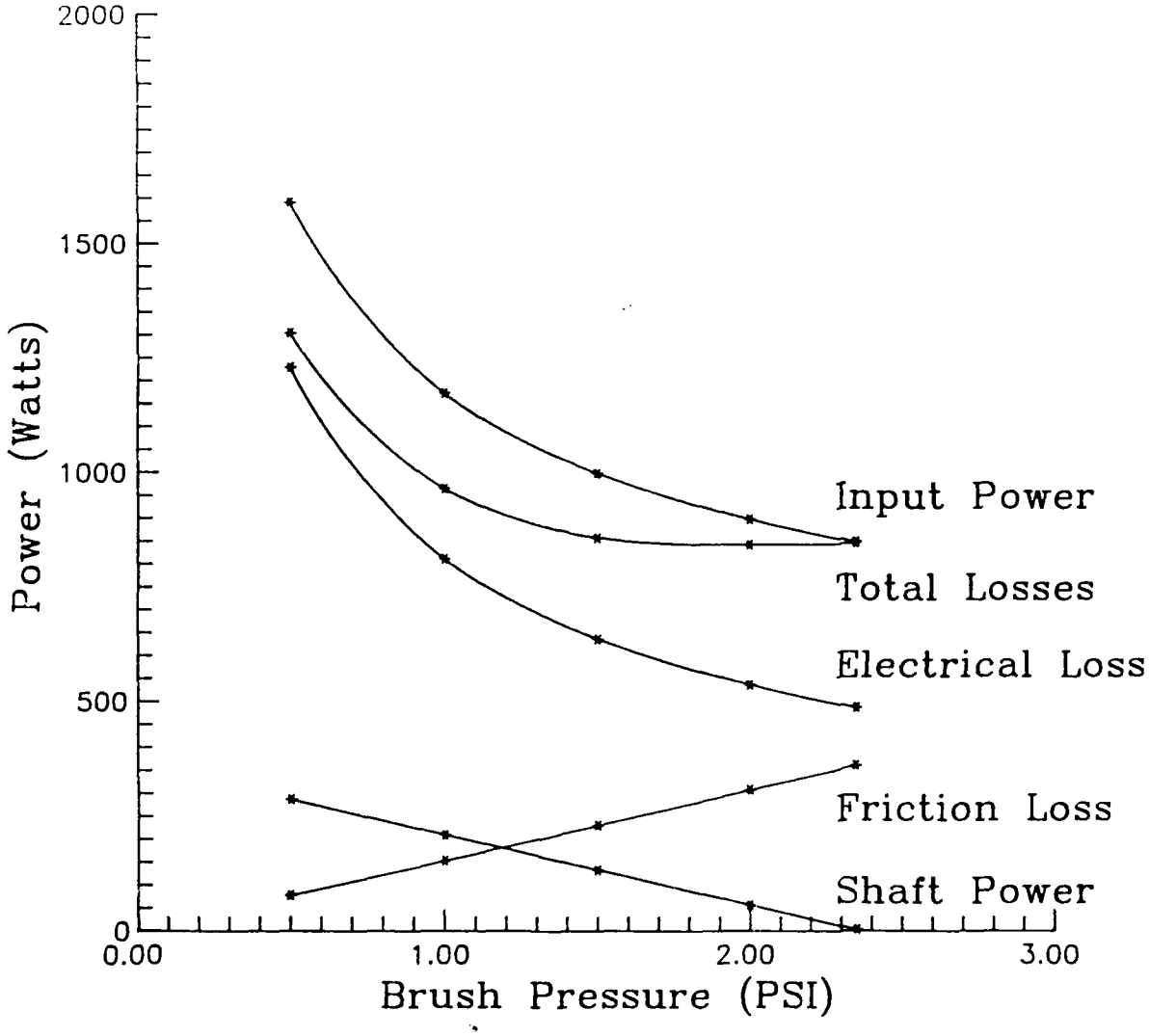


Figure 3.2.20 Motor Power and Losses Vs. Brush Pressure for 30% Field Coil Ampere Turns. Speed is 3000 RPM. Current is 1000 Amperes.

for maximum current density in a magnetic field. The smaller coils will be easier to handle and will be less prone to damage.

As wire properties improve, we can rewind the coils and operate closer to the full designed field performance.

### 3.2.3 Testing of the homopolar DC motor with copper field windings

Since CPS has not yet produced enough HTSC wire to wind the homopolar motor, we built the first version using copper wire for the field winding. We just completed the construction of the copper field winding homopolar DC motor. We started testing the motor but most of the testing will continue next quarter and be reported in the next report.

One of the main ingredients for a homopolar DC motor to work is the flux through the rotor and between the brushes. Using one of the six field coils as a search coil connected to a fluxmeter, we measured the flux produced by the coil. The results are plotted in figure 3.2.21. At the designed level of 575 Ampere turns, the measured flux of 0.0130 Webers is within 1% of the 0.0129 Webers calculated from the finite element model.

Most of the error at the other operating points is due to the error in the model of the B-H characteristics of the steel in the finite element program. In the previous section of the report, we calculated that the performance of the HTSC wire would allow us to operate at 30% of the designed field which would be 0.00390 Weber of flux at the field coil. From the measured values of flux, we get only 0.00345 Webers or 27% of the designed flux. This would put the performance of the motor between the curves calculated in figure 3.2.17 and 3.2.20. All things considered, this is about the same overall performance.

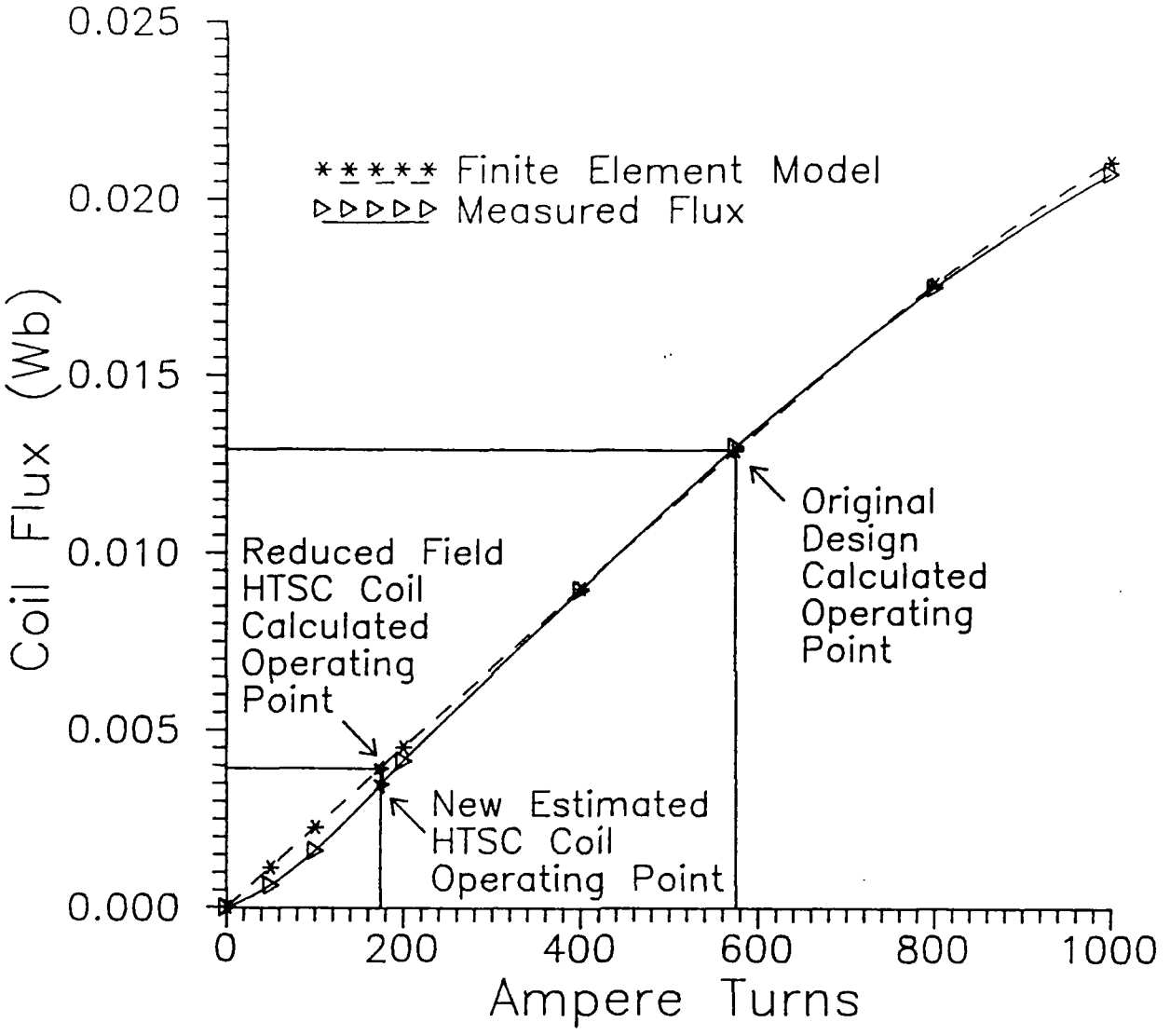


Figure 3.2.21 Flux Through Field Coil Versus Field Coil Ampere Turns.

Next quarter, we will wear in the brushes, and then we will be able to measure back EMF, friction, voltage drops in the brushes, and torque versus speed for various voltages and currents.

## 3.3 Brushless DC Motor Using Trapped Flux HTSC Magnets

The concept of trapping flux in a superconductor coil or in bulk material to make a super high energy "permanent magnet" is a fascinating one. As the flux trapping capability of HTSC materials improves, this concept can become a reality for motor applications. In theory, these magnets could be five to ten time higher energy than conventional rare earth magnets of today.

Just as conventional permanent magnets need to be magnetized, HTSC coils or bulk material needs to be "magnetized". A magnetic field is applied while the superconductor is above the critical temperature, and then the superconductor is cooled below the critical temperature. When the field is removed, currents in the superconductor will circulate to maintain the field and keep it from decaying. In a brushless motor, this would done by having superconducting stator windings in a cryostat, and a rotor with a superconducting ring or coils in its own cryostat. The stator would be cooled and high currents would be put through the superconducting windings while the rotor was still above the critical temperature. The rotor would then be cooled to trap the flux. The rotor would then act much like a permanent magnet rotor.

To analyze the performance of a motor design, finite element magnetic field modeling was used. An air core motor design with a stator frame that is 11 inches in diameter and an axial length of active material of 5 inches was modeled. Figure 3.3.1 shows a motor cross section with rotor and stator

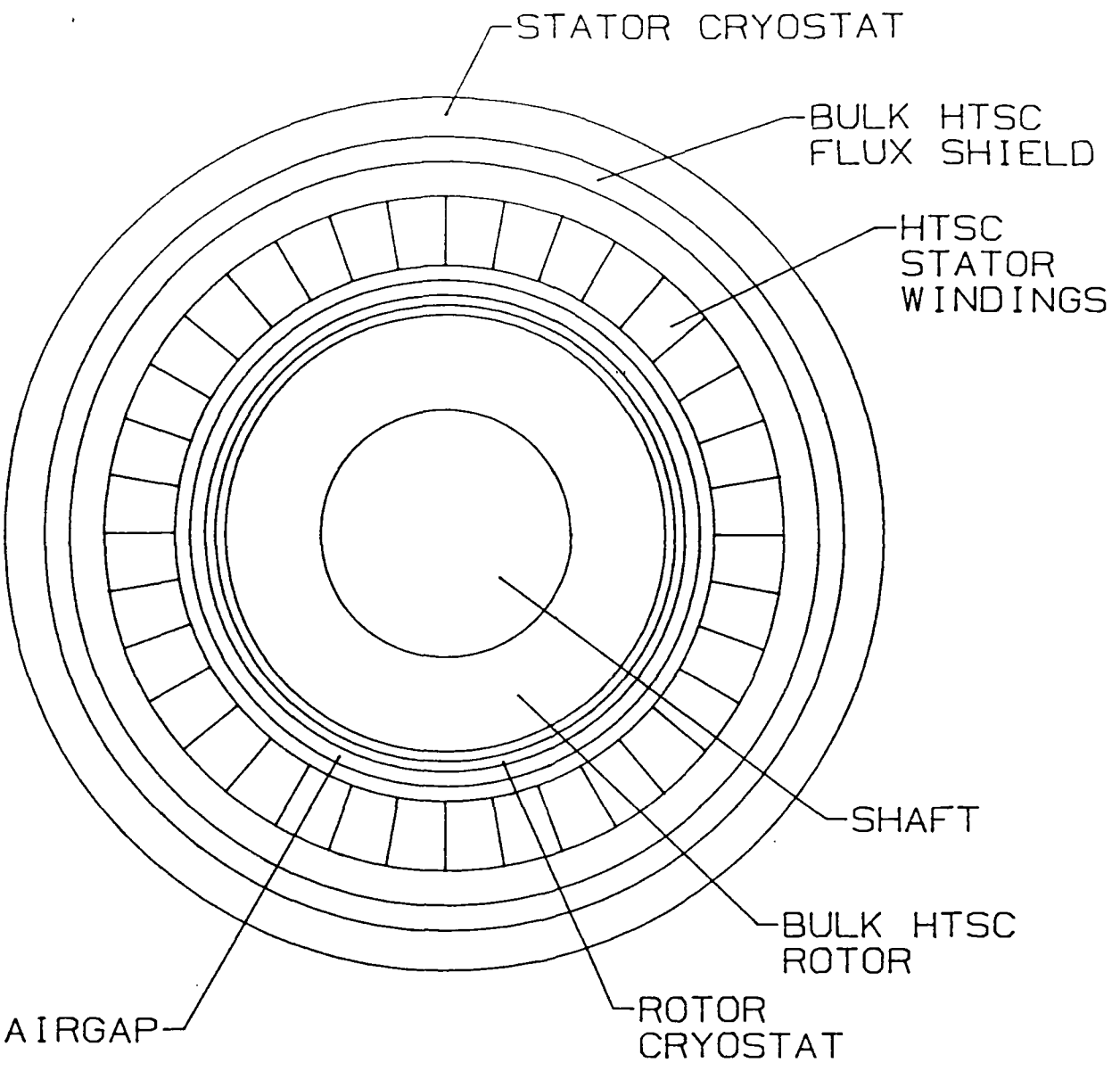


FIGURE 3.3.1 BRUSHLESS DC MOTOR WITH HTSC STATOR WINDINGS AND BULK HTSC ROTOR

cryostats. The HTSC stator windings, bulk HTSC stator shield, and bulk HTSC rotor are also shown. Figure 3.3.2 shows 1/6 of the six pole motor while the stator is supplying flux to the rotor. The HTSC winding is operating at a current density of 100,000 Amperes/$cm^2$ in a 2.0 Tesla field, with 20% of the coil space consisting of HTSC material. This produces a peak field of 1.0 Tesla on the surface of the rotor. When the stator field is removed, Figure 3.3.3 shows the same flux emitting from the rotor. This assumes the ideal condition that 100% of the flux is trapped. In reality, some flux is lost. Depending on the HTSC material processing, a lot of flux could be lost. Since that is not known yet, we will assume an ideal flux trapping material for this exercise. Figure 3.3.4 shows the rotor flux combined with the stator flux in the peak torque position. The current density in the stator winding is still 100,000 Amperes/$cm^2$ in the HTSC material occupying 20 % of the coil volume. The a peak flux density in the coil is 2.0 Tesla. The peak flux density in the air gap is 2.4 Tesla. The torque calculated for these conditions is 2439 Newton meters. At 1800 RPM that would be 616 horsepower.

Even though this motor could theoretically produce 2439 Newton meters of torque, the practical mechanical aspects of the design would limit the torque to a much lower value. The sheer strength of materials would limit the safe output to around 100 horsepower or less at 1800 RPM.

For comparison, an induction motor of the same size in a totally enclosed fan cooled 284T frame is 15 horsepower at 1770 RPM with a service factor of 1.25. The maximum continuous rating is 18.75 horsepower. A brushless rare earth permanent magnet motor using samarium cobalt or neodymium-iron-boron magnets in the same package size can produce 180 Newton

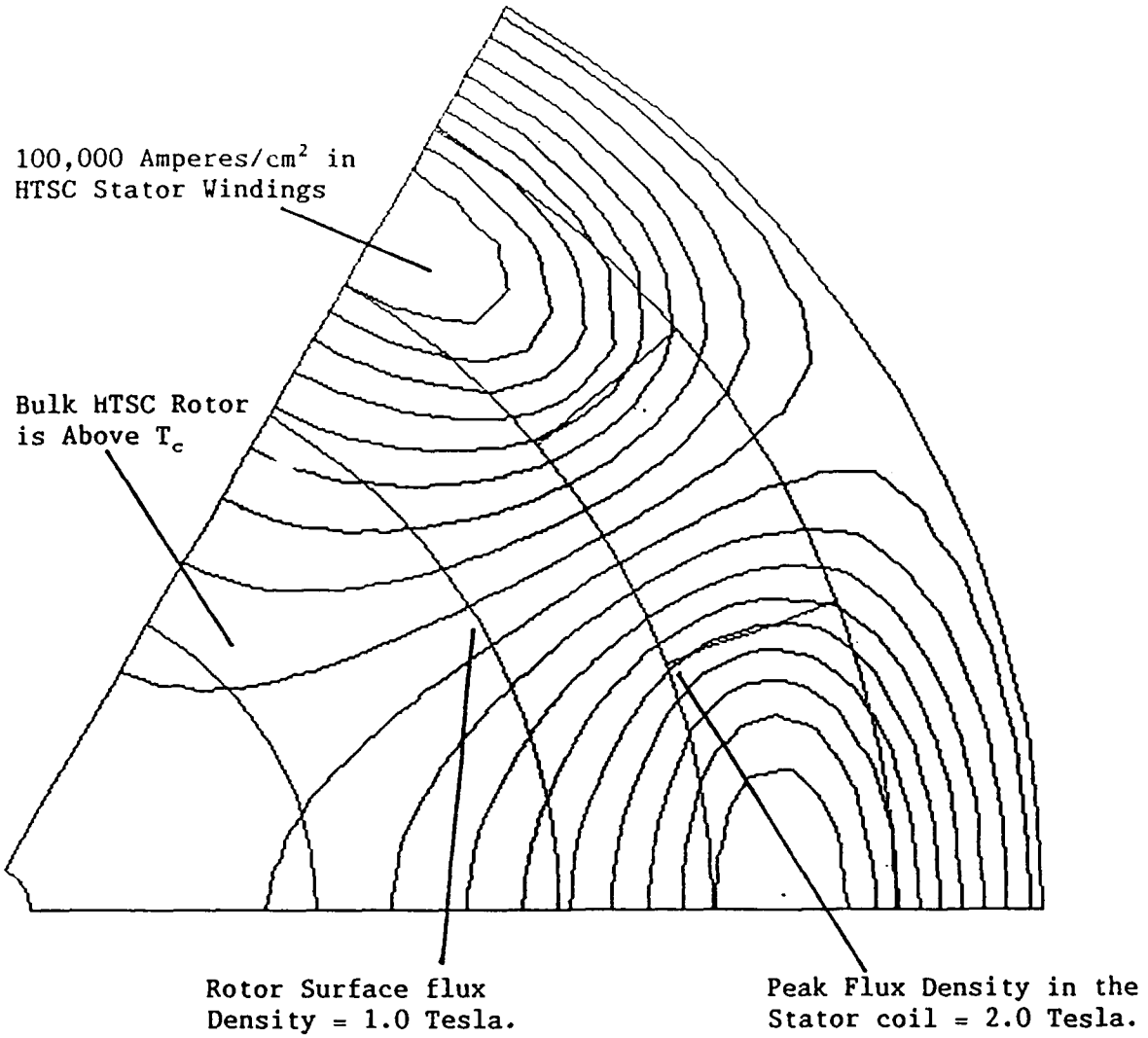


Figure 3.3.2 HTSC Stator Supplies magnetic Field to charge the Rotor of a Superconductor Brushless DC motor.

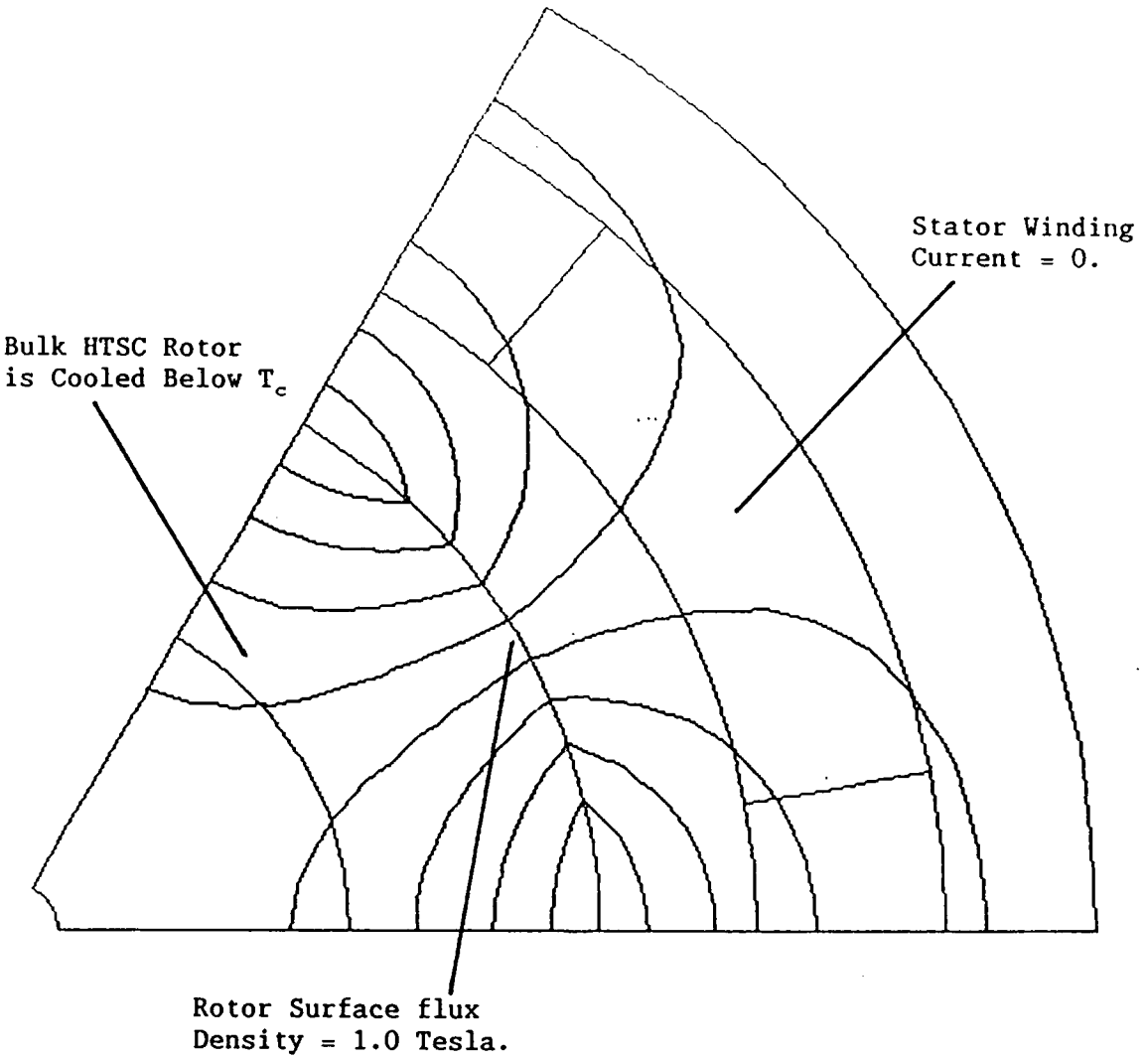


Figure 3.3.3 Flux is Trapped in the HTSC Material After the Rotor is Cooled in a Magnetic Field.

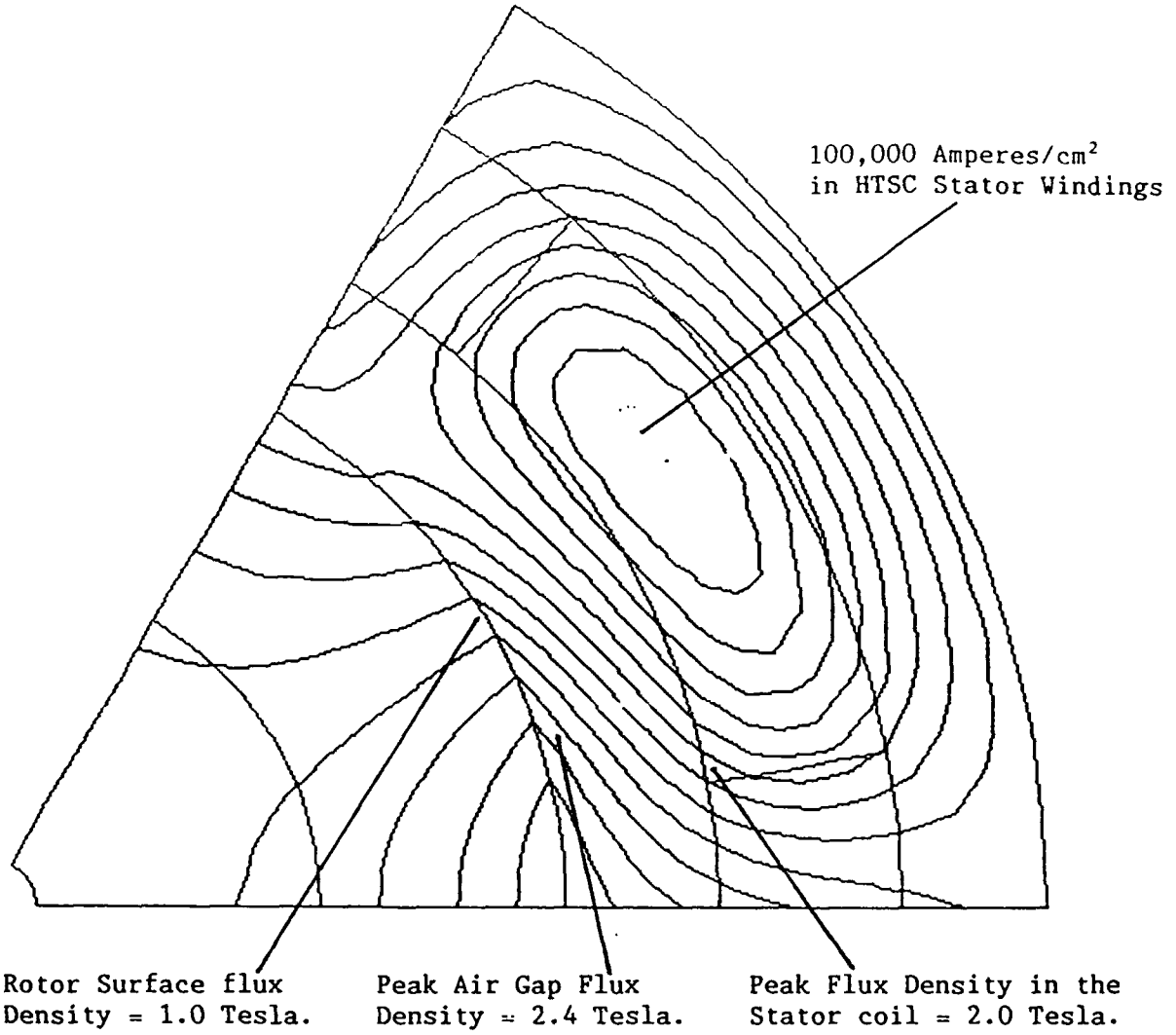


Figure 3.3.4 HTSC Brushless DC Rotor Flux and Stator Flux Combine in the Peak Torque Position.

meters of torque at 1800 RPM or 45.5 horsepower continuously in the same package size.

The torque of the HTSC brushless motor will vary with the stator current density squared. The rotor flux is proportional to the stator flux and the torque is proportional to the product of the two fluxes. The torque in Newton meters, and the horsepower at 1800 RPM are given by:

$$\text{Torque} = 2.439 \times 10^{-7} J^2$$

$$\text{Horsepower at 1800 RPM} = 6.163 \times 10^{-8} J^2$$

Where : J is the current density in Amperes/$cm^2$

Figure 3.3.5 shows the horsepower versus current density for this motor design. For low current density, the power output is very low. A current density of 34,000 Amperes/$cm^2$ with a peak coil flux density of 0.54 Tesla would produce 45.5 horsepower like the rare earth brushless DC motor. In order to produce 18.75 horsepower like the induction motor, the HTSC brushless DC motor would need 22,000 Amperes/$cm^2$ in a peak field of 0.35 Tesla.

These comparisons apply for the ironless brushless DC motor design presented here. An iron core motor would require a lot less current density in the HTSC wire and bulk rotor material to get torque comparable to conventional motors.

We have started work on an iron core trapped flux motor. CPS Superconductor has demonstrated flux trapping in a melt textured disc of HTSC material. They have measured 300 Gauss or 300 Oersteds that persist as trapped flux in air. We are designing an iron core brushless DC motor that

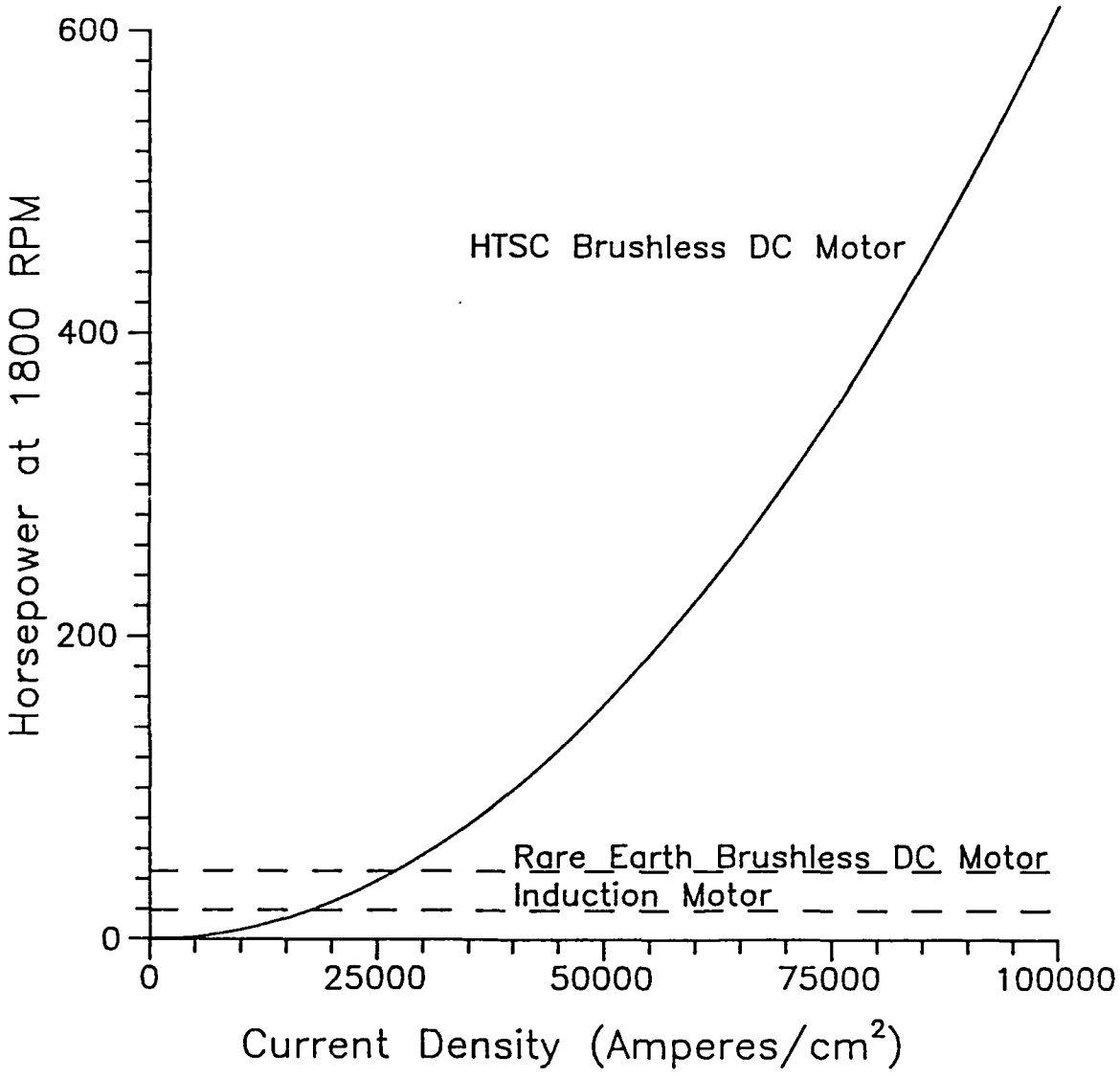


Figure 3.3.5 Horsepower versus Current Density in HTSC Stator Windings.

will work with trapped flux fields below 300 Gauss or 300 Oersteds. The results will be reported next quarter.

## 3.4 Other Advanced HTSC Motor Designs.

As HTSC wire properties improve, Advance high performance superconductor motors will become possible. We are continually looking at possible motor designs to best take advantage of new wire properties as they become available. We are also looking at what current densities in a magnetic field are necessary for a viable motor in the various designs.

### 3.4.1 High Performance Homopolar DC Motor

The Homopolar DC motor is still an attractive design for ship propulsion or other large scale applications where high current low voltage power is available. They are well suited to superconductor field windings because of the absence of AC fields and currents. When high current and low voltage is not available, as in industrial applications, Homopolar DC motors are probably not the best choice. High voltage, low current versions of homopolar motors tend to be large and not as efficient as other motor designs.

### 3.4.2 Heteropolar DC Motor

For applications with high voltage input power requirements, Heteropolar DC motors are an alternative. In the third quarterly report and the first annual report, we discussed a heteropolar DC motor with HTSC field windings to produce up to 3 Tesla in the air gap with no steel in the magnetic circuit and conventional copper windings in the armature. This design had some advantages over a conventional motor but did not have a huge increase in the power density because it was modeled with copper armature windings and a

lot of space was needed for flux shielding. We will be considering a version which not only has HTSC field windings, but HTSC armature windings and HTSC flux shielding. This "all HTSC" version will have much higher power density. The power produced would have the same type of characteristics as the brushless DC motor performance shown in figure 3.3.5.

Ultra high torque comes from a combination of high flux density and high current density.

## 3.5 Summary

We have designed and built a homopolar DC motor that will operate with HTSC field coils submerged in liquid nitrogen. The HTSC field was designed to operate at a $J_c$ of 1000 Amperes/cm$^2$ in a field of 100 Gauss. The motor has been built with copper field windings while waiting for the HTSC coils to be available. Testing has started and will continue into the next quarter.

Brushless DC and other motor concepts have been evaluated. Trapped flux brushless DC motors are an attractive possibility. Since CPS and others have demonstrated flux trapping, we are now designing an iron core brushless DC motor that will use the flux trapping melt textured HTSC material.

# SECTION 4

# GENERAL DISCUSSION AND SUMMARY

## 4.1 General Discussion

It is appropriate to discuss the status of the program after two years of effort. In the area of HTSC wire, we contend that the materials properties necessary for practical applications have been demonstrated by several groups in bulk material for YBCO at 77K and BiSCCO at lower temperature. Methods for fabricating these as wire have been demonstrated by ourselves and others. The task before us is two-fold: 1) to achieve these excellent bulk properties in wire form; and 2) to fabricate the wire in the form which is required, i.e. kiloamp current ratings in kilometer lengths. We have restructured our development program to address these tasks in both YBCO and BiSCCO. Prospects for successfully achieving this at CPS Superconductor are discussed below.

In the area of HTSC motors, the fact remains that wire-wound machines require that the wire exist before they can be built. Our DC homopolar was built to operate with low $J_c$ wire, but it still requires a very large quantity of wire (6 kilometers of our monofilament). About a 10-fold increase in the scale of the present wire process is required to produce this quantity. It makes sense to postpone this activity until the wire properties justify the effort.

A new opportunity is presented by the novel trapped flux "permanent magnet" motors. This offers the prospect of building a significant HTSC motor, which can meet or exceed the torque and power density of any existing conventional electric motor. In the short term, the machine can be built as a

hybrid with HTSC replica magnets and copper stator windings (which can be later upgraded with HTSC stator windings). We plan to emphasize these activities in the following year.

## 4.2 Prospects for Practical Applications for YBCO Wire at 77K

A year ago many knowledgeable experts were justifiably pessimistic about the prospects of practical HTSC wire at 77K. Distressing new data on flux lattice motion, combined with intractable weak link problems, created an attitude captured by the Science article which announced that "the party is over".[14] Fortunately, much has changed, and one can be more optimistic about practical applications.

Electromagnetic applications require kilometers of strong, flexible, metal-stabilized wire with certain electrical properties. Figure 4.1 is a plot of critical current density vs. magnetic flux density, which contrasts the July 1990 state-of-the-art for Y-123 with application needs. The latter are indicated with an "application window" which approximates the range of critical current and magnetic field of practical use for electromagnetic machinery. The window has a lower $J_c$ limit of 10,000 A/cm$^2$ as the smallest useful current density, and a lower B of 2-T, near the upper range of ordinary iron-core resistive magnets. The upper limit of a few hundred thousand amperes/cm$^2$ recognizes that it becomes impractical to stabilize superconducting wire above this range. Superimposed on Figure 4.1 are the most recent Y-123 data at 77K. The data divide into three classes: 1) sintered polycrystalline materials (SP); 2) melt-textured materials (MT); and 3) irradiated melt processed materials.

---

[14]. Science, 26 May 1989, p. 914

The sintered polycrystalline materials can never have practical application. They are, however, the first materials that we have made in wire form in lengths greater than 100 meters. They have some of the physical attributes and manufacturing characteristics required for wire, but are deficient in electrical properties. Developing our silver clad SP wire was a necessary first step toward practical wire manufacturing.

The melt textured Y-123 materials have properties comparable to the pioneering 1987 work by Jin et al. on small pieces. We can distinguish between small batch specimens, like Jin's original sample and Salama's record-setting 75,000 A/cm$^2$ sample, and continuously processed material which could ultimately be developed into a wire. Examples of the latter are Hitachi's directionally solidified YBCO, the continuously MT rods reported recently by TCSUH, and the CPSS MT-wire made from fine fibers. These are in the 1000 to 10,000 A/cm$^2$ range at 1-tesla, which is encouraging progress, reflecting strong-linked material with the current density limited by flux pinning. J. Ekin[15] recently reported very high field transport measurements on samples cut from Salama's MT pellets. These samples had a transport $J_c$ about 9600 A/cm$^2$ at 8 tesla and 1100 A/cm$^2$ at 30 tesla, which proves conclusively that high current-high field material can be achieved at 77K.

Van Dover et al. at Bell Labs demonstrated that irradiation can create defects which are potent pins. Figure 4.1 shows 600,000 A/cm$^2$ at 0.9 T for a neutron irradiated single crystal. Recently the TCSUH group achieved comparable results with neutron irradiated melt textured pellets. Their $J_c$(magnetic) vs. B data hit the application window.

---

[15]. J. W. Ekin, National Institute for Standards and Technology, private communication

Of course irradiation, especially neutron irradiation, is not a practical method for creating defects for pinning sites. But similarly potent defects can be created by conventional heat treatment. Again Jin's group at Bell Labs leads the way with their elegant demonstration[16] that decomposition of Y-124 can create pinning defects in the resulting Y-123 sufficient to support a magnetic $J_c$ of 100,000 A/cm$^2$ at 0.9 T.

There is no doubt that MT wire, once pinning sites are introduced, will achieve $J_c(B)$ characteristics within the application range. It will be a challenge to achieve the physical attributes and manufacturing characteristics. Early result indicate that we can produce silver cladding on a 125-micron MT wire by post-firing on a green cladding. Preliminary results on melt-texturing a previously clad fiber are encouraging. Such a fine diameter silver clad wire should have physical properties similar to our present SP wire. Manufacturing is the issue. Melt texturing is very slow, with growth rates about 0.5-1 cm/hr. Our strategy to multiply the MT wire production rate by simultaneously propagating very many molten zones along the length of a wire, such that the entire length can be processed in a relatively short time. The first version of the apparatus for this has been designed and is being built.

## 4.3 Prospects for Practical Applications for BiSCCO Wire at 77K and Lower Temperatures

Quite a few groups have reproduced Vacuumschmetze's stunning data on high $J_c$ at very high field for BiSCCO wire at 4.2K, so little doubt remains that practical low temperature - high temperature superconducting magnets will eventually be made BiSCCO wire. Here the fabrication challenge will be to

---

[16]. reported in Science, 8 December 1989, p.1243

achieve in kilometer-long wires the properties exhibited by, eg. Sumitomo's 2.4-cm long sample wires.[17] Properties are less impressive at 77K, although Sumitomo and Furukawa have made significant progress, achieving almost a year ago[18] several thousand amps/cm$^2$ at 77K in a (suitably oriented) 1-telsa field.

At this point we have demonstrated the fabrication of rolled BiSSCO tape from the fiber method. We anticipate no difficulties in scaling this method up to the hundred-meter level. We have not yet achieved significant $J_c$ values at 77K, and have not done any measurements at lower temperatures. One of our goals for the coming year is to meet or exceed the electrical performance of powder-in-tube wire using our monofilament and multifilament BiSCCO fiber process. We plan to devote about half of our efforts next year to BiSCCO, and so anticipate rapid progress.

---

[17]. Y. Iwasa of the Bitter National Magnet Lab reported 55,100 A/cm$^2$ at 20K in a 19.75 tesla field on a 4mm-0.15mm-24mm tape at the July 25, 1990 Review Meeting of the DOE STEPS Program.

[18]. K. Sato et al., "High $J_c$ Silver-sheathed BiPbSCCO Superconducting Wires", Superconducting Materials and Magnets, September 4-6, 1989

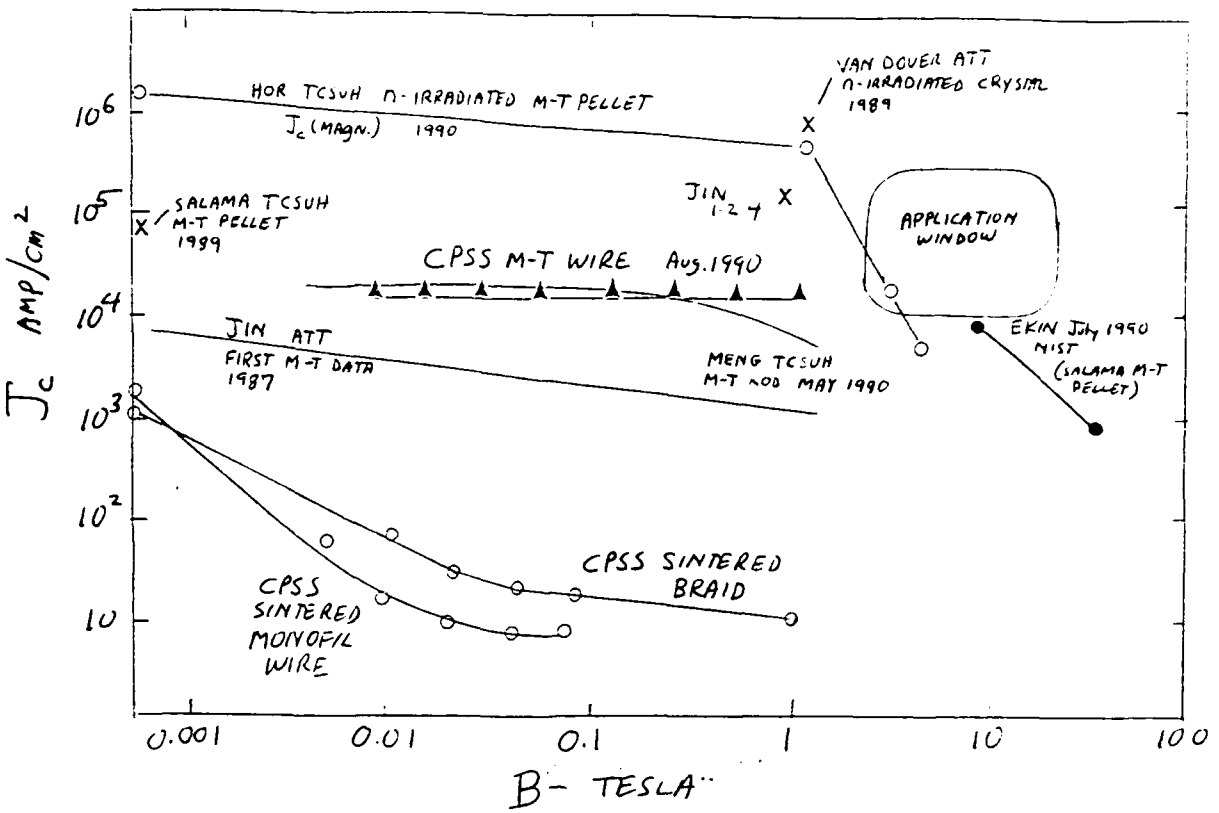


Figure 4.1 Critical Currents in Bulk YBCO at 77K

State of the Art, July 1990

## 4.4 Summary

We demonstrated our fiber process for wire by fabricating hundreds of meters of silver clad wire from both $YBa_2Cu_3O_{7-x}$ (Y-123) and $Bi_2Ca_2Sr_2Cu_3O_x$ (BiSCCO). The fiber spinning and green cladding operations produce kilometer-long continuous material. Much effort was devoted to scaling up the wire process to fabricate HTSC coils for a DC homopolar motor. The coils are not yet completed, but we have wound multiple turns of wire on the coil bobbins, and characterized the superconducting properties of the coiled wire. We have demonstrated multifilamentary conductors as cables and coils of sintered silver clad braided wire. The sintered polycrystalline wire has self-field critical current densities ($J_c$) as high as 2800 A/cm$^2$, but are weak-linked, so the $J_c$ falls rapidly with magnetic field.

To overcome the weak-link problem we "melt texture" the sintered wire by directional solidification. We have a continuous melt texturing process for Y-123 wires which, while slow, can produce textured wire up to 0.5 meters long. The melt textured wire has 77K transport $J_c$ above[18] 11,770 A/cm$^2$ in self field and 2100 A/cm$^2$ at 1 telsa.

The Emerson Electric DC homopolar HTSC motor was designed to operate with low $J_c$ wire to be a test bed for wire. The machine has been fabricated and operated conventional copper coils. A novel class of superconducting motors have been designed at Emerson Electric subcontract, using trapped flux in melt textured Y-123 as "magnet replicas" in an new type of permanent magnet motor.

---

[18]. The apparent critical current was limited by Joule heating of the silver paint contacts, so the actual 77 K is higher by an unknown amount.

These have the promise for very high output motors, and can be built in the very near term. The stator element and part of the rotor of the first prototype machine presently exist, and the HTSC magnet replica segments are now being fabricated.

APPENDIX A

Spring MRS Meeting

# RAPID THERMAL PROCESSING OF HIGH TEMPERATURE SUPERCONDUCTING FIBER

J.W. HALLORAN*, M.J. NEAL*, D.S.GINLEY**, E.L. VENTURINI**, J.F. KWAK**, R.J. BAUGHMAN**,M.A. MITCHELL**,B.MOROSIN**,S.N. BASU*** and T.E. MITCHELL***

*CFS Superconductor Corporation, Milford, MA 01757 **Sandia National Laboratories, Albuquerque, NM 87185 ***Los Alamos National Laboratories, Los Alamos, NM 87545

## Abstract

We report on the rapid thermal processing (RTP) of $YBa_2Cu_3O_7$ (Y-123) fibers. Unsintered fibers are densified by RTP. We show that fibers which were originally semiconducting and tetragonal before RTP form normal twinned orthorhombic material after processing for 2-4 seconds above 1000°C with a 3 min. cool down in oxygen. They subsequently show $T_c$ to 90K and magnetization indicative of substantially shielding. We present the effects of varying the RTP parameters on the morphology, phase, and superconducting properties of a number of tetragonal and orthorhombic Y-123 fibers.

## Introduction

We have previously reported that Rapid Thermal Processing (RTP), using heat treatments as short as one second at temperatures around 1000°C, is an effective processing technique for high temperature superconductors [1,2]. RTP of $YBa_2Cu_3O_7$ (Y-123) fibers has produced material with $T_{c,r=0}$ of up to 90K and self field $J_c$ to 1200 A/cm$^2$. RTP rapidly densifies unsintered material, creating a microstructure characteristic of the fiber composition, RTP temperature and time. Of particular interest is the fact that RTP annealed Y-123 is superconducting immediately after the RTP anneal, without requiring the 500°C oxygen anneal which is conventional for Y-123. Indeed, conventionally sintered Y-123 fibers, which are semiconducting in their as-sintered state, become superconducting after an RTP treatment, indicating that very rapid oxygenation occurs during RTP.

In this paper we discuss the development of the microstructure when sintering occurs by RTP and characterize the phenomenon of rapid oxygenation by examining superconducting properties of pre-sintered Y-123 after RTP treatment.

## EXPERIMENTAL PROCEDURE

### Fabrication of Fibers

Fibers were produced using a proprietary process in which Y-123 powders are compounded with a thermoplastic resin so they can be spun into continuous "green" fibers using a conventional textile fiber spinning machine. Most fibers used in this study had a green diameter of 125 microns. The powder was a phase pure Y-123 with 1.6 micron average particle diameter. Copper oxide-rich fibers were prepared with a 5 wt% admixture of CuO. Fibers which were RTP annealed in the unfired state had undergone a binder burnout in which the fibers were heated in air at 20°C/minute to 500°C, held for 10 minutes, then cooled to room temperature at 10°C/minute. This treatment removes most of the organic material, but does not allow any sintering of the Y-123. Pre-sintered fibers received a binder burnout and a 945°C/30 min sintering anneal in a continuous furnace, yielding a sintered density about 90% of theoretical.

### Rapid Thermal Processing

Burned-out unsintered fibers and presintered fibers were RTP annealed in an ADDAX-AET model R-1000 rapid thermal annealer. The fibers were supported on a 4" Si wafer coated with 1 micron of silicon nitride. The system was equipped with two low mass thermocouples with one or both in direct contact with the fibers. Before during each run the system (100 cc chamber volume) was purged with high purity oxygen at 3 liters/sec. Typical run conditions (all under 1 atm. oxygen) were: i) a 10 second wait period, ii) 4 second ramp to peak temperature, iii) hold at peak temperature 1-4 seconds, iv) cooling ramp to 600°C

in 96 seconds, v) ramp to room temperature in 180 seconds. The programmed measured temperature agreed within 1%, except when below 300°C where the actual cooling rate lagged the program. The coated Si wafer was an effective substrate in cases reported here, with no apparent reaction with the fibers during the brief RTP anneal. At higher temperature, fibers reacted with the substrate.

Characterization

After RTP, specimens were characterized in the as-fired condition, with no oxygen anneal. Oxygen anneals, though not discussed here, did improve the superconducting properties in some cases. Fibers were examined by X-ray diffractometry had patterns indicative of well formed orthorhombic Y-123, although in some cases the lines were not as sharp as our best material. Precession photographs indicated no preferred orientation. The microstructures were characterized by optical microscopy, scanning electron microscopy, and transmission electron microscopy. Transport properties were determined with standard 4-probe techniques. Magnetization measurements down to 5K were performed in a SQUID magnetometer at 100 Oe, and AC susceptibility at 10 Oe was measured down to 75K.

## RESULTS

Microstructure Development

Green Y-123 fibers sintered by RTP develop a sequence of microstructures depending upon time, temperature, and composition. It was generally observed that very rapid grain growth, suggestive of liquid phase formation, occurred in a narrow +/-25°C temperature window. Below the window there is local sintering of grains into dense patches, but no grain growth so the grain size remains 1-2 microns. As the window is approached, rapid grain growth creates distinctive blocky grains as large as 10 microns. At higher temperature, there is a profound change in grain morphology, creating locally oriented patches of elongated grains as large as 50 microns. Figure 1 is a series of SEM micrographs illustrating the evolution of microstructure with temperature and time for Y-123+5% CuO fibers. Figure 1A illustrates the fracture surface after a 1025°C/2 sec RTP anneal at, showing the blocky grain morphology. This microstructure is uniform throughout the cross-section of the fiber. A 4-sec RTP anneal at the same temperature creates the elongated grain structure shown in Figure 1B. Lower magnification views of this specimen, not shown here, show that the elongated grains form in circular patches with the grains radiating from a central nucleus. This suggests that recrystallization occurs by formation and growth of spherulites. The transition from blocky to spherulitic elongated grain morphology occurs more quickly at higher temperature. Figures 1C and 1D show blocky grains after a 1050°C/1 sec RTP anneal and elongated grains after a 1050°C/2 sec treatment. We find that similar microstructures develop in stoichiometric Y-123 fibers at about 25°C higher temperaturesl.

Both the blocky- and elongated-grain microstructures consist primarily of orthorhombic Y-123. This is confirmed by TEM of crushed fragments of fibers. Figure 2 is a bright field TEM of a fragment of a stoichiometric Y-123 fiber after an RTP anneal at 1025°C for 1 sec. The obvious twins indicate that the material is orthorhombic Y-123, a fact confirmed by electron diffraction.

Rapid Oxygenation

Green Y-123 fibers sintered by RTP are superconducting with zero resistance near 90K immediately after the rapid anneal [1]. We have also observed that Y-123 fibers pretreated with a conventional (eg., 925°C/30 min.) air sintering anneal to produce dense, largely tetragonal semiconducting fibers, can be rendered superconducting by RTP, suggesting that ultra-rapid oxygenation occurs in RTP. To investigate the rapid oxygenation effect, we prepared a series of stoichiometric Y-123 fibers by sintering fibers 30 minutes at 945°C in an atmosphere of flowing nitrogen. These $N_2$-sintered samples were semiconducting before RTP, but became superconducting after RTP treatment at 1000°C.

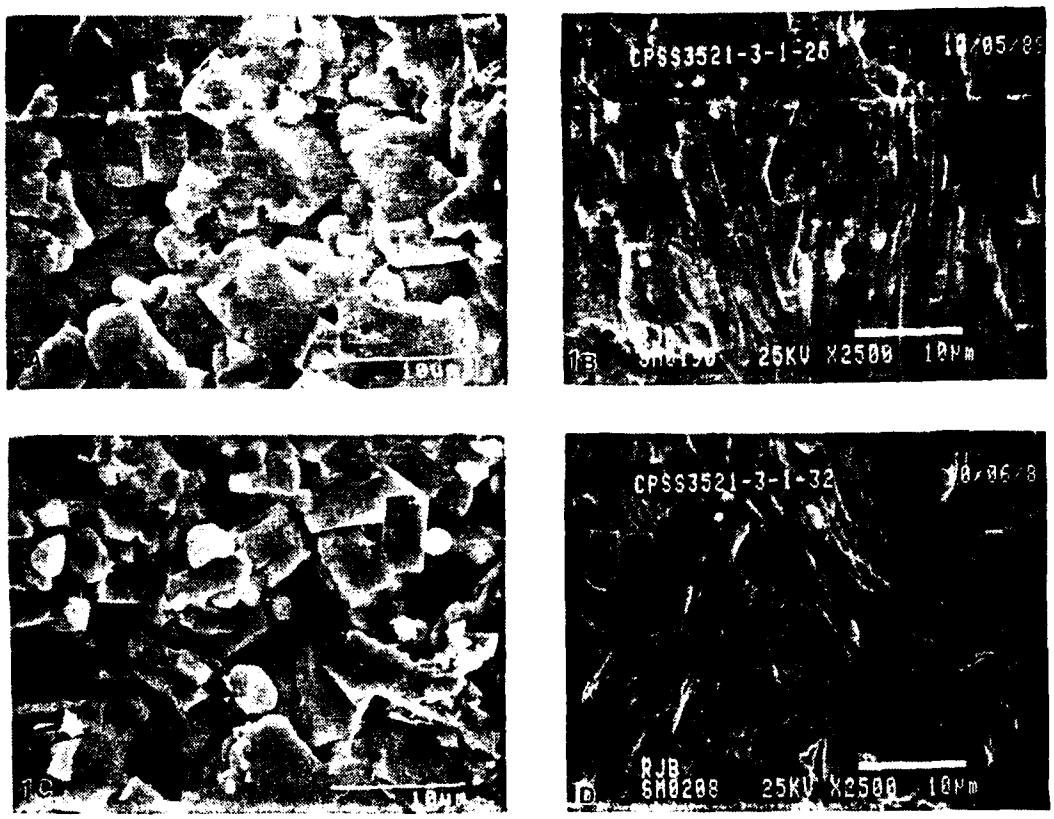


Figure 1 SEM Micrographs showing grain morphology in unsintered Y-123 + 5 wt% CuO wires, after RTP anneals of: A) 1025°C, 2 sec; B) 1025°C, 4 sec; C) 1050°C, 1 sec; D) 1050°C, 2 sec

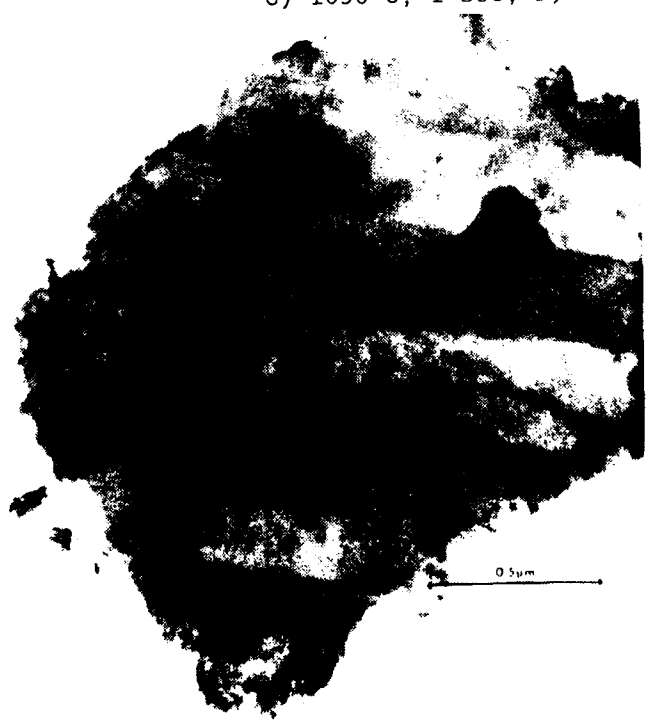


Figure 2 Transmission electron micrograph of twinned orthorhombic Y-123 from a stoichiometric Y-123 wire sintered by RTP at 1025°C

Figure 3, a plot of resistivity vs. temperature, illustrates that the $N_2$-sintered fibers had a resistivity above 2000 $\mu\Omega$-cm, with no hint of a resistive transition. A 1-second RTP treatment reduces the normal state resistivity below 300 $\mu\Omega$-cm, with a partial transition near 90K. After a 2-second RTP treatment, the specimen displays a broad transition with onset at 87K and zero resistance at 78K. The 4-second RTP treatment sharpens the transition, so that onset occurs at 92K with zero resistance at 87K.

Figure 4 shows the real and imaginary volume AC susceptibility down to 75K for the $N_2$-presintered fibers after 1000°C/1 sec RTP. No diamagnetism could be detected at 77K with this technique in the as-sintered specimen. The 2-second RTP sample has a small diamagnetic signal, reaching only -0.05 at 77K, while the 4-second sample has a diamagnetic susceptibility as high as -0.40 at 77K.

Table I displays the SQUID data for volume static susceptibility (diamagnetic shielding) in 100 Oe at 5K. Like other ceramic Y-123 samples, these RTP fibers have weak-link behavior, so in a 100 Oe field the grains are decoupled, allowing volume susceptibility to be estimated from the measured mass susceptibility. Completely superconducting grains would have a volume static susceptibility of $-1/4\pi$. We assume that the 5K data can be used as a rough indication of the extent of oxygenation of the Y-123. A more quantitative estimate would require corrections for the magnetic penetration depth and grain morphology. At 5K, the $N_2$ sintered sample had a measurable diamagnetic susceptibility, demonstrating that small fraction of orthorhombic phase exists after $N_2$ sintering. The susceptibilities of the 1000°C RTP samples cooled at the standard rate of 4°C/sec were similar when the dwell time was varied from 1 seconds to 4 seconds, indicating that little further oxygenation occurs after the first second. The peak temperature of the RTP treatment seems to be important, since heating to 850°C reduced the 5K susceptibility.

It runs counter to intuition to suggest that 1-4 second dwells at peak temperature causes oxygenation, since the equilibrium oxygen content at 1000°C is known to be in the non-superconducting tetragonal range. A more likely explanation would seem to be that the material oxygenates during the rapid cool. To test this, a series was run with constant dwell time, but cooling rates either twice as fast (8°C/sec) or twice as slow (2°C/sec) than the standard rate. This would have a decisive affect if the reoxygenation occurred during the rapid cool. The data of Table I, however, show that the volume susceptibility is not affected by the cooling rate. Thus we reach the surprising conclusion that RTP increases the oxygen stoichiometry at 1000° to levels high enough to create orthorhombic 90K material. The mechanism for this is unclear.

Transmission electron microscopy of the $N_2$ sintered Y-123 before RTP shows that most of the grains are tetragonal. A few grains are partially converted to orthorhombic, often with twins growing inward from the grain boundaries. This is consistent with partial reoxygenation by $O^2$ impurities, and is the origin of the small diamagnetic signal at 5K. Figure 5 is a series of bright field images from ion-milled foils. Figure 5A shows one of the more partially orthorhombic grains in the as-sintered material. The twins are poorly developed and a large number of (as yet uncharacterized) lattice defects are visible. The twins boundaries are not crisply defined, an indication of oxygen depletion. The 1000°C-1 sec. RTP reduces the population of tetragonal grains and improves the quality of the orthorhombic grains. Figure 5B shows "cleaner" twin boundaries and fewer lattice defects. After the 1000°C-2 sec. RTP, most of the microstructure is similar to Figure 5C, with minimal defects and the sharp twin boundaries which are a sign of high oxygen content.

**Summary**

Rapid thermal processing, involving 2-4 sec. around 1000°C with a 3 min. cool down in oxygen, forms the dense sintered fibers of orthorhombic Y-123. Green fibers are rapidly densified, displaying microstructures characterized by large grains with distinctive blocky or elongated morphology. Presintered Y-123 fibers do not undergo drastic microstructural change after RTP, but are

Tc

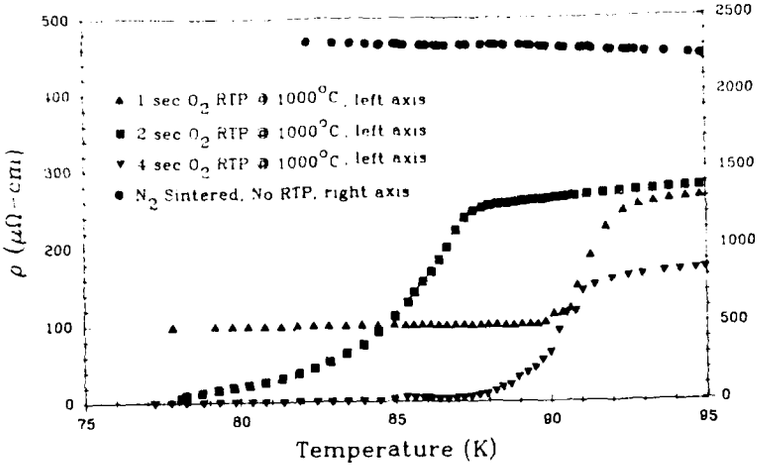


Figure 3 Resistivity vs. temperature for stoichiometric Y-123 fibers pre-sintered in nitrogen and RTP annealed in oxygen at 1000°C

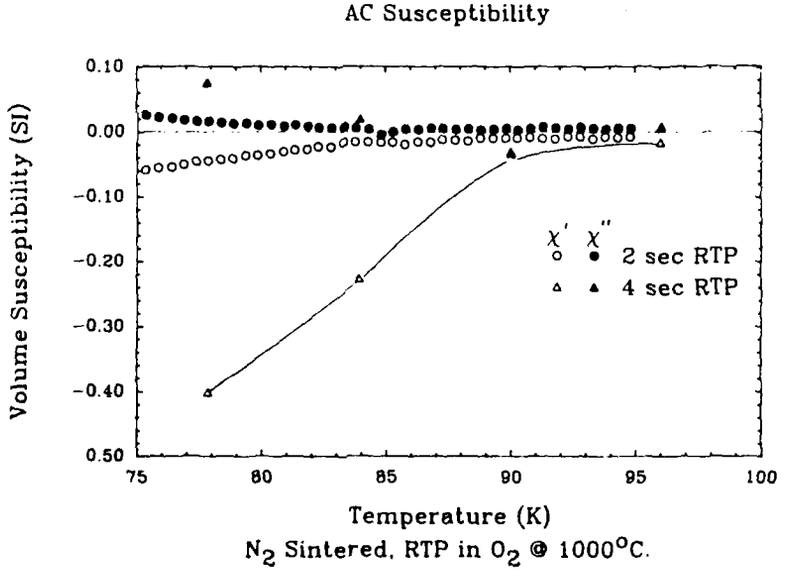


Figure 4 Real and imaginary AC susceptibility for stoichiometric Y-123 fibers pre-sintered in nitrogen and RTP annealed in oxygen at 1000°C

TABLE I

DIAMAGNETIC SHIELDING DATA AT 5K FOR NITROGEN-SINTERED Y-123

| RTP PROCESS CONDITIONS | VOLUME SUSCEPTIBILITY AT 100 Oe |
|---|---|
| AS- SINTERED, NO RTP | $-0.10/4\pi$ |
| 1000°C - 2 sec hold - 2°C/sec cool | $-0.21/4\pi$ |
| 1000°C - 2 sec hold - 4°C/sec cool | $-0.23/4\pi$ |
| 1000°C - 2 sec hold - 8°C/sec cool | $-0.24/4\pi$ |
| 1000°C - 1 sec hold - 4°C/sec cool | $-0.25/4\pi$ |
| 1000°C - 4 sec hold - 4°C/sec cool | $-0.26/4\pi$ |
| 850°C - 2 sec hold - 4°C/sec cool | $-0.15/4\pi$ |

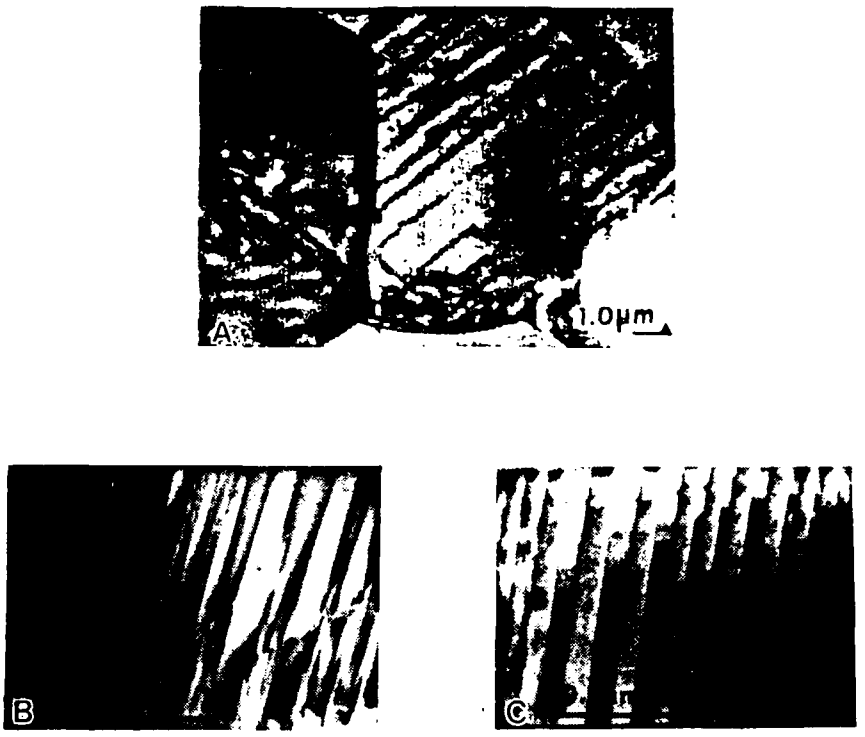


Figure 5 Bright field transmission electron micrographs of the nitrogen sintered series: A) as-sintered state, no RTP; (B) 1000°C/1 sec RTP; (C) 1000°C/2 sec RTP

rapidly oxygenated by the treatment. Presintered fibers, semiconducting and tetragonal before RTP, form twinned orthorhombic material after RTP with $T_c$ to 90K and magnetization indicative of substantially shielding.

Experiments with RTP of tetragonal Y-123 fibers made by pre-sintering in $N_2$ show that re-oxygenation by RTP in oxygen occurs during the 1-4 second isothermal hold at 1000°C, rather than during the 3-minute cooling ramp. Twinned orthorhombic Y-123 grows predominantly from grain boundaries, suggesting grain boundary diffusion of oxygen during the RTP anneal.

**Acknowledgements**

The work at CPS Superconductor was supported by DARPA contract N00014-88-C-0512 and NASA-Lewis contract NAS-3-25876. The Los Alamos work was supported by the High Temperature Superconductor Pilot Center Cooperative Agreement CRDA-89-03. The work at Sandia was supported, in part, by the DOE Office of Basic Energy Sciences under contract No.DE-AC04-76DP00789.

**References**

1. D.S. Ginley, E.L. Venturini, J.F. Kwak, M. Mitchell, R. J. Baughman, J.W. Halloran, and M.J. Neal, Physics Review Letters (in press 1990)

2. D.S. Ginley, E.L. Venturini, J.F. Kwak, R. J. Baughman, R.J. Bourcier, M.A. Mitchell, B. Morosin, J.W. Halloran, M.J. Neal, and D.W. Capone, in High Temperature Superconductors: Fundamentals, Properties, and Novel Processing, ed. J. Narayan et al. Materials Research Society, Symposia Proceedings Volume 196 , (in press 1990)

ATTACHMENT I

REPORT SUMMARY

# COMPOSITE CERAMIC SUPERCONDUCTING WIRES FOR ELECTRIC MOTOR APPLICATIONS

Second Annual Report on
Contract Number N00014-88-C-0512

July 30, 1990

John W. Halloran, Ceramics Process Systems Corporation,
Milford, MA 01757

This is a progress report for July 1989-June 1990, on a program to develop high temperature superconducting (HTSC) wire by cladding HTSC ceramic fibers with metal, and to build an high temperature superconducting motor.

We demonstrated our fiber process for wire by fabricating hundreds of meters of silver clad wire from both $YBa_2Cu_3O_{7-x}$ (Y-123) and $Bi_2Ca_2Sr_2Cu_3O_{10}$ (BiSCCO). The fiber spinning and green cladding operations produce kilometer-long continuous material. Much effort was devoted to scaling up the wire process to fabricate HTSC coils for a DC homopolar motor. The coils are not yet completed, but we have wound multiple turns of wire on the coil bobbins, and characterized the superconducting properties of the coiled wire. We have demonstrated multifilamentary conductors as cables and coils of sintered silver clad braided wire. The sintered polycrystalline wire has self-field critical current densities ($J_c$) as high as 2800 A/cm$^2$, but are weak-linked, so the $J_c$ falls rapidly with magnetic field.

To overcome the weak-link problem we "melt texture" the sintered wire by directional solidification. We have a continuous melt texturing process for Y-123 wires which, while slow, can produce textured wire up to 0.5 meters long. The melt textured wire has 77K transport $J_c$ above 11,770 A/cm$^2$ in self field and 2100 A/cm$^2$ at 1 telsa.

The Emerson Electric DC homopolar HTSC motor was designed to operate with low $J_c$ wire to be a test bed for wire. The machine has been fabricated and operated conventional copper coils. A novel class of superconducting motors have been designed at Emerson Electric subcontract, using trapped flux in melt textured Y-123 as "magnet replicas" in an new type of permanent magnet motor. These have the promise for very high output motors, and can be built in the very near term. The stator element and part of the rotor of the first prototype machine presently exist, and the HTSC magnet replica segments are now being fabricated.

ATTACHMENT II

ARPA ORDER NUMBER: 9525

PROGRAM CODE NUMBER: 7737

CONTRACTOR: Ceramics Process Systems Corporation
155 Fortune Boulevard
Milford, MA 01757

CONTRACT NUMBER: N00014-88-C-0512

CONTRACT EFFECTIVE DATE: 30 JUNE 1988

CONTRACT EXPIRATION DATE: 31 MARCH 1991

SHORT TITLE OF WORK: High Temperature Superconducting Wire and Motor

PRINCIPAL INVESTIGATOR: John W. Halloran
(508) 634-3422

Several types of HTSC wire have been produced and two types of HTSC motors are being built. Hundreds of meters of Ag- clad wire were fabricated from $YBa_2Cu_3O_{7-x}$ (Y-123) and $Bi_2Ca_2Sr_2Cu_3O_{10}$ (BiSCCO). The DC homopolar motor coils are not yet completed, but multiple turns of wire have been wound on the coil bobbins to characterize the superconducting properties of coiled wire. Multifilamentary conductors were fabricated as cables and coils. The sintered polycrystalline wire has self-field critical current densities ($J_c$) as high as 2800 A/cm$^2$, but the $J_c$ falls rapidly with magnetic field. To improve $J_c$, sintered YBCO wire is melt textured with a continuous process which has produced textured wire up to 0.5 meters long with 77K transport $J_c$ above 11,770 A/cm$^2$ in self field and 2100 A/cm$^2$ at 1 telsa.

The Emerson Electric DC homopolar HTSC motor has been fabricated and run with conventional copper coils. A novel class of potentially very powerful superconducting motors have been designed to use trapped flux in melt textured Y-123 as "magnet replicas" in an new type of permanent magnet motor. The stator element and part of the rotor of the first prototype machine exist, and the HTSC magnet replica segments are being fabricated.

ATTACHMENT III

ARPA ORDER NUMBER: 9525 PROGRAM CODE NUMBER: 7737

CONTRACTOR: Ceramic Process Systems Corporation
155 Fortune Boulevard
Milford, MA 01757

CONTRACT NUMBER: N00014-88-C-0512 CONTRACT AMOUNT: $ 5,509,387.00

EFFECTIVE DATE OF CONTRACT: 30 JUNE 1988

EXPIRATION DATE OF CONTRACT: 31 MARCH 1991

PRINCIPAL INVESTIGATOR: John W. Halloran

TELEPHONE NUMBER: (508) 634-3422

SHORT TITLE OF WORK: High Temperature Superconducting Wire and Motor

REPORTING PERIOD: 1 July 1989 through 30 June 1990

DESCRIPTION OF PROGRESS

This is a progress report for July 1989-June 1990, on a program to develop high temperature superconducting (HTSC) wire by cladding HTSC ceramic fibers with metal, and to build an high temperature superconducting motor.

We demonstrated our fiber process for wire by fabricating hundreds of meters of silver clad wire from both $YBa_2Cu_3O_{7-x}$ (Y-123) and $Bi_2Ca_2Sr_2Cu_3O_{10}$ (BiSCCO). The fiber spinning and green cladding operations produce kilometer-long continuous material. Much effort was devoted to scaling up the wire process to fabricate HTSC coils for a DC homopolar motor. The coils are not yet completed, but we have wound multiple turns of wire on the coil bobbins, and characterized the superconducting properties of the coiled wire. We have demonstrated multifilamentary conductors as cables and coils of sintered silver clad braided wire. The sintered polycrystalline wire has self-field critical current densities ($J_c$) as high as 2800 A/cm$^2$, but are weak-linked, so the $J_c$ falls rapidly with magnetic field.

To overcome the weak-link problem we "melt texture" the sintered wire by directional solidification. We have a continuous melt texturing process for Y-123 wires which, while slow, can produce textured wire up to 0.5 meters long. The melt textured wire has 77K transport $J_c$ above[1] 11,770 A/cm$^2$ in self field and 2100 A/cm$^2$ at 1 telsa.

The Emerson Electric DC homopolar HTSC motor was designed to operate with low $J_c$ wire to be a test bed for wire. The machine has been fabricated and

---

[1]. The apparent critical current was limited by Joule heating of the silver paint contacts, so the actual 77 K is higher by an unknown amount.

operated conventional copper coils. A novel class of superconducting motors have been designed at Emerson Electric subcontract, using trapped flux in melt textured Y-123 as "magnet replicas" in an new type of permanent magnet motor. These have the promise for very high output motors, and can be built in the very near term. The stator element and part of the rotor of the first prototype machine presently exist, and the HTSC magnet replica segments are now being fabricated.

SUMMARY OF SUBSTANTIVE INFORMATION DERIVED FROM SPECIAL EVENTS

Project members attended the several conferences on high temperature superconductivity to keep abreast of current developments.

CHANGE IN KEY PERSONNEL

No change

PROBLEMS ENCOUNTERED AND/OR ANTICIPATED

None

ACTION REQUIRED BY THE GOVERNMENT

None

FISCAL STATUS (June 30, 1990)

1) CUMULATIVE AMOUNT CURRENTLY RECEIVED ON CONTRACT . . . . . $ 3,637,963

2) CUMULATIVE EXPENDITURES AND COMMITTMENTS TO DATE..... $ 3,637,963

3) ADDITIONAL FUNDS REQUIRED TO COMPLETE WORK

THROUGH FY 1990..... $ 569,037